SELF DIFFUSION IN MgO UNDER THE INFLUENCE OF MODERATE ELECTRIC FIELDS IN THE TEMPERATURE RANGE OF 1100-1250K

by

Jose Roberto Martinelli

Dissertation

Sumitted to the Faculty of the
Graduate School of Vanderbilt University
In partial fulfillment of the requirements
for the degree of
DOCTOR OF PHILOSOPHY

in

Materials Science & Engineering

December, 1984

Nashville, Tennessee

SELF DIFFUSION IN MgO UNDER THE INFLUENCE OF MODERATE ELECTRIC FIELDS IN THE TEMPERATURE RANGE OF 1100-1250K

by

Jose Roberto Martinelli

Dissertation

Orientador
Robert A. Weeks

Submitted to the Faculty of the
Graduate School of Vanderbilt University
in partial fulfillment of the requirements
for the degree of
DOCTOR OF PHILOSOPHY

in

Materials Science & Engineering

December, 1984

Nashville, Tennessee

IPEN
LIVRO
Nº 17657
BIBLIOTECA

Approved:	Date:
Robert A. Weeks	30 Sept 1984
H. L. Lee	October 3, 1984
James J. Wert	Oct. 3, 1984
Edward Sonder	30 Sept 1984
Robert Benjamin	October 4, 1984
William F. Flanagan	4 Oct 84
Ernest A. Jones	10/4/84

INSTITUTO DE PESQUISAS ENERGÉTICAS E NUCLEARES
I. P. E. N.

MATERIALS SCIENCE
& ENGINEERING

SELF DIFFUSION IN MgO UNDER THE INFLUENCE OF MODERATE ELECTRIC FIELDS IN THE TEMPERATURE RANGE OF 1100-1250K

JOSE ROBERTO MARTINELLI

Dissertation under the direction of Professor Donald Leroy Kinser

Diffusion of oxygen and magnesium is studied in nominally pure MgO crystals for the temperature range of 1100-1250 K. A nuclear technique that uses the nuclear reaction $^{18}O(p,\alpha)^{15}N$ in the region of the resonant energy at 629 KeV, is used to measure ^{18}O concentration profiles. Oxygen diffusion coefficients are determined. In addition, magnesium drift is determined with an electric field applied to the samples. Activation energy and pre-exponential values are calculated for both oxygen and magnesium diffusion. Values are obtained for the Mg^{++} ionic transference number. These results are in good agreement with those expected by extrapolating higher temperature values.

The effect of time, temperature, and electric field strength on the cation drift are reported. Also, the effects on diffusion by doping MgO with 1500 μg/g chromium is determined; the results are consistent with the assumption that excess V_{Mg} are present due to trivalent impurities.

Rutherford backscattering in the random and channeling modes are used as a complementary technique to study surface modification in MgO due to electric field.

Approved_____ Date_____
Adviser

To my parents

for their love and guidance

and

to Elvira and Thiago

for their love and understanding

ACKNOWLEDGEMENTS

With deep pleasure I acknowledge the help and encouragement of Drs. Robert A. Weeks and Donald L. Kinser, Vanderbilt University, and Dr. Edward Sonder, Oak Ridge National Laboratory, under whose guidance and supervision this work was done. I wish to thank them for the stimulating scientific atmosphere provided during the execution of this work.

I express special thanks to Dr. Ray A. Zuhr who shared his knowledge of nuclear reaction techniques and accelerator physics with me.

I thank Dr. James M. Williams for the ion implantations, Dr. Robert J. Renka for discussions pertinent to the computer program elaboration, and Mr. Lee A. Zevenbergen for metal depositions.

Appreciation is also expressed to Dr. Frank A. Modine for supporting this work and Dr. Yok Chen for pertinent discussions concerning this study.

Mrs. Anne M. Keesee's assistance in typing both the draft and the final copy of the manuscript is greatly appreciated.

Sincere thanks are also extended to the staff of the Solid State Division of Oak Ridge National Laboratory for their interest and willingness to help, and for the friendly atmosphere which made my graduate life enjoyable.

The author came to this country under a scholarship provided by Comissão Nacional de Energia Nuclear (Brazil), and sponsored by Instituto

de Pesquisas Energeticas e Nucleares (Brazil), which are gratefully acknowledged.

This research is sponsored by the Division of Materials Sciences, U.S. Department of Energy under contract DE-AC05-84OR21400 with Martin Marietta Energy Systems, Inc.

TABLE OF CONTENTS

Page

LIST OF TABLES

LIST OF FIGURES

...ENERGÉTICAS E NUCLEARES
I. P. E. N.

INTRODUCTION

Diffusion processes are important in establishing the rate of solid state reactions, as well as chemical reactions between solids and liquids or gases. For example, oxidation of metals is controlled by the mobility of ions in the solid state. Noteworthy is the corrosion resistance of aluminum which is related to the formation of a protective film of Al_2O_3 on aluminum surfaces. This thin oxide layer is homogeneous and usually crack free. The extremely slow growth of this film at ambient temperatures is due to the slow rate of ionic diffusion through the oxide. In polycrystalline ceramics diffusion processing is used to densify the materials. Reduction of porosity occurs by the migration of atoms to pores. These processes in oxides have been studied extensively in order to provide a better understanding of defect structure as well as processes such as creep, sintering, grain growth, pore mobility, and electrical conduction. Measurements of self-diffusion coefficients as a function of temperature and oxygen partial pressure have been used to identify and characterize defect populations.

The transport properties of oxides are still not very well understood since there is only limited data and the results of the different investigators do not always agree. In contrast to alkali halides, the agreement with theory is comparatively poor. Therefore, it is useful to accumulate additional data on diffusion rates in high-purity oxide crystals, using techniques that allow direct determination of

diffusion coefficients when possible. A review of diffusion data for several oxides is given in references 1 and 2.

CHAPTER I

METHODS OF STUDYING DIFFUSION IN OXIDES

The most common methods of studying diffusion in oxides are those employing radioactive tracers and serial sectioning. The tracer concentration profile is obtained by measuring the activity of each removed layer, or the fractional activity remaining after material removal. However, for many elements there are no radioactive isotopes with half-lives long enough to provide accurate data. In those cases, methods employing stable isotopes as tracers may be chosen in connection with mass spectrometry analysis. The initial natural concentration of those isotopes inside the specimen to be analyzed has to be as low as possible in order to provide good resolution. A typical example is the case of oxygen self-diffusion in oxides; the use of oxygen radioisotopes as tracers is not feasible since there are none with a half-life longer than 2 minutes (e.g. ^{15}O). Thus, methods employing a stable isotope that differs from ^{16}O must be used in order to determine the concentration profile. A mass spectrometer is used to determine the ratio of $^{18}O/^{16}O$ in a gas phase previously enriched with ^{18}O and kept in equilibrium with the sample being investigated. Although this method is indirect and surface exchange may be a rate-limiting step, it is useful for the determination of relatively low diffusion rates (on the order of 1×10^{-16} $cm^2\ s^{-1}$). This method does not yield the distribution of the diffusing species (^{18}O) as a function of distance from the surface exposed

to the enriched gas, i.e. the concentration profile; only the time dependent variation of the ratio $^{18}O/^{16}O$ in the gas in equilibrium is measured. A profile can be determined by measuring the ratio $^{18}O/^{16}O$ by mass spectrometry as successive layers of the material are removed by mechanical grinding. Surface conditions have been reported to influence the self-diffusion coefficient [3].

When it is not possible to find suitable isotopes, a method employing electrical conductivity measurements can be used to study diffusion. The Nernst-Einstein equation is used to calculate the diffusion coefficient from the electrical conductivity data. This method is indirect and limited to those materials in which charge transport is exclusively ionic or in which the ionic transference number can be determined. One of its weaknesses is the difficulty in separating electronic and ionic transport without using other experimental techniques.

Ion beam mass spectrometry has also been used in diffusion studies. Material is removed from a surface through which tracer diffusion has occurred. This removal is done by bombarding the sample with a beam of ions, e.g., argon. The removed material is then analyzed by a mass spectrometer to determine the amount of the tracer isotope. Although this method has shown a high depth resolution, problems of ion identification and sputtering rates have been found [4]. By using the sputter profiling technique, the kinetic energy of the primary beam not only causes secondary ions to leave the surface, but also displaces ions in the surface layer laterally and into the bulk, which results in cascade mixing [5].

Nuclear reactions of various elements with energetic particles provide a practical alternative method of analysis and give a direct measurement of the profile of diffusing species. These techniques are widely used for oxygen diffusion because there are several reactions which can be induced, some of them showing useful characteristics for the determination of diffusion profiles.

Reactions most commonly used are:

i) $^{17}O(^{3}He,\alpha)^{16}O$ — uses rare stable isotope of oxygen.

ii) $^{18}O(p,n)^{18}F$ — ^{18}F emits a 0.6 MeV positron and has a half-life of 112 min. The proton beam energy has to be 2.7 MeV, and problems with activation of other elements are present. This reaction has been used to determine the oxygen diffusion coefficient by auto-radiograph exposure [6]. This technique is unique since it can show the existence of preferential diffusion paths such as grain boundaries, e.g., as in the case of undoped and Fe-doped MgO bicrystals [7].

iii) $^{18}O(p,\gamma)^{19}F$ — This reaction can be used close to the reaction resonance energy of 2.26 MeV, but has the same deficiencies as the $^{18}O(p,n)^{18}F$ reaction.

iv) $^{18}O(\alpha,n)^{21}Ne$ — ^{18}O profile can be determined by successive removal of surface layers, and by repeated bombardment.

v) $^{18}O(p,\alpha)^{15}N$ — This reaction has been used to study the oxygen diffusion in oxides, metals, as well as the oxidation of metallic alloys. The energy spectrum of α-particles provides information about the distribution of diffusing oxygen as a function of the distance from a surface through which diffusion has occurred. The stopping power for

protons and α-particles traveling through the sample must be known, as well as the differential cross section of this nuclear reaction.

There are at least three ways to use the nuclear reaction yield to determine the concentration profile of oxygen:

i) By inducing the nuclear reaction close to the resonance energies, which can be at 629 KeV or 1.765 MeV in the case of $^{18}O(p,\alpha)^{15}N$, and which can probe the isotopic oxygen ion concentration to depths up to 4 μm with a resolution of 0.1 μm [8].

ii) By analysis of the α-particle spectrum when the proton energy is greater than the resonance energy. This method is useful when a profile of small depth is to be determined [9].

iii) By removing successive layers of material mechanically, followed by proton activation analysis of each consecutive surface using the resonance technique at 629 KeV or 1.765 MeV.

The nuclear method is capable of sensitivities of the order of 10^{17} atm cm^{-3} [10], but for oxides, such as in the present work, the resolution is 10^{18} atm cm^{-3} due to 0.2% of ^{18}O naturally present in the oxide. The method is nondestructive if the resonance or the continuous spectrum methods are used. In practice only chlorine and boron may interfere with the analysis of ^{18}O, but ^{15}N and ^{19}F might have some influence in the production of α-particles [11]. The nuclear reaction $^{18}O(p,\alpha)^{15}N$ seems to be the most desirable for studying the oxygen diffusion in oxides, as well as the oxidation of metallic alloys. The maximum depth probed depends on the stopping power values for α-particles and protons. Backscattered protons are a problem since the α-particle detector may be jammed due to pileup [12]. These protons can be filtered with a mylar

film. The α-particles also lose energy in passing through the mylar foil and this loss limits the depth which can be probed. Much improvement is possible if protons can be prevented from reaching the detector without using a mylar foil. The separation of the backscattered protons from the α-particles also can be accomplished with a magnetic field. The resulting decrease in the width of the spreading function increases the depth to which an analysis can be achieved [9] to approximately 10 μm. However, for shallow profiles (< 1 μm) an absorber technique is preferred [12]. The concentration profile may be determined in the surface region (< 5 μm) with a resolution of the order of 0.1 μm. By improving the energy resolution of the detector, the resolution of this technique becomes < 100 Å near the surface [10].

There are a number of indirect procedures available to study diffusion, e.g., thermogravimetry, NMR measurements and optical absorption, all of which suffer from varying degrees of inaccuracy and difficulty of interpretation. These will not be discussed in the present work.

Electric field effects on diffusion

Effects of electric fields on diffusion of atomic species have become important with the widespread use of refractories as electrical insulators. The addition of an external electric field in diffusion experiments has also provided valuable information about the transport mechanisms of charged species, which could not be distinguished from neutral species by the traditional diffusion experiments. In this section we briefly review the work performed on alkali halides and oxides concerning the effects of electric field on diffusion.

INSTITUTO DE ENERGÉTICA NUCLEAR
I. E. N.

Effects on diffusion of an external electric field applied to a sample of NaCl have been reported [13]. In those experiments the electric field was applied to distinguish between the contribution of free sodium vacancies from those of vacancy pairs in the diffusion process.

It has been noted that electric fields produce a shift of the diffusion profile which can be correlated to the mobility of the diffusing species. Experimental data are in agreement with curves calculated from the solution of Fick's second law containing a drift term which includes the drift mobility and the electric field strength, in addition to the usual concentration gradient term [13].

The relative displacement of the diffusion profile was used to calculate directly the transport of sodium ions through a crystal in an electric field. Interdiffusion experiments in the KCl-KBr single-crystal system have shown clearly a shifting of the profile caused by an external dc electric field [14]. It was demonstrated that at high temperature some of the vacancies which take part in diffusion transfer of material, are electrically neutral.

There are a limited number of papers reporting on effects of electric field in transport properties of oxides. These are concentrated on solid state reactions in CaO-Al_2O_3 [15,16] and MgO-Al_2O_3 systems [17], and oxygen diffusion in UO_2 [18]. It has been shown, for example, that an electric field enhances diffusion of Ca into Al_2O_3 grains and changes the sintering rate of polycrystalline materials by assisting mass transfer across the contact zone between grains, and by a local electrical heating effect.

In the $MgO-Al_2O_3$ polycrystalline system, the Mg diffusion coefficient has been determined as a function of applied field by measuring the ratio [Mg]/[Al] using the Energy-Dispersive X-Ray (EDAX) probe in conjunction with a scanning electron microscope (SEM), and assuming the validity of the solution of Fick's second law for the appropriate boundary conditions [17]. It has been noted that the diffusion coefficient of Mg into Al_2O_3 is markedly increased in the presence of an electric field when the alumina side of the couple is polarized negatively. On the other hand, when the alumina side is polarized positively a very small increase in the diffusion coefficient over the one in the absence of field is observed.

Dornelas et al. [18] observed that polycrystalline UO_2 subjected to electric fields at 1000°C, decomposes in the cathodic region. Metallic phases involving uranium and platinum (the electrode material) have been observed on the cathode. Consequently the released oxygen diffused to the anode creating an oxygen excess oxide UO_{2+x}, x varying from 0 (cathode region) up to 0.25 (anode interface).

It has been shown by Gonzalez et al. [19] that protons and deuterons can be swept out of MgO single crystals when subjected to a moderate electric field (2000 V/cm) at 1300 K. The drifted ions are moved to the cathode in agreement with the expectation that protons are swept toward the negative pole.

In addition, material degradation has been reported [20] to occur in undoped MgO single crystals subjected to electric fields of the order of 10^3 V/cm at T > 1000°C. An increase in electrical conductivity leads to a subsequent breakdown. Dark streaks develop. In the streaks the

presence of relatively high concentration of dislocation loops, voids, and precipitates have been observed [20]. Although two models have been proposed to explain the origin of this dielectric breakdown, there is still a lack of experimental evidence to substantiate them. Sonder et al. [21] suggested that the degradation of the material leading to breakdown is due to a resistivity decrease along dislocations and small-angle grain boundaries, and only the final sudden breakdown is due to thermal runaway [22]. A double injection model has been proposed by Tsang et al. [23] in which electrons are injected by the cathode and holes by the anode. In this model, accumulation of negatively charged ionic species is proposed in the region adjacent to the anode in order to explain the increase of hole injection.

Research Objective

In the present work, a technique is developed to investigate ionic drift in solids caused by an external electric field. The measurement of the oxygen isotope, ^{18}O, concentration profile is used to determine the oxygen diffusion coefficient as well as the mobility of ionic species drifted by the electric field. Consequently, both oxygen and cationic diffusivity can be obtained. Moreover, the cationic transference number can be determined.

This technique is used to investigate the movement of magnesium ions to the surface region of MgO single crystals subjected to electric fields ranging from 0 to 3×10^3 V cm^{-1} in the temperature range of 800-1000°C.

The choice of MgO was based upon its relatively simple structure (face centered cubic), the availability of high-quality crystals, and its relatively high ionic transference numbers. These characteristics make it an excellent subject for a fundamental investigation of mass transport.

Experimental Technique for Measurements

In the present work the nuclear resonance reaction $^{18}O(p,\alpha)^{15}N$ is used to measure the ^{18}O concentration profile. Alpha particles are detected as a function of incident proton energy. The integrated α-particle count is plotted against the proton energy resulting in the so-called excitation curve.

Charged particles moving through a solid lose energy at a rate determined by the type of particles, their energy, and the stopping power of the material. The mean particle energy, E_m, decreases after penetrating to a given depth in a solid [24]. When the initial energy E_i is equal to 629 KeV, the resonance reaction occurs for ^{18}O just at the surface of the sample, but not for ^{18}O within the sample. For E_i slightly greater than 629 KeV, the nuclear reaction will be induced at a depth at which the energy has dropped to 629 KeV, as shown by the diagram in Fig. 1. This depth can be calculated by using published data for the stopping power of each element [25] and applying Bragg's rule for a compound [26].

Method of analysis

The experimental data as obtained may be analyzed by either convolution or deconvolution as described by Rawal et al. [27].

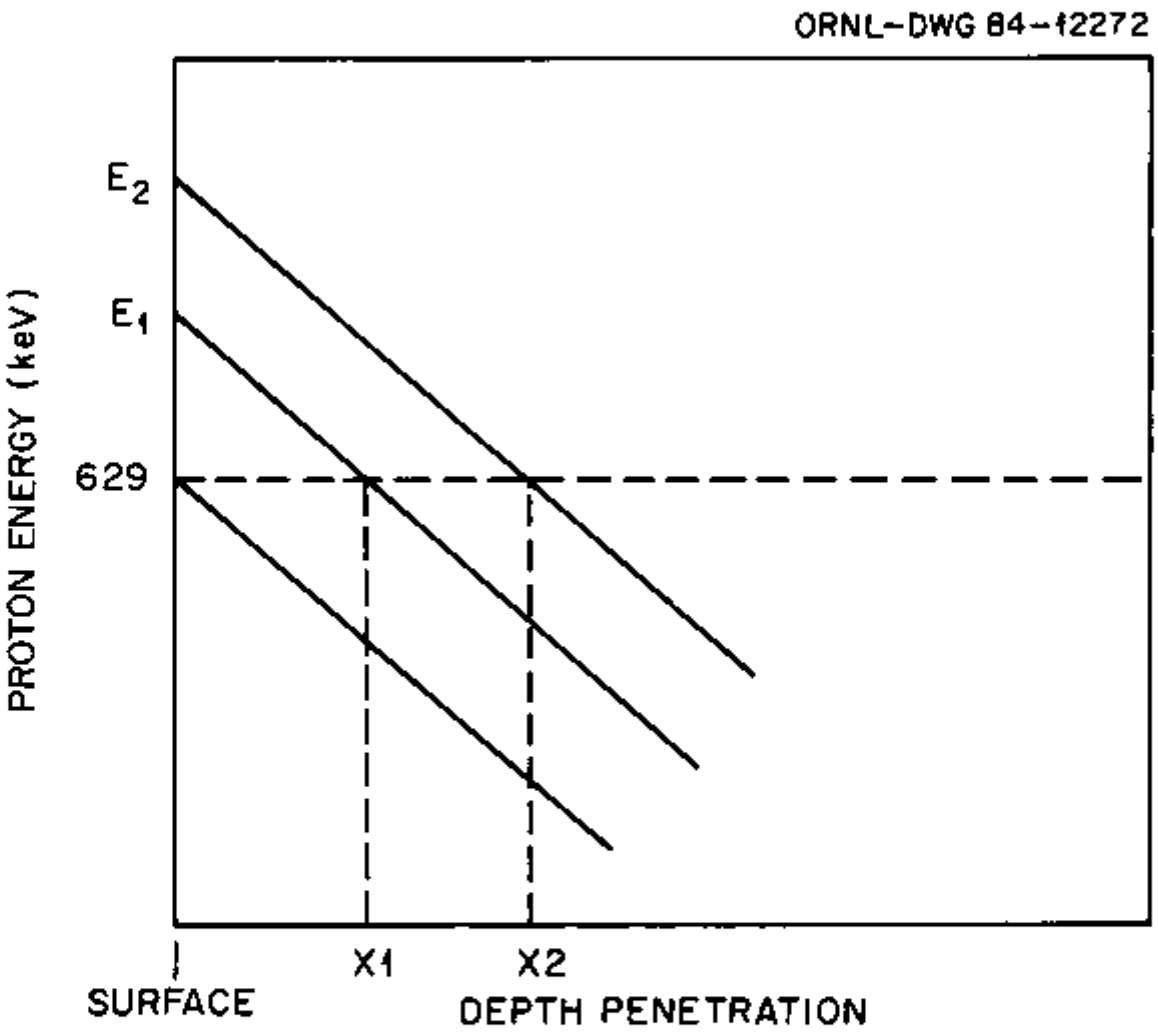

Fig. 1. Proton energy vs depth penetration. The horizontal dashed line at 629 KeV shows the depth at which the proton energy is 629 KeV. That is the depth at which the resonance reaction occurs.

There are three basic factors contributing to the observed rounding and spreading of the integrated α-particles count and the depth profile [28]:

i) Initial proton beam energy spread, ΔE. The proton beam produced by the Van der Graaff accelerator has an energy distribution approximated by a gaussian distribution.

ii) Proton straggling. Both energy and energy distribution of the protons are a function of the material and the distance x through which they have traveled in the target. The standard deviation is given by Bragg's scattering formula:

$$\phi = \phi_0 + KX^{1/2} \tag{1}$$

where ϕ_0 is the initial standard deviation and $K = 8.54 \times 10^{-7}$ $esu^2/cm^{3/2}$ for MgO. For $E_p > E_r$, the resonance energy,

$$\phi = \phi_0 + K'(E_p - E_r)^{1/2} \tag{2}$$

where $K' = K(S_p)^{-1/2}$ and S_p is the stopping power for protons travelling through MgO.

iii) Resonance width. The natural width of the resonant peak at 629 KeV is 2.1 KeV as shown by Fig. 2. Hence, a resonance reaction does not occur at a unique energy and this distribution must be included. Another factor that can be seen from Fig. 2 is the nonzero cross section for proton energies differing from the resonance energy. The reaction of ^{18}O with protons whose energies are greater than the resonance energy, contributes to the α-particle yield and therefore must also be included.

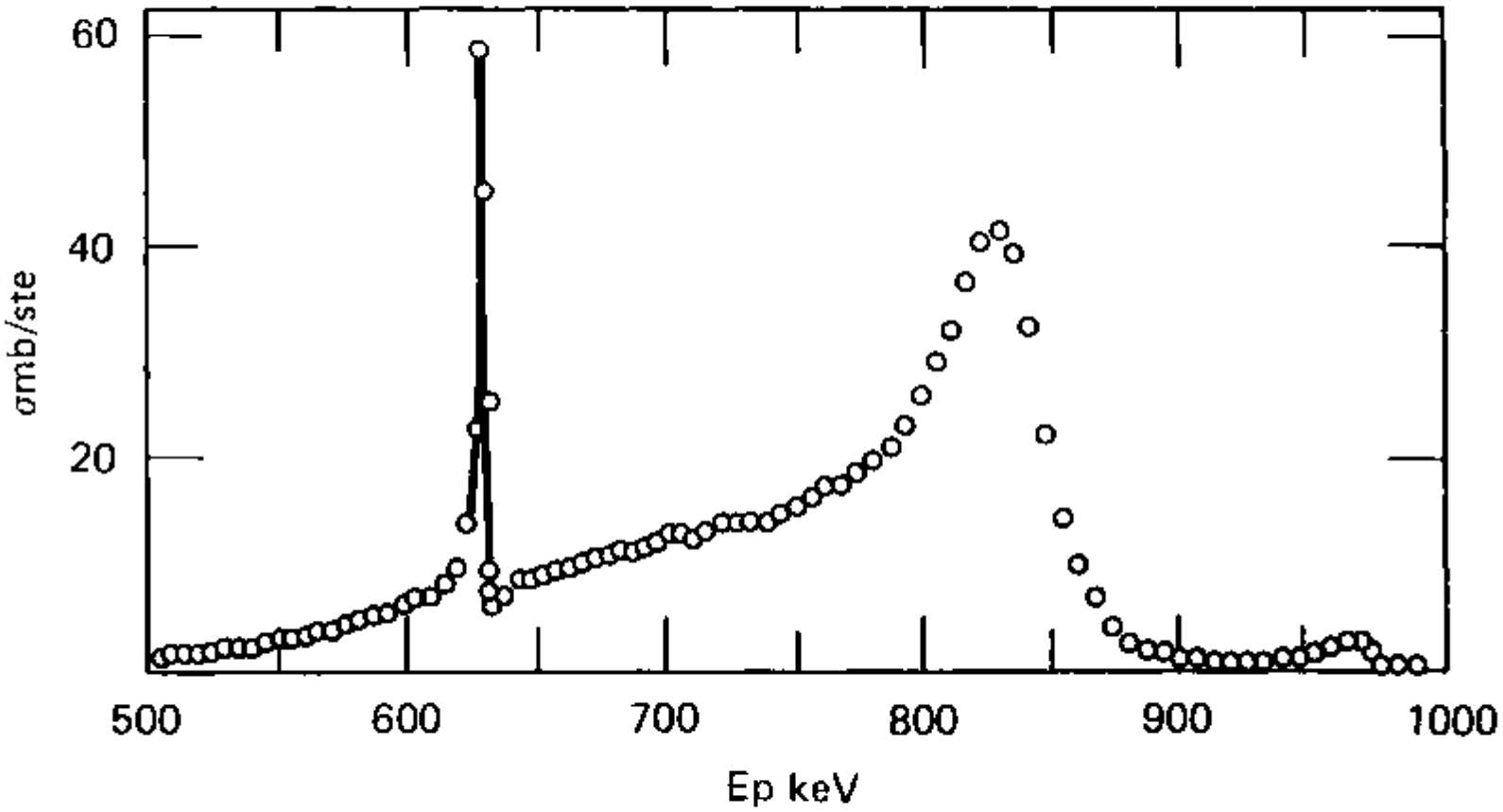

Fig. 2. Differential cross section vs incident proton energy at θ_{lab} = 165° for $^{18}O(p,\alpha)^{15}N$ reaction. From Fig. 2b of G. Amsel and D. Samuel, Anal. Chem. 39, 1689 (1967).

The parameters involved in the diffusion model are inferred either by fitting the deconvoluted spectra with undistorted profiles or by fitting the recorded spectra with the convoluted profiles. We have selected the latter method.

The nuclear reaction yield can be calculated for each incident proton energy from the following equation:

$$Y = i\varepsilon\Omega \int_0^x C(x') \int_{E'-6\phi}^{E'+6\phi} \frac{\xi(E',\theta)}{\sqrt{2\pi}\phi} \exp\left[-\frac{1}{2}\left(\frac{E-E'}{\phi}\right)^2\right] dE'dx' \qquad (3)$$

where i is the integrated current, ε the detector efficiency, Ω the solid angle subtended by the detector, $C(x')$ the assumed concentration profile, and $\xi(E',\theta)$ the differential cross section.

Literature Survey on Oxygen Diffusion in MgO

Oxygen diffusion in MgO has been determined by the gas-solid isotope exchange [29], by the autoradiographic technique inducing the nuclear reaction $^{18}O(p,n)^{18}F$ [6], and by the yield of the nuclear reaction $^{18}O(p,\alpha)^{15}N$ [30]. The results obtained for the diffusion coefficient are summarized in Table 1. It can be noted from this table that the pre-exponential term D_0 from the Arrhenius equation (Eq. 11) has a wide range of values (differing by 10 orders of magnitude). In addition, the activation energy Q from the same equation ranges over about a factor of four. In view of the wide range of D_0 and Q, a redetermination of these values is useful, particularly at low temperature, < 1400 K.

TABLE 1

OXYGEN DIFFUSION DATA IN MgO

Samples	Temperature Range (°C)	D_o x 10^{10} (m^2/sec)	Q (KJ/mole)*	Nature of Diffusion	Ref.
(i) Single crystals					
Low purity	1300-1750	2.5	261	Extrinsic	29
High purity	975-1150	43	343	Intrinsic	31
High purity	750-975	4.8×10^{-8}	125	Extrinsic	31
Cr-doped (300 ppm)	1000-1150	4.8×10^{-6}	142	Extrinsic	31
Cr-doped (300 ppm)	835-1000	1.5×10^{-2}	228	Below inverted knee	31
Li-doped (380 ppm)	1040-1150	1.4×10^{-5}	178	Extrinsic	31
High purity-ORNL	1350-1550	2.0×10^{2}	370		30
(ii) Polycrystals					
Undoped	1050-1490	0.45	252	Extrinsic	32
Li-doped (3-5 at.%)	1090-1420	0.52	186	Extrinsic	33
Undoped (loosely sintered)	1020-1260	1.6×10^{-2}	186	Extrinsic	34
Undoped (loosely sintered)	1260-1450	9.9×10^{3}	430	Intrinsic	34
Undoped (large grain)	1100-1427	1.36×10^{4}	460	Intrinsic	35

*1 kJ/mole = 1.037×10^{-2} eV/atm

It has been suggested [29] that oxygen diffusion in MgO is an impurity-controlled and/or structure-sensitive process (e.g., affected by subgrain boundaries and dislocations), and that the activation energy corresponds to that for ion mobility. However, the activation energy has a meaning only when the transport mechanism is determined. Also, it is suggested [31] that at low temperature the transport of oxygen is by both interstitial and vacancy mechanisms. The vacancy concentration is

interstitial and vacancy mechanisms. The vacancy concentration is dependent upon the crystal purity, oxygen partial pressure, and temperature. On the other hand, there are reports [5,36] on oxygen diffusion in iron-doped MgO and scandium-doped MgO which claim that oxygen diffusion is insensitive to the presence of aliovalent cations of higher valence than magnesium. In solid solution these cations are known to enhance the concentration of magnesium ion vacancies and decrease the oxygen vacancy concentration.

Literature Survey on Magnesium Diffusion in MgO

Self-diffusion of magnesium in MgO has been determined by several experiments in the range of temperatures 1000–2400°C. Table 2 summarizes the available data. Although there are reports claiming the observation of Mg diffusion through intrinsic vacancies [37], the relatively high Schottky formation energy would preclude such observation at temperatures below the melting point, even in the purest samples [38]. The values of D_0 and activation energy are of magnitudes comparable to those observed in measurements of impurity cation diffusion, and are therefore attributed to extrinsic impurity-controlled diffusion [39].

There is fair agreement that Schottky defects are predominant in MgO with formation enthalpy varying from 390 kJ/mol to 800 kJ/mol, according to theoretical calculations [30]. Experimental activation enthalpies are consistent with formation enthalpy, ΔH_f = 370 kJ/mol and migration enthalpy, ΔH_m = 145 kJ or with ΔH_f > 870 kJ/mol and ΔH_m = 270 kJ [42].

... NUCLEARES
... E. N.

TABLE 2

MAGNESIUM SELF-DIFFUSION COEFFICIENT IN MgO

Temperature Range °C	D_o cm^2/sec	Q kJ/mol*	Remarks	Reference
1400—1600	0.249	331	Tracer value sectioning technique	37
1200—1600	0.38	220	From mobility determination by e.m.f.	38
1000—2400	4.19×10^{-4}	266	Mass spectrometry of stable isotope ^{26}Mg as tracer	39
1265—2350	7.48×10^{-6}	151	Tracer value sectioning method using ^{28}Mg radioactive tracer	40
1100—1400 1400—1750	0.54 1.6×10^{-5}	308 164	Tracer value sectioning method	41

*1 kJ/mole = 1.037×10^{-2} eV/atm

The ionic conductivity and transference number have been measured in MgO single crystals for temperatures ranging from 1100°C to 1600°C. The ionic transference number was determined by the emf method [38], and dilatocoulometric method [43] as a function of oxygen partial pressure. The values reported for 1 atm of oxygen are 0.44 at 1155°C and 0.31 at 1234°C [43].

The ionic conductivity has been determined to be directly proportional to the concentration of the trivalent solutes [38]. The controlling charge-balance equation appears to be

$$2[V''_{Mg}] = [I^{\bullet}_{Mg}] + [Fe^{\bullet}_{Mg}] \quad , \tag{4}$$

where $[V''_{Mg}]$ is the concentration of double ionized magnesium vacancies, $[I^{\bullet}_{Mg}]$ is the concentration of trivalent solutes excluding iron and $[Fe^{\bullet}_{Mg}]$ is the Fe^{3+} concentration.

CHAPTER II

BASIC THEORY OF DIFFUSION

Fick's Laws

An ideal crystal is composed of atoms distributed in a regular periodic arrangement of points in a space defined lattice [44]. A lattice is a mathematical abstraction useful in understanding a crystalline structure. However, in practice, such a perfect crystalline system does not exist because of the existence of thermally created intrinsic defects, e.g., Schottky and/or Frenkel pairs, or defects created by impurities. The presence of aliovalent impurities causes an electrical charge unbalance which is compensated by defects such as vacancies and/or interstitials.

Structural imperfections or defects are a primary avenue for atom migration in solids. Volume or bulk diffusion is the atomic migration of ions caused by motion of the lattice defects, e.g., vacancies and interstitial atoms. Planar and linear defects, e.g., grain boundaries and dislocations, may be avenues for enhanced atom migration.

Analogous to the problem of heat conduction, a mathematical theory of diffusion in an isotropic medium has been developed [45]. Fick's first law in one dimension states that the rate of transfer, J, of diffusing species is directly proportional to the concentration gradient $\partial C(x,t)/\partial x$:

$$j = -D \frac{\partial C(x,t)}{\partial x} \quad . \tag{5}$$

The proportional constant D is called the diffusion coefficient. Fick's second law is derived from the above and the continuity equation; and for the particular case of the diffusion coefficient being independent of the concentration, Fick's second law takes the simple form

$$\frac{\partial C}{\partial t}(x,t) = D \frac{\partial^2 C(x,t)}{\partial x^2} \quad . \tag{6}$$

This equation may be solved explicitly for certain boundary conditions which can be experimentally defined. For instance, in a semi-infinite solid with an initial constant tracer concentration, C_o, uniformly distributed throughout, and with surface maintained in equilibrium with a gas phase, the boundary condition is

$$C(o,t) = C_g \qquad \text{for } t > 0 \tag{7}$$

C_g is the fractional concentration of tracer in the gas phase, and C(o,t) is the fractional concentration of tracer at the surface of the solid. The solution of Eq. (6) satisfying the above condition is [45]

$$C(x,t) - C_o = (C_g - C_o)\ \mathrm{erfc}\left(\frac{x}{2\sqrt{Dt}}\right) \quad . \tag{9}$$

If the surface does not instantaneously equilibrate with the concentration of the tracer in the gas, the boundary condition at x=o for t>o is

$$-D\left(\frac{\partial C}{\partial x}\right)_t = V\,[C_g - C(o,t)] \tag{6}$$

with $$C(x,t) \to C_o \text{ as } x \to \infty \quad .$$

V is the first-order surface exchange coefficient. The solution of Eq. (6) satisfying that condition is now [30]

$$\frac{C(x,t)-C_o}{C_g - C_o} = \text{erf}\left(\frac{x}{2\sqrt{Dt}}\right) - \exp\left(\frac{V^2t+Vx}{D}\right) \text{erfc}\left(\frac{2Vt+x}{2\sqrt{Dt}}\right) \quad . \qquad (10)$$

By establishing a temperature dependence of the diffusion coefficient, the activation energy and, therefore, the sum of the enthalpies of defect formation and motion can be determined, leading to an atomistic interpretation of the mechanism of diffusion.

Experimentally determined diffusion coefficients are usually expressed by an Arrhenius-type equation

$$D = D_o \exp\left(-\frac{Q}{RT}\right) \quad , \qquad (11)$$

where D_o is the pre-exponential factor, Q the activation energy, R the gas constant, and T the absolute temperature.

In the particular case of diffusion taking place by the vacancy mechanism, the activation energy Q is the sum of both the enthalpy of vacancy formation, ΔH_f, and the enthalpy of ionic motion, ΔH_m, if the intrinsic vacancies are predominant [46]

$$Q = \Delta H_f + \Delta H_m \quad . \qquad (12)$$

However, if extrinsic vacancies are predominant, the activation energy for diffusion is

$$Q = \Delta H_m \quad . \qquad (13)$$

In any case, the mechanism is the same. An atom in a lattice site jumps to a nearest vacancy. The net effect is atoms migrating in one direction and vacancies in the opposite direction.

Although the vacancy mechanism was chosen as an example, there are other possible mechanisms such as interstitial, interstialcy, and ring mechanisms which are discussed in detail in reference 46.

Drift Caused by an Electric Field

In the case of electric-field forced diffusion, Fick's second law contains a driving force term in addition to the concentration gradient:

$$\frac{\partial C(x,t)}{dt} = D\,\frac{\partial^2 C(x,t)}{\partial x^2} - \mu E\,\frac{\partial C(x,t)}{\partial x} \quad , \tag{14}$$

where μ is the mobility of the diffusing species and E is the electric field strength.

For a semi-infinite specimen with initial and boundary conditions $C(x,o) = C_o$, $C(o,t) = C_g$, respectively, the solution of Eq. (14) when both electric field and diffusion are in the same direction is [47]:

$$C+(x,t) = C_o + \frac{C_g - C_o}{2}\left[\left\{1-\mathrm{erf}\left(\frac{x-\mu Et}{2\sqrt{Dt}}\right)\right\} + e^{\frac{\mu Ex}{D}}\left\{1-\mathrm{erf}\left(\frac{x+\mu Et}{2\sqrt{Dt}}\right)\right\}\right] \tag{15}$$

Upon reversing the direction of the applied field but keeping the same field strength, the solution to Eq. (14) is given by [47]

$$C-(x,t) = C_o + \frac{C_g - C_o}{2}\left[\left\{1-\mathrm{erf}\left(\frac{x+\mu Et}{2\sqrt{Dt}}\right)\right\} + e^{-\frac{\mu Ex}{D}}\left\{1-\mathrm{erf}\left(\frac{x-\mu Et}{2\sqrt{Dt}}\right)\right\}\right] \quad . \tag{16}$$

Effects of an electric field on the migration of charge species in a homogeneous crystal involves a decrease of the activation energy for migration by a factor of $\frac{ZesE}{2}$ in one direction, and an increase by the same factor in the reverse direction. Figure 3 illustrates this concept where s is the interplanar crystalline distance, e the electron charge, and Z the charge state. The resulting current density J_i caused by the directional charge transport is given by

$$J_i = \sigma_i E \quad , \tag{17}$$

where the subscript i designates a particular specie (ionic or electronic), and σ_i is the conductivity of that specie. The conductivity of particles of type i is

$$\sigma_i = t_i \sigma \quad , \tag{18}$$

where t_i is the transport (or transference) number of specie i.

The total electrical conductivity σ is given by the sum of the electronic and ionic conductivities. If only one ionic specie and one electronic specie are contributing to the conductivity, then

$$\sigma = \sigma_{ion} + \sigma_{el} \quad . \tag{19}$$

In this case the ionic transport number, t_{ion}, is defined as the ratio between the ionic conductivity and the total conductivity:

$$t_{ion} = \frac{\sigma_{ion}}{\sigma} \quad . \tag{20}$$

The conductivity is related to the charge carrier mobility μ by the following equation:

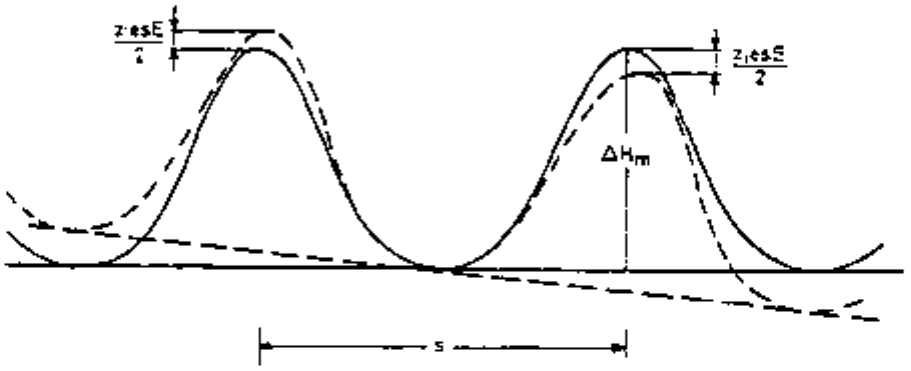

Fig. 3. Schematic illustration of the electric field effect on the crystal potential: solid line indicates potential without perturbation, dashed line is potential with field perturbation.

$$\sigma = Z e c \mu \quad , \tag{21}$$

where c is the concentration of mobile species.

The Nernst-Einstein relation establishes a relation between mobility and diffusion coefficient of any species, and it is derived from the calculation of the net flow of particles in the presence of an electric field, assuming random diffusion in a homogeneous system [46]:

$$\mu = \frac{Ze}{KT} D \quad , \tag{22}$$

where K is the Boltzmann constant and T the absolute temperature.

In a solid electrolyte subjected to an electric field applied through oxygen reversible electrodes, a relative displacement of the electrolyte-electrode interface is observed [43]. This displacement has been attributed to the accumulation of ionic species in the electrolyte-electrode interface [43]. It has been reported [43] that an accumulation of 0.1 Coul is enough to cause a displacement of approximately 3 μm at 1160°C.

Taking the particular case of cationic migration, the cationic transference number can be calculated by a simple charge-mass balance. The cationic transference number will be the ratio of the equivalent charge due to the cationic motion and the total charge transported through the material:

$$t_{cat} = \frac{nZF}{I\Delta t} \quad , \tag{23}$$

where n is the number of moles of cationic species, I the dc current, Δt the time interval, and F Faraday's constant.

It is clear that

$$n = \frac{a\ S\ \Delta x}{M} \quad , \tag{24}$$

where S Δx is the volume of the displaced region, a the material density, and M the molecular weight.

Hence

$$t_{cat} = \frac{a\ S\ Z\ F\ \Delta x}{M\ I\ \Delta t} \quad . \tag{25}$$

In the present work it is assumed that the surface area of the interface electrolyte-electrode is kept constant, and the electrolyte-electrode interface is displaced by Δx normal to the electrode plane. Therefore, the factor S/I can be easily replaced by 1/J leading to Eq. (26):

$$t_{cat} = \frac{a\ Z\ F\ \Delta x}{M.J.\Delta t} \quad . \tag{26}$$

Assuming pure cationic motion, t_{cat}=1, Eq. (26) is rearranged as

$$MJ\Delta t = a\ Z\ F\ \Delta x \quad . \tag{27}$$

Therefore the mobility is

$$\mu = \frac{a\ F\ \Delta x}{MecE\ \Delta t} \quad , \tag{28}$$

where c is the cation vacancy concentration.

The cation vacancy diffusion coefficient, D_v, is determined by Eq. (29) when one combines Eqs. (22) and (28):

I. P. E. N.

$$D_v = \frac{K\ T\ a\ F\ \Delta x}{Z\ e^2\ M\ c\ E\ \Delta t} \quad . \qquad (29)$$

CHAPTER III

EXPERIMENTAL PROCEDURE

Sample Preparation

Samples of MgO nominally pure* single crystals were cut with a diamond edge saw in slabs (1x1x0.1 cm) and (1x0.6x0.1 cm) from a boule with faces on the crystallographic planes {100}. The original boule was in the form of a rectangular parallelipiped 1x1.5x1.5 cm. After grinding with a series of successively finer abrasives, such as 240, 320, 400, and 600 grit SiC impregnated paper, as well as 3/0 carborundum impregnated paper, each sample was mechanically polished with alumina slurries, 0.3 μm in particle size. Water was used during the grinding. After polishing, samples were chemically polished with a solution of 85% HPO_3 at 150°C for 30 seconds in order to remove the surface layer left from the mechanical polishing procedure [48]. Chemical polishing is also necessary since the nuclear technique has shown that mechanical polishing, even using fine alumina, produces a contaminated surface [49]. After polishing, the samples were washed in water, in acetone, and then dried in air at room temperature.

It has been demonstrated by Spadaro [50] that annealing at 1400°C reduces the dislocation density in MgO single crystals by at least an

*Crystals grown by Tateho Chemical Industries Co., Ltd, Hyogo-ken, Japan. Neutron activation analysis performed by ORNL indicates the following principal impurities in μg/g: Al, 44; V, 20; Cr, 8; Mn, 2; Fe, 71; and Na, 130.

order of magnitude and produces a realignment of dislocations in polygonized arrays. However, the penetration depth of dislocations show little or no change. Because of these effects it was decided to anneal the samples at 1400°C for 4 h in air prior to the introduction of the isotopic tracer.

After the tracer introduction and the diffusion annealing, the surfaces of the samples were covered with a layer of aluminum 200 A thick by sputtering an aluminum target with argon. The aluminum layer provides an electrical contact between the sample and the sample holder during the nuclear analysis and thereby reduces the accumulation of charges generated by the proton bombardment. Charge accumulation adversely affects the measurement of the emitted α-particles because of the energy reduction of protons due to coulombic interaction, thus giving an erroneous indication of depth of the $^{18}O(p,\alpha)^{15}N$ reaction. In addition, electrical breakdown on the surface might introduce electronic noise in the detector.

Analytical Procedure

The oxygen diffusion coefficient is generally obtained from fitting the mathematical solution of the differential diffusion equation to the experimental concentration profile of the tracer. Depending on the boundary conditions, several analytical solutions are possible. The boundary conditions are determined experimentally, by the method of tracer introduction.

Three different methods (and therefore three different boundary conditions) have been used in these experiments to introduce tracers

into the sample. They are: i) implantation, ii) gas/solid isotopic exchange, and iii) gas/solid isotopic exchange with electric field externally applied.

Implantation

The {100} face on MgO single crystals was implanted with $^{18}O^{+}$ ions with energy of 110 KeV and an integrated flux of 10^{17} ions cm^{-2}. For this energy the gaussian distribution of the implanted ions had a maximum at 1412 A and a standard deviation of 722 A about this depth. Diffusion anneals were made at temperatures in the range of 200-1600°C in air. For temperatures greater than 800°C, samples were placed in a magnesia boat and for temperatures lower than 800°C, in a quartz boat, and inserted in an electric furnace with a quartz muffle tube. Annealing times ranged from 1 to 75 hours. At the end of each anneal, samples were quenched in air to room temperature by withdrawing the boat from the furnace.

Gas/solid isotopic exchange

Diffusion anneals were performed on MgO samples in equilibrium with one atm of 95% $^{18}O_2$ gas* in the range of temperatures 800-1000°C, during time intervals ranging from 24 to 400 hours. A quartz tube inserted in an electric furnace contained the samples.

Gas/solid isotopic exchange with electric field externally applied

MgO samples were equilibrated with one atm of 95% $^{18}O_2$ gas in the range of temperatures 800-1000°C. An electric field with strengths ranging

*$^{18}O_2$ gas was purchased from Monsanto Research Corporation.

from zero to 3000 V/cm was applied between the {100} surfaces of the samples during the diffusion annealing. Figure 4 shows the experimental apparatus consisting of a temperature and pressure-controlled system. Electrodes were platinum gauze (45 and 100 mesh). Samples were inserted in a quartz tube and compressed between two electrodes by means of a spring system. To keep the pressure uniformly distributed on the surface of the sample, two perforated discs, initially made of machinable glass ceramic (MACOR)*, were used in contact with the electrodes. However, an abnormally high background was detected during the nuclear analysis. The origin of this background was found to be the product of a nuclear reaction involving boron ($^{11}B(p,\alpha)^{8}Be$ with Q = 5.65 MeV) producing α particles with energy 3.70 MeV when the incident proton energy was 0.65 MeV [51]. This assumption was checked by promoting the same nuclear reaction with samples containing boron, such as BN and Ni_3B. It was concluded that the source of boron contamination on the MgO was the MACOR discs, since this material contains 7% B_2O_3. Therefore, parts made of MACOR were replaced by pure alumina.

The samples were inserted in the furnace after it reached a stable temperature. The system was then evacuated to 10^{-5} mm Hg and filled with 1 atm of 95% $^{18}O_2$ enriched oxygen. During the process of filling, the gas passed through a cold trap in order to remove any residual water. Samples of the $^{18}O_2$ gas were collected before and after the diffusion annealing and analyzed by mass spectrometry in order to monitor

*MACOR machinable glass ceramic chemical composition provided by Duramic Products, Inc., New Jersey: 46% SiO_2, 16% Al_2O_3, 17% MgO, 10% K_2O, 4% F, 7% B_2O_3.

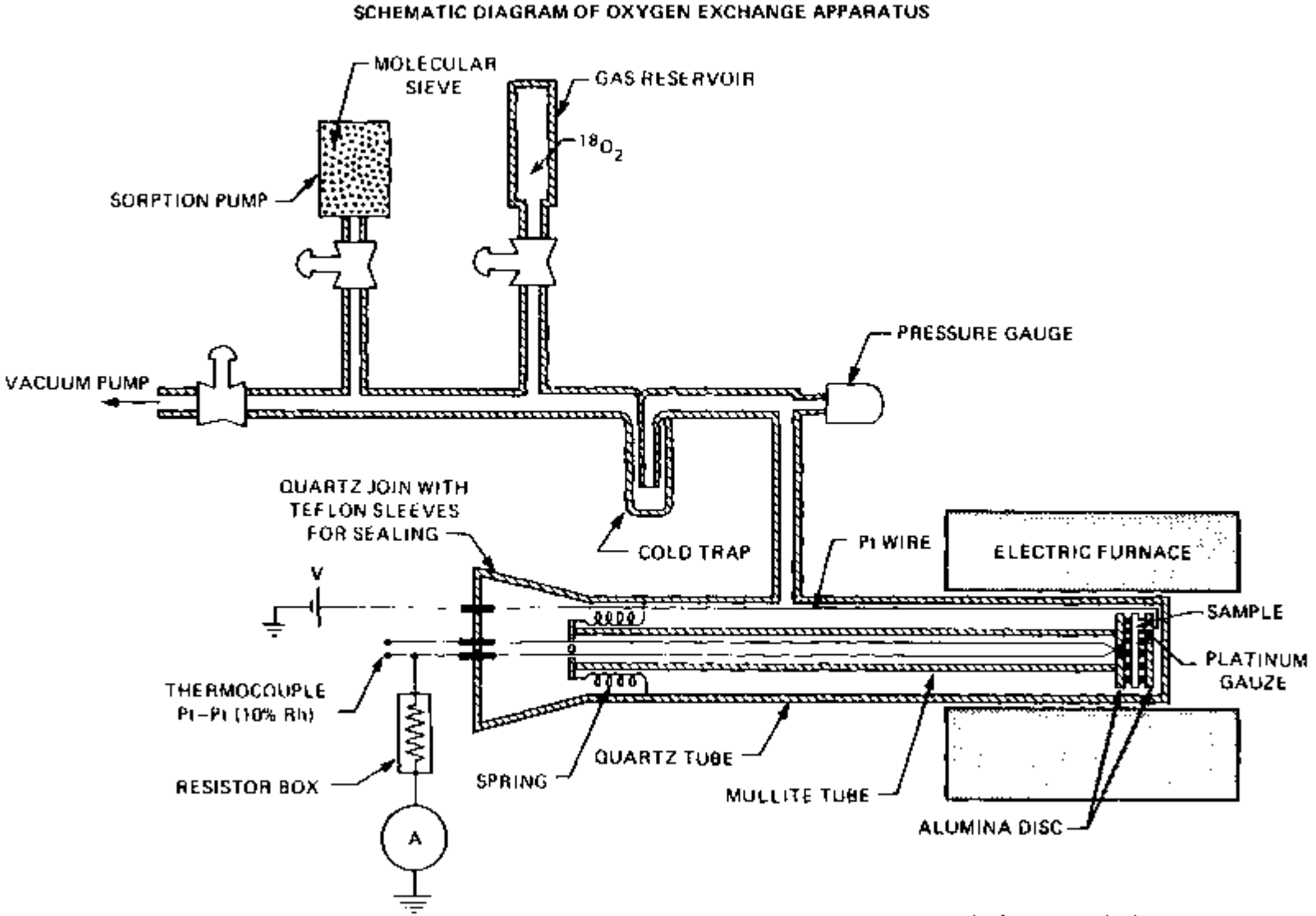

Fig. 4. Schematic diagram of the gas/solid isotope exchange experimental apparatus.

the variation of the isotopic concentration. The average isotopic concentration decreases ~15% with respect to the initial concentration regardless of the exposure time within the range of times of these experiments. Apparently the largest fraction of this variation is caused by the gas isotopic exchange with the furnace walls, stabilizing after 24 h.

The electric field was applied by an external power supply (PRL Electronics, Model CP-1413-V) and the current was measured by a digital electrometer (Keithley Model 616) in series with the sample, the power supply, and a resistance of 100 Ω (Variable resistance box, LEEDS & Northrup, Cat. No. 2164). Electrical connections to one of the electrodes was made by a Pt:Pt 10% Rh thermocouple which was also used to monitor the temperature of the sample. A thermocouple indicator (Doric Model DS-350) provided digital temperature readout. At the end of each anneal, the samples were cooled inside the furnace to room temperature at a cooling rate of ~10°C/min. Before withdrawing the samples, the remaining gas was stored in a sorption pump containing zeolite. The quartz tube was then filled with dry air and the sample withdrawn.

Nuclear analysis

The experiments described in this section were carried out by using a Van de Graaff accelerator able to reach a maximum energy of 2.5 MeV. An ion analyzing magnet is used to select the particle beam. The magnetic field of this magnet is adjusted in order to maximize the beam current detected by a Faraday cup. A nuclear magnetic resonance probe is used to measure the magnetic field. The magnetic fields from which half

of the maximum current was obtained were also measured in order to estimate the energy standard deviation ΔE. From these measurements ΔE was estimated to be 0.8 KeV. The ^{18}O concentration profile was determined by inducing the nuclear reaction $^{18}O(p,\alpha)^{15}N$ in the region of the resonant energy of 629 KeV. By varying the proton beam energy up to 750 KeV, the reaction was induced at increasing depths in the samples. For each incident proton energy, the nuclear reaction $^{18}O(p,\alpha)^{15}N$ produces α-particles which are distributed through a range of energy. As an example of such yield, Fig. 5 shows a typical α-particle spectrum obtained by bombarding a $Zr^{18}O_2$ film with 629 KeV protons. The integrated charge in this case was 10 μCoul.

To probe the ^{18}O concentration profile, the incident proton energy is increased, resulting in a similar yield for each selected energy. The integrated α-particle count of each spectrum is plotted as a function of proton energy, producing the excitation curve. The samples were mounted in a goniometric chamber with two degrees of freedom. Initially, the samples were oriented with (100) face normal to the incident proton beam. By tilting the target a few degrees off of this direction, the integrated nuclear reaction yield was maximized. At this orientation channeling effects did not affect the data. Erroneous depth profiles can be obtained if the crystal is oriented in the channeling direction with respect to the proton beam. The stopping power and the cross section for collisions with atoms in the channeling direction differ from the ones in a random orientation, where the probability of atomic collision is higher [52].

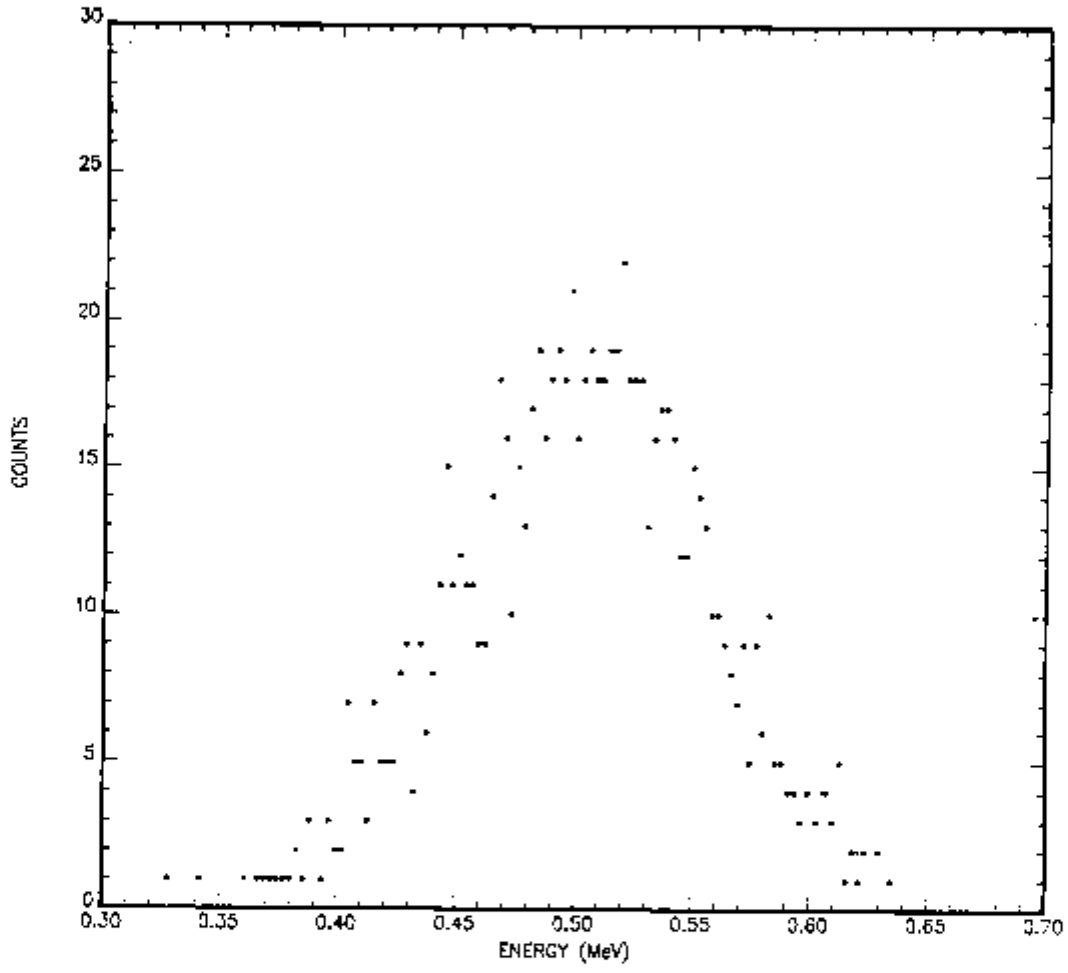

Fig. 5. Alpha particle spectrum of $Zr^{18}O_2$ film bombarded with 629 KeV protons: particle counts vs particle energy.

The α-particles produced by the reaction were detected through a silicon surface barrier detector (ORTEC Model TE-13-100-100) located 9 cm from the center of the goniometer, and making an angle of 150° with respect to the incident proton beam direction (see Fig. 6). A thin aluminized mylar film 0.50 mils thick covered the detector in order to shield it from backscattered protons. The beam current ranged from 50 to 150 namps and the integrated charge for each run was 20 μCoul.

A disc of zirconium containing a film of $Zr^{18}O_2$, 150 Å thick on the surface was used as a standard sample. This sample was prepared by anodic oxidation of zirconium in $H_2{}^{18}O$. The thickness of the film has been estimated by the values of voltage, current, and time interval adopted for the anodization process. This sample provided an energy calibration and standardized the parameters with respect to the variations of the accelerator conditions.

Complementary Rutherford backscattering (RBS) and channeling experiments were performed in some samples by using a 2 MeV α-particle beam. The mylar film was replaced by a metal plate with a 0.4x1.3 cm slit. The beam current ranged from 10 to 30 namps. For RBS, the samples were aligned 7° from the [110] direction and the azimuthal angle was varied during each run to avoid channeling and to provide a "random" spectra. The integrated charge was 20 μCoul. In the case of RBS in the channeling mode, samples were oriented with [110] direction parallel to the incident proton beam. The azimuthal angle was varied in order to minimize the integrated counts. The integrated charge was 60 μCoul.

A multichannel pulse height analyzer (MCA) was used to store the α-particles energy spectra. Each spectrum was subsequently transferred to

[illegible] NUCLEARES

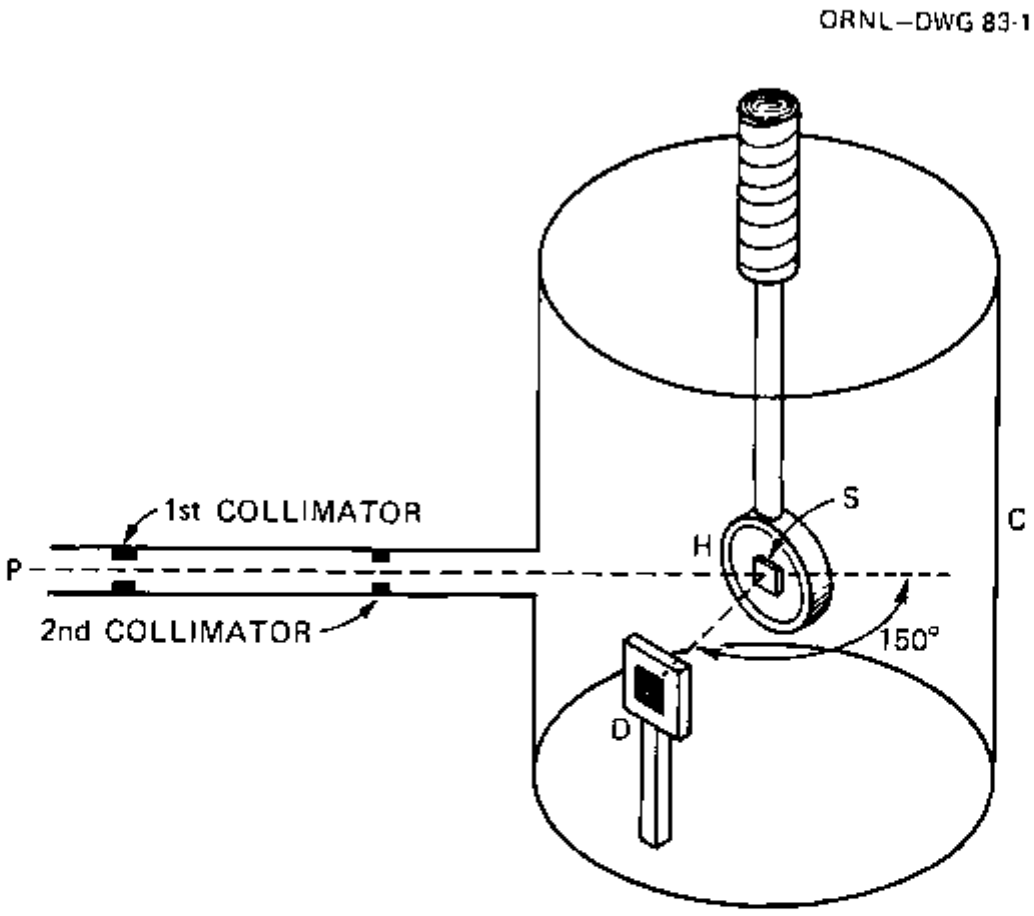

Fig. 6. Schematic view of the analysis chamber. P - proton beam, H - sample holder which can be rotated and pulled up and down, D - solid state detector, S - sample, and C - chamber.

a maynetic tape for computer analysis. Calibration of the multichannel analyzer was done by measuring RBS of pure C, Al, and Si samples.

CHAPTER IV

RESULTS

In this section the observed excitation curves are presented. In the discussion section, they will be compared with calculated excitation curves generated by convoluting assumed penetration profiles. From these excitation curves it is possible to determine diffusion parameters.

Initially, excitation curves obtained from $^{18}O^{+}$ implanted-MgO samples are shown as a function of annealing times and temperatures. These are followed by excitation curves from samples isotopically exchanged with $^{18}O_2$. Dependence on annealing parameters such as time, temperature, and electric field strength are included.

RBS spectra in both random and channeling modes are shown for samples exchanged with $^{18}O_2$, and exposed to electric field. Finally, data obtained from SEM of surfaces kept in contact with electrodes are presented.

Results from Implanted Samples

Figure 7 shows the excitation curves for a sample as implanted and after diffusion anneals at 1500°C/8h, 1200°C/75h, and 700°C/1h in air. In this chapter dash lines are drawn connecting experimental points in order to help visualize the experimental data. The background from an unimplanted sample which contains a natural concentration of 0.2% ^{18}O is 15 times less than the maximum number of counts obtained from a sample

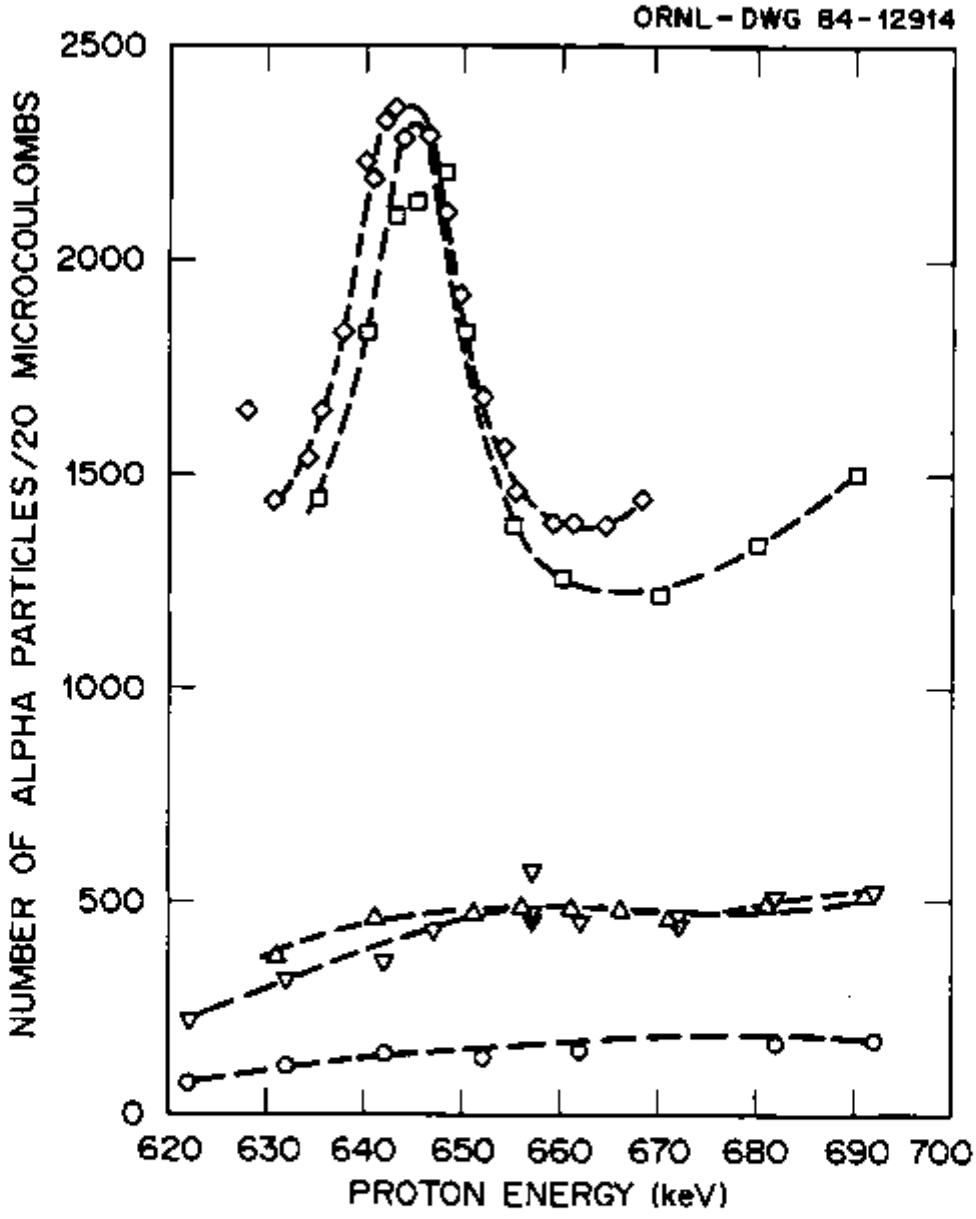

Fig. 7. Excitation curves for MgO single crystals implanted with 10^{17} ^{18}O ions cm^{-2}: (□) as implanted, (◇) after annealing at 700°C/1h, (△) 1200°C/75h, (▽) 1500°C/8h, (○) not implanted. Dashed lines are drawn to help visualize the experimental data.

implanted with 10^{17} ^{18}O ions cm^{-2}. Data in this figure were taken without checking channeling effects. It is observed that annealing at a low temperature (e.g., 700°C), does not significantly affect the implantation profile. However, annealing at higher temperatures (e.g., 1200°C and 1500°C) alters the implantation profile substantially as a result of a loss of implanted ^{18}O diffusing toward the implanted surface of the crystal. The remaining 20% of implanted ^{18}O is apparently moved deeper into the crystal. After this initial experiment it was realized that channeling might affect the results. The majority of implanted ^{18}O can only be observed when channeling is avoided since implantation leaves the lattice distorted, and ions occupy interstitial positions. However, annealing restores the lattice by relocating atoms in these positions. An example is shown in Fig. 8. This figure shows that an implanted sample, when analyzed in the channeling mode has a larger amount of implanted ^{18}O. After annealing at 700°C during 1 h in air (according to figure 6 little diffusion takes place), channeling of protons is observed in [100] direction because the total amount of ^{18}O detected is lower compared to the random spectrum taken by tilting the target 7° off that direction. In view of these results, all the subsequent measurements were done in nonchanneling directions.

Results from ^{18}O gas/solid isotopic exchange

A typical excitation curve from the nuclear reaction on a MgO sample equilibrated with $^{18}O_2$ gas is shown in Fig. 9. In this particular case the ^{18}O gas/solid isotopic exchange was performed at

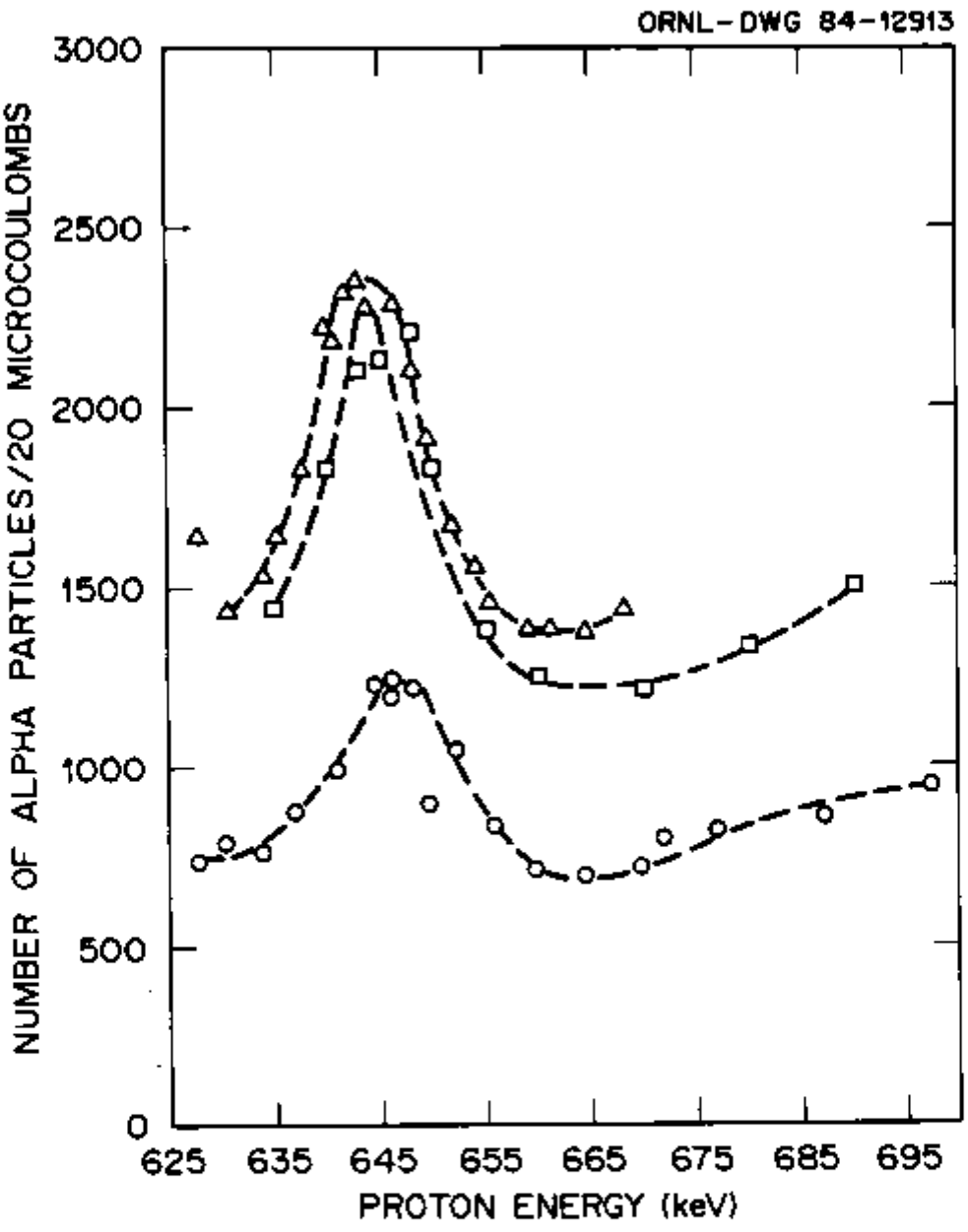

Fig. 8. Excitation curves for a MgO single crystal implanted with 10^{17} ^{18}O ions cm^{-2} showing the channeling effect: (□) as implanted and profiled in the [100] direction, (○) after annealing at 700°C/1h and profiled in the [100] direction, and (△) same annealing and profiled 7° off [100] direction. Dashed lines are drawn to help visualize the experimental data.

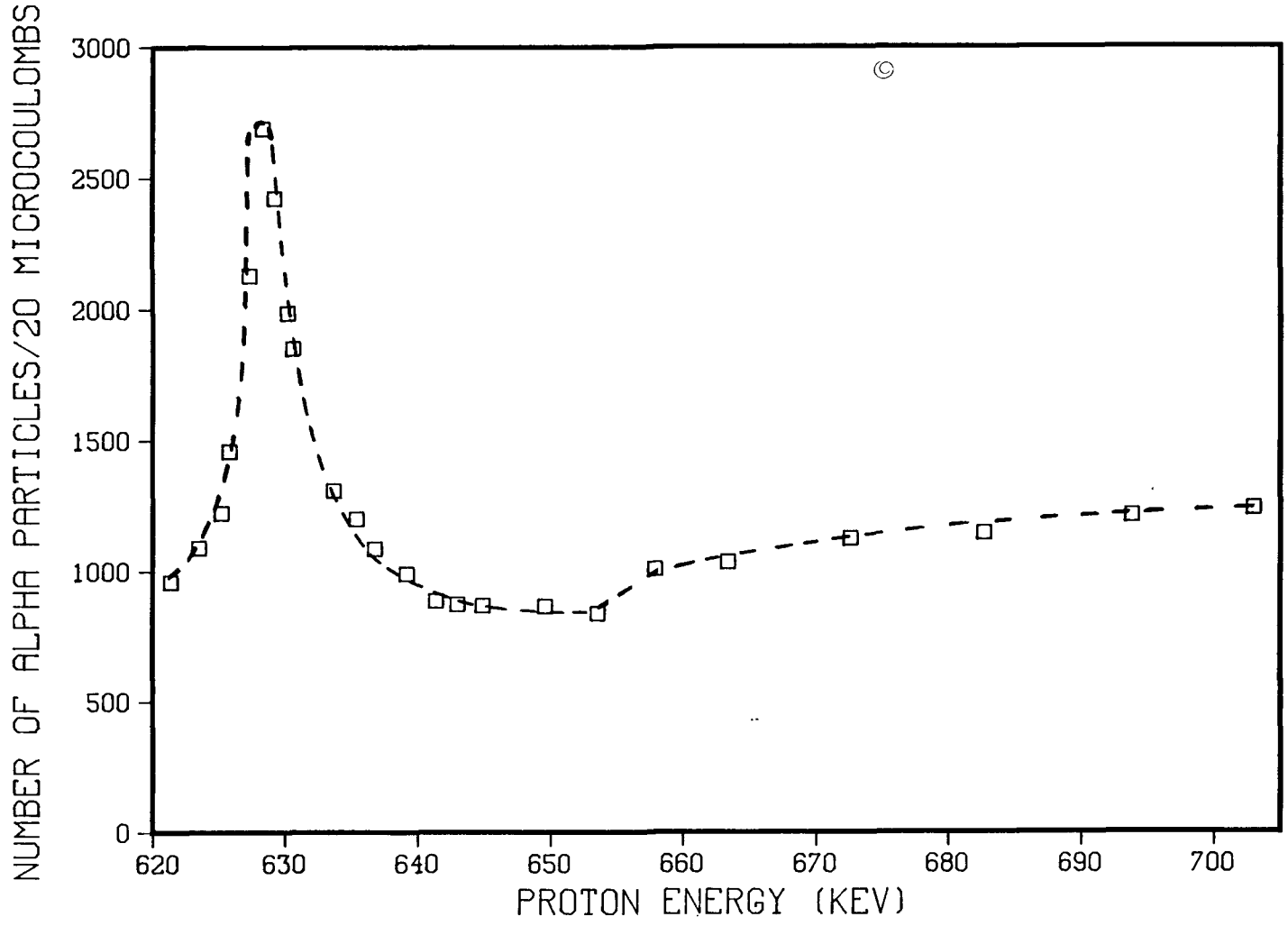

Fig. 9. Excitation curve for a MgO single crystal subjected to ^{18}O gas/solid isotopic exchange at 975°C/311.4h. The dashed line is drawn to help visualize the experimental data.

975±6°C during 311.4h. Excitation curves were also obtained for 894±3°C/48.1h, and 845±4°C/256.7h, resulting in similar curves.

The principal characteristics of these curves are a peak close to 630 KeV and a monotonic increase of number of α-particle counts at higher energies. The area under the peak is approximately related to the concentration of ^{18}O in the region near the surface. The increase of counts at higher energy does not indicate an increase in ^{18}O concentration deeper into the crystal, but does indicate an effect of the cross section of the nuclear reaction in this range of energy. This effect is taken into account by the convolution process.

Results from ^{18}O gas/solid isotopic exchange in the presence of an External Electric Field

The effect of an electric field on the excitation curves for proton bombardment is shown in Fig. 10 for a MgO sample subjected to a field strength of 90 V/cm, during a 48 hours $^{18}O_2$ gas/solid exchange at 936±2°C. Data from a sample under the same condition but without applied field is included for comparison. The cathode side of this sample exhibited a higher integrated particle count than did the anode side. Indeed, this is observed for all samples subjected to moderate electric fields. The anode side exhibited an excitation curve similar to the one obtained without applied field, except for a peak shift. This deviation is attributed to variations of the energy calibration of the Van de Graaff accelerator which occured between runs performed on different days. These variations are generally observed and related to the maintenance process of this machine. However, the area under the

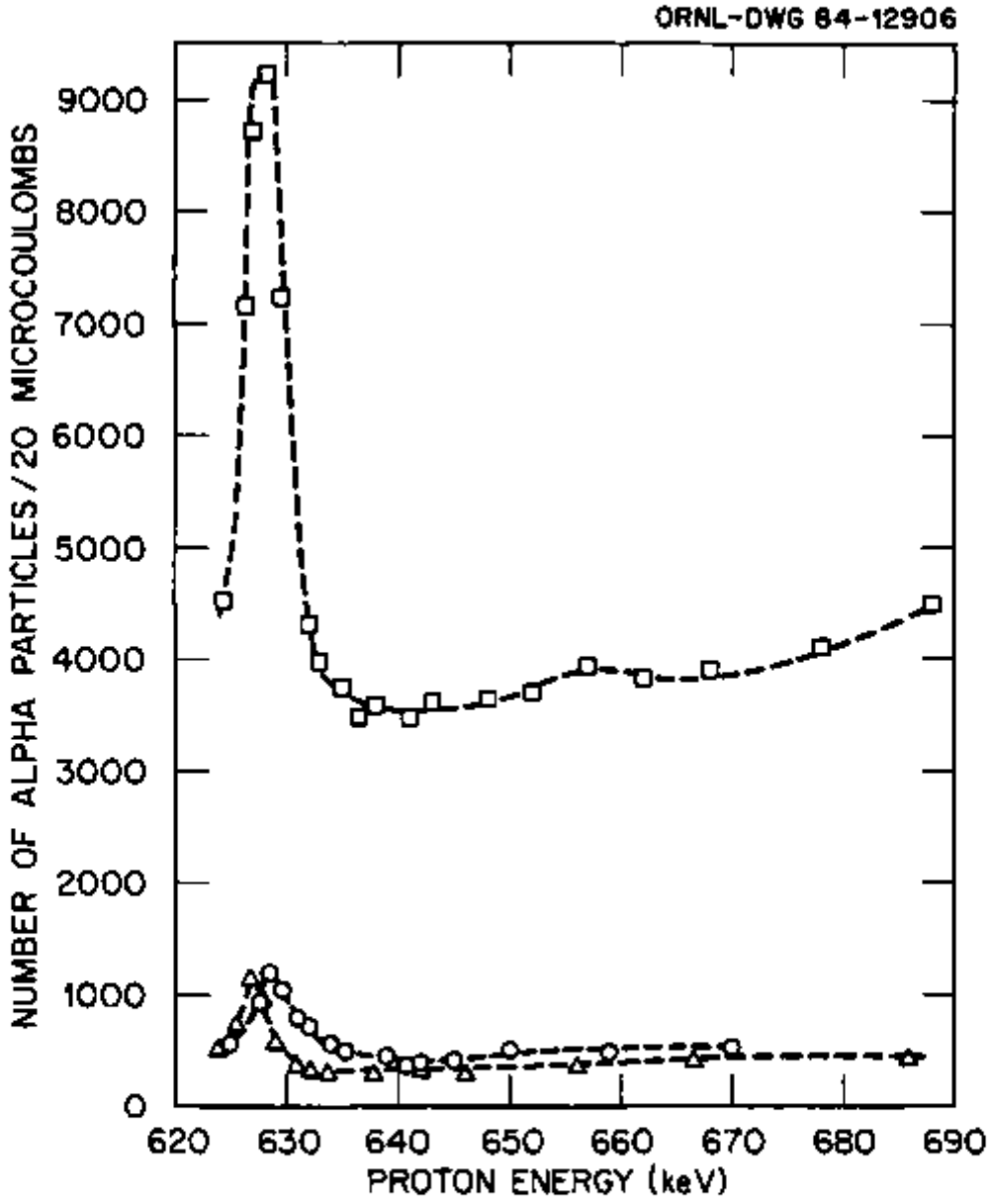

Fig. 10. Excitation curves for a MgO single crystal subjected to ^{18}O gas/solid isotopic exchange at 936°C/48h, and to an electric field strength of 90 V cm^{-1}: (□) cathode side, (○) anode side, and (△) no field. Dashed lines are drawn to help visualize experimental data.

excitation curve is the important parameter and it should not be affected by the peak shift.

The electric field strength dependences of the excitation curves are depicted by Figs. 11 and 12 for the cathode and anode faces. It should be noted that the ordinate scales for these two figures differ by more than an order of magnitude. These samples were exchanged with $^{18}O_2$ at a fixed time (24h), and temperature (930°C). From the area under the excitation curves of the cathode sides it is observed that the ^{18}O concentration in the region near the surface increases proportionally to the electric field strength. Moreover, the excitation curve for low electric field (10 V/cm) approaches the one in the absence of an electric field.

Although the areas under the excitation curves for the anode sides are similar to the ones without applied field, there is some variation, e.g., 90 V/cm, which cannot be explained in terms of electric field strength dependence. These anomalies will be discussed in the next chapter.

The time dependence of the excitation curves was measured by keeping the temperature (930°C) and the electric field (90 V/cm) at constant values, and by varying the isotopic exchange time interval. Figures 13 and 14 show the excitation curves for the cathode and anode side, respectively. For the cathode sides the ^{18}O concentration in the region near the surface is observed to increase proportionally to the exchange time interval. For the anode side the reverse conclusion is reached.

I. P. E. N.

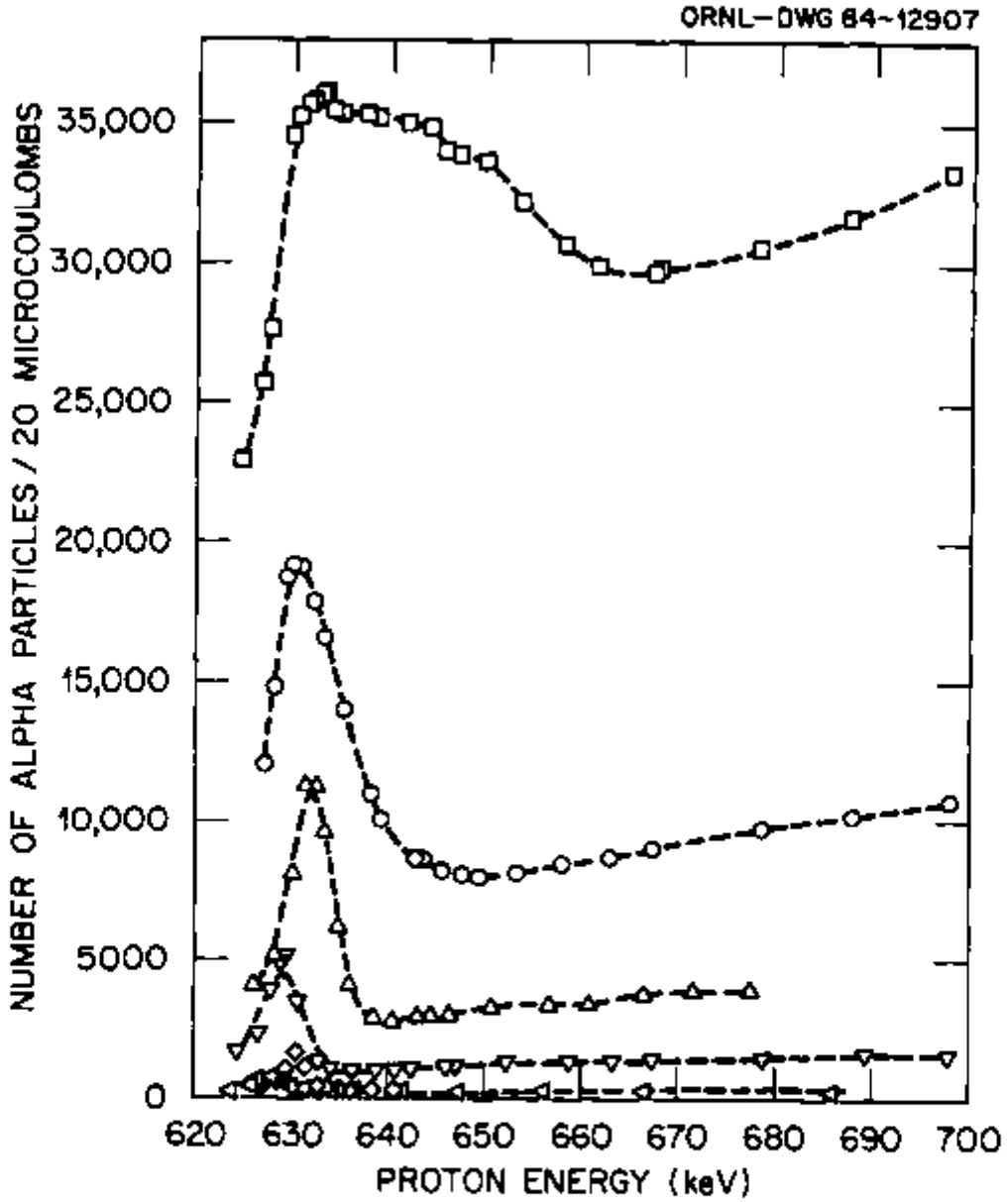

Fig. 11. Excitation curves from the cathode side of MgO single crystals subjected to ^{18}O gas/solid isotopic exchange at 930°C/24h and to electric field strengths of: (□) 3000 V cm^{-1}, (○) 1000 V cm^{-1}, (△) 300 V cm^{-1}, (▽) 90 V cm^{-1}, (◇) 10 V cm^{-1}, and (◁) no field. Dashed lines are drawn through data points to help visualize experimental data.

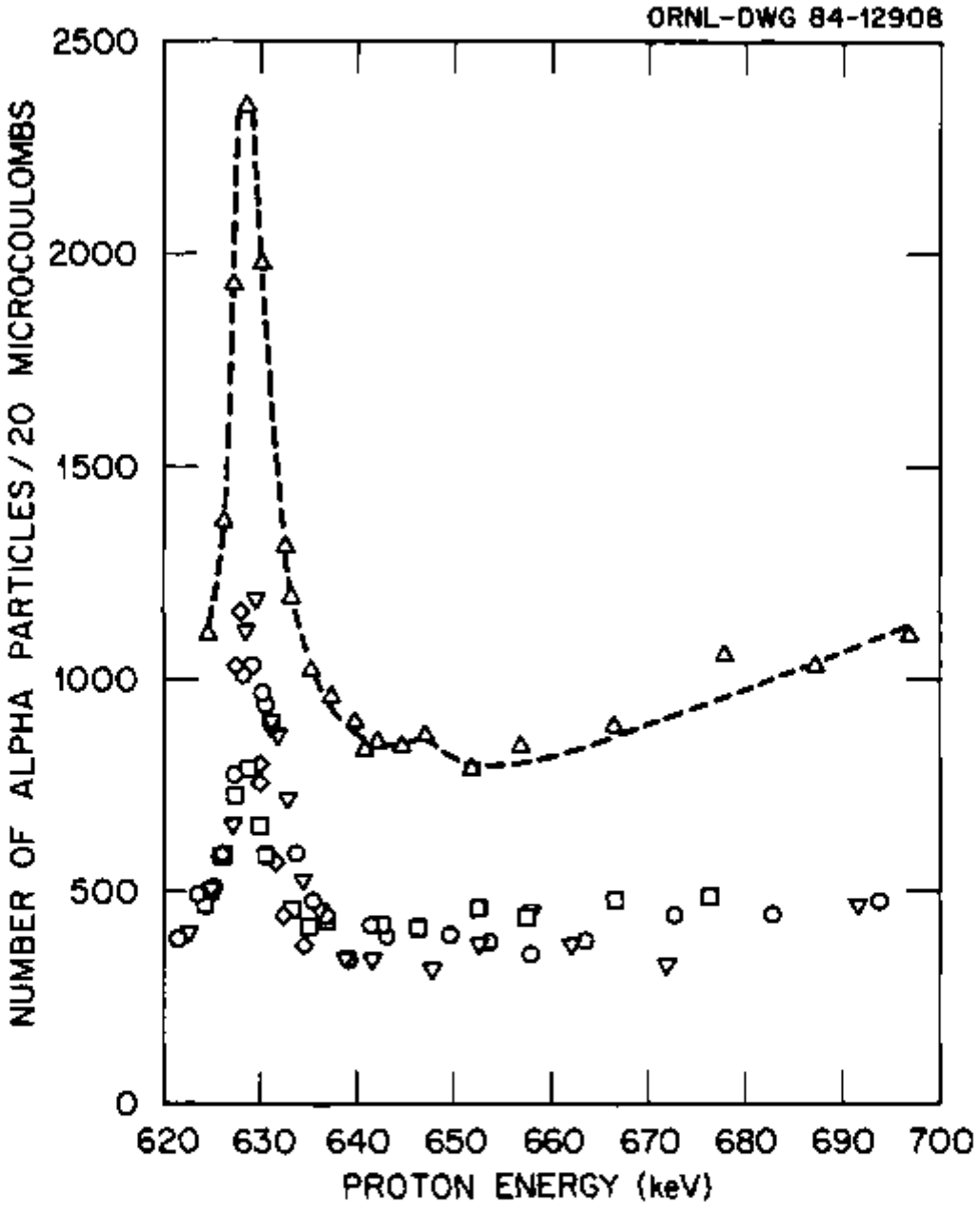

Fig. 12. Excitation curves from the anode side of MgO single crystals subjected to ^{18}O gas/solid isotopic exchange at 930°C/24h and to electric field strengths of: (□) 1000 V cm^{-1}, (○) 300 V cm^{-1}, (△) 90 V cm^{-1}, (▽) 10 V cm^{-1}, and (◇) no field. The dashed line is drawn to help visualize one set of the experimental data.

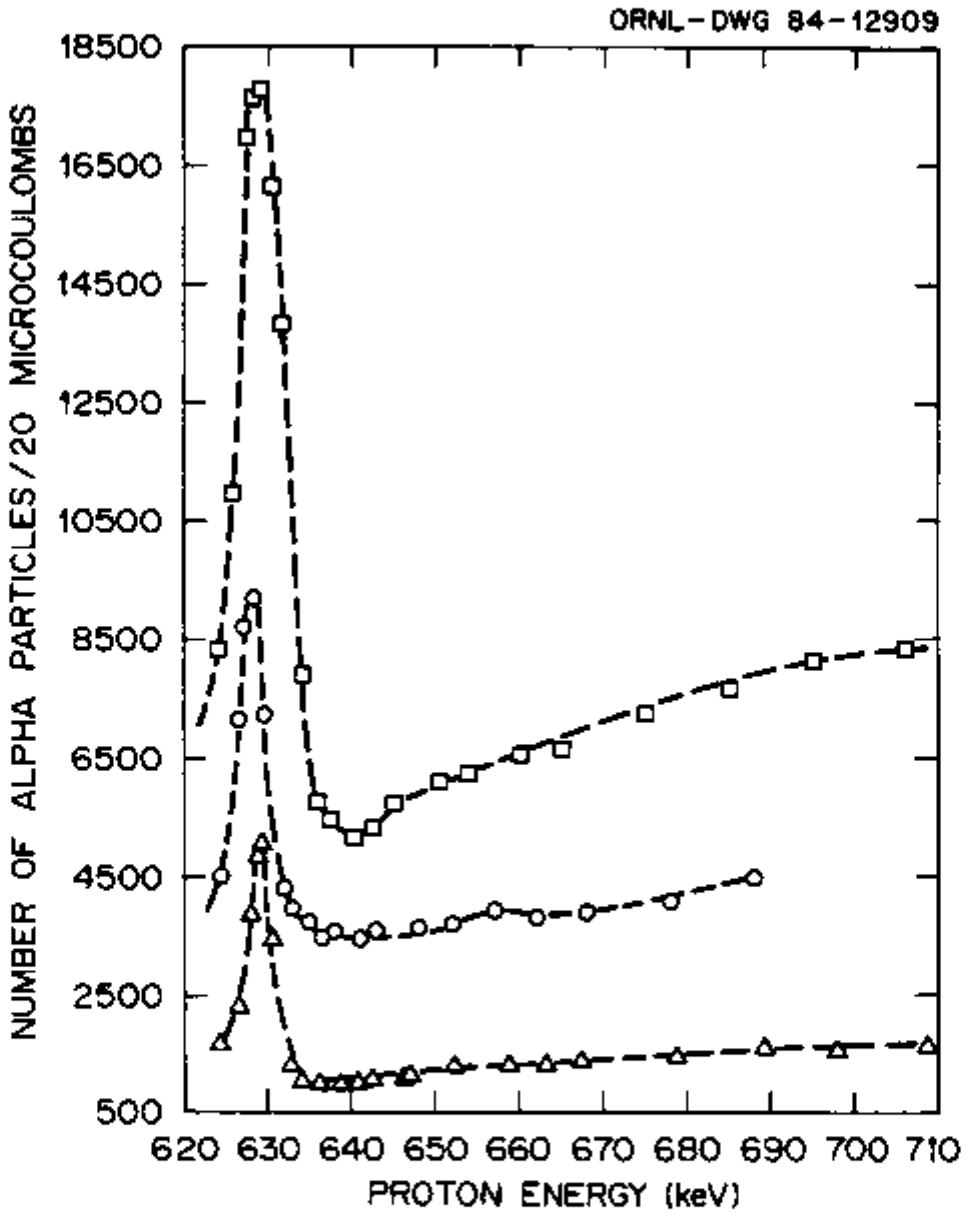

Fig. 13. Excitation curves from the cathode side of MgO single crystals subjected to ^{18}O gas/solid isotopic exchange at 930°C, and to an electric field strength of 90 V cm^{-1}. Time intervals were: (△) 24h, (○) 48h, and (□) 96h. Dashed lines are drawn to help visualize the experimental data.

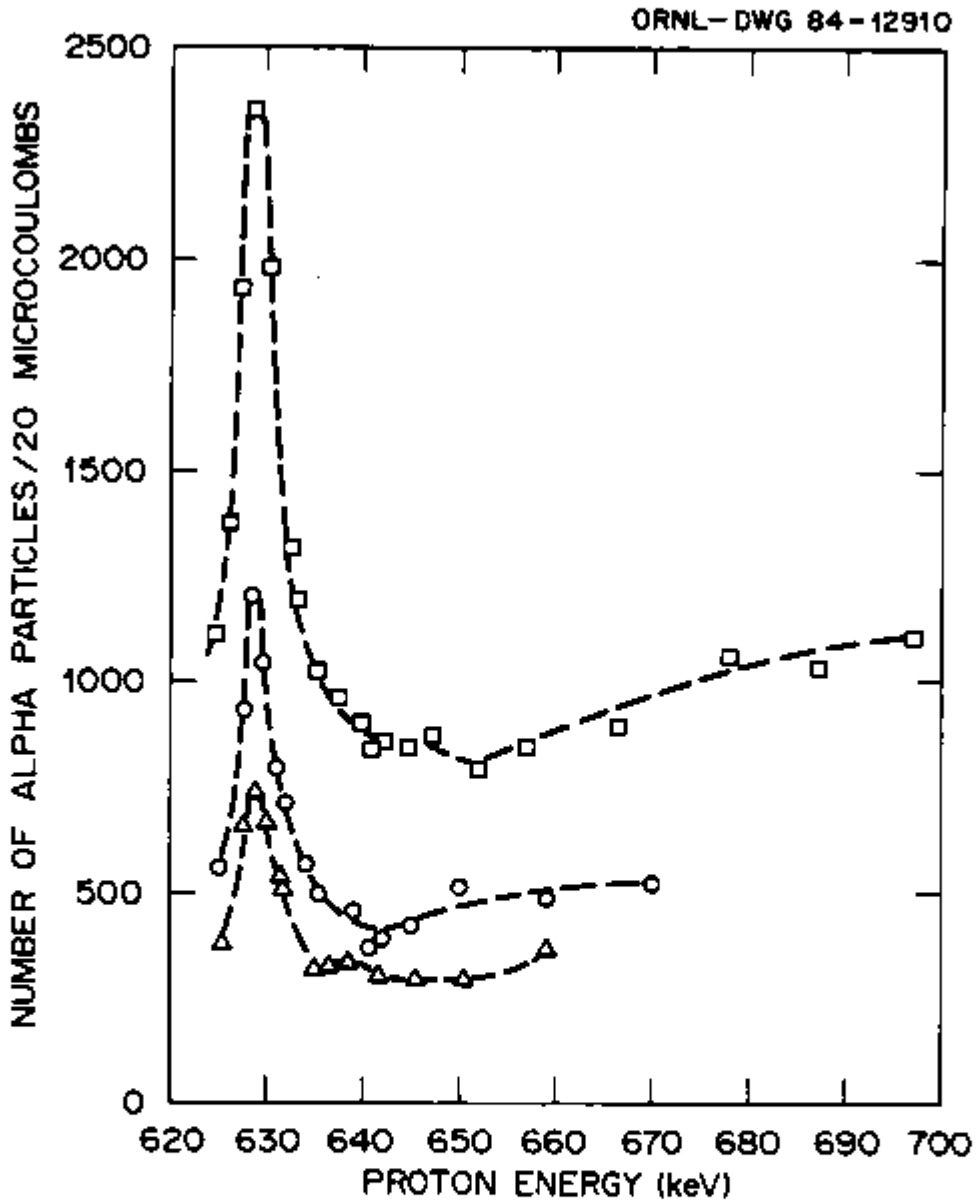

Fig. 14. Excitation curves from the anode side of MgO crystals subjected to ^{18}O gas/solid isotopic exchange at 930°C, and to an electric field strength of 90 V cm^{-1}. Time intervals were: (□) 24h, (○) 48h, and (△) 96h. Dashed lines are drawn to help visualize the experimental data.

Similarly, the temperature dependence of the excitation curves was also determined for both cathode and anode sides by keeping the electric field strength (90 V/cm) constant. The exchange time interval was fixed at 48 h for T > 890°C and 139 h for T < 890°C. Figures 15 and 16 show these results. The temperature dependence of the excitation curves is useful for determining the activation energy of the physical process responsible for the results obtained in this work. The variations of the areas under the excitation curves for the cathode side show an increase of ^{18}O concentration in the region near the surface, proportional to the increase of the temperature. The variations of the excitation curves for the anode side show the same behavior, except for the case where the temperature was 845°C.

RBS data

RBS in the random and channeling modes was performed on two samples in order to determine the location of the ^{18}O. One sample was isotopically exchanged with $^{18}O_2$ without field and the other in the presence of an electric field. Figure 17 shows the RBS spectrum in the random mode for a sample exchanged with $^{18}O_2$ at 960°C during 89 h. The steps indicated in the figure are due to the onset of ^{4}He scattering by ^{27}Al (previously deposited on the samples), ^{16}O and ^{24}Mg (substrate components). There is no evidence of scattering by ^{18}O. Figure 18 shows the RBS spectrum from the negatively polarized face of a sample subjected to the same procedure, but in addition to a 1010 V/cm electric field. This figure shows that ^{4}He scattering is due to ^{18}O, in addition to ^{16}O, ^{24}Mg, and ^{27}Al. Both spectra were obtained with crystals tilted

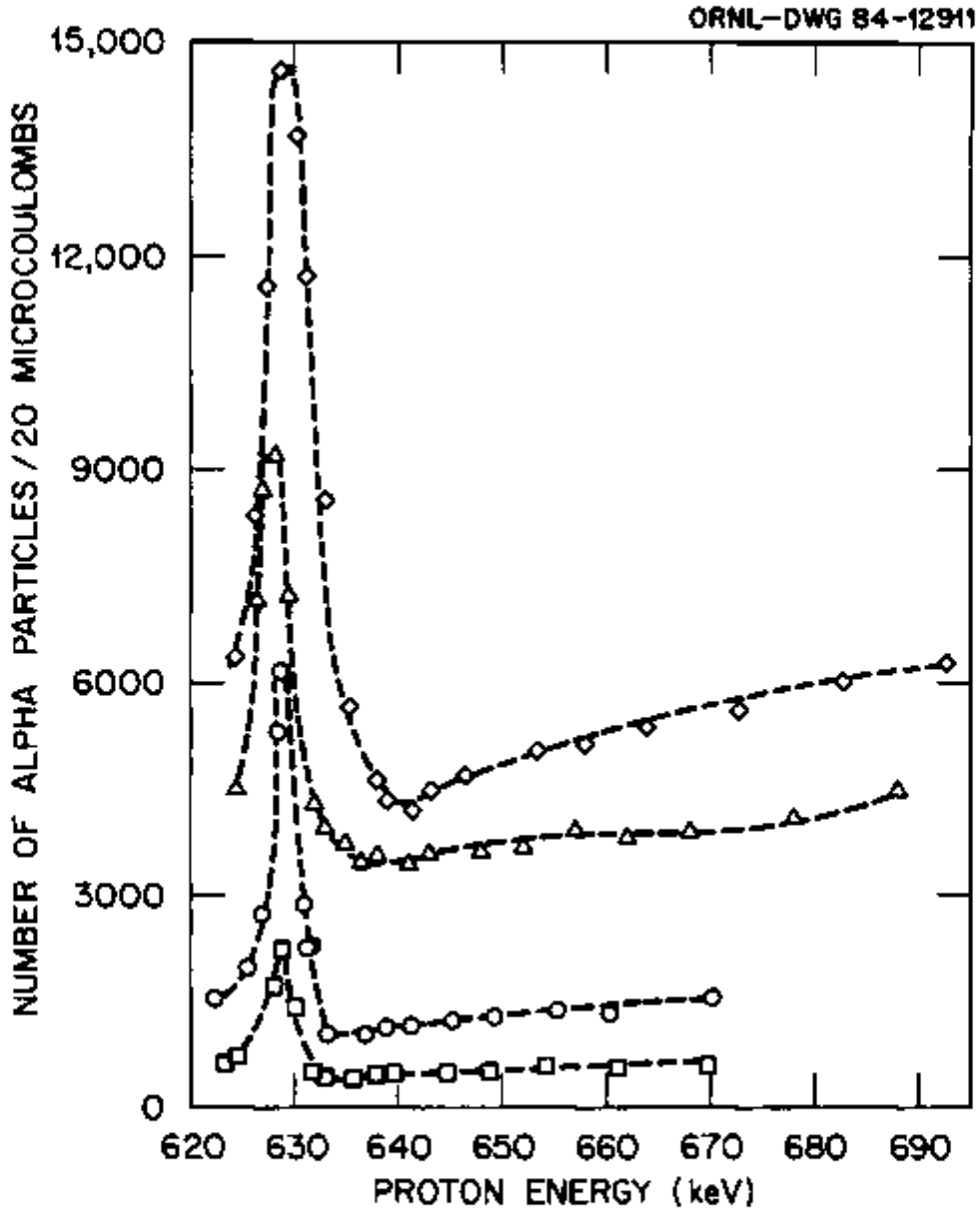

Fig. 15. Excitation curves from the cathode side of MgO single crystals subjected to an electric field strength of 90 V cm^{-1}, and ^{18}O gas/solid isotopic exchange at: (◇) 973°C/48h, (△) 936°C/48h, (○) 894°C 48h, (□) 845°C/139.1h. Dashed lines are drawn to help visualize the experimental data.

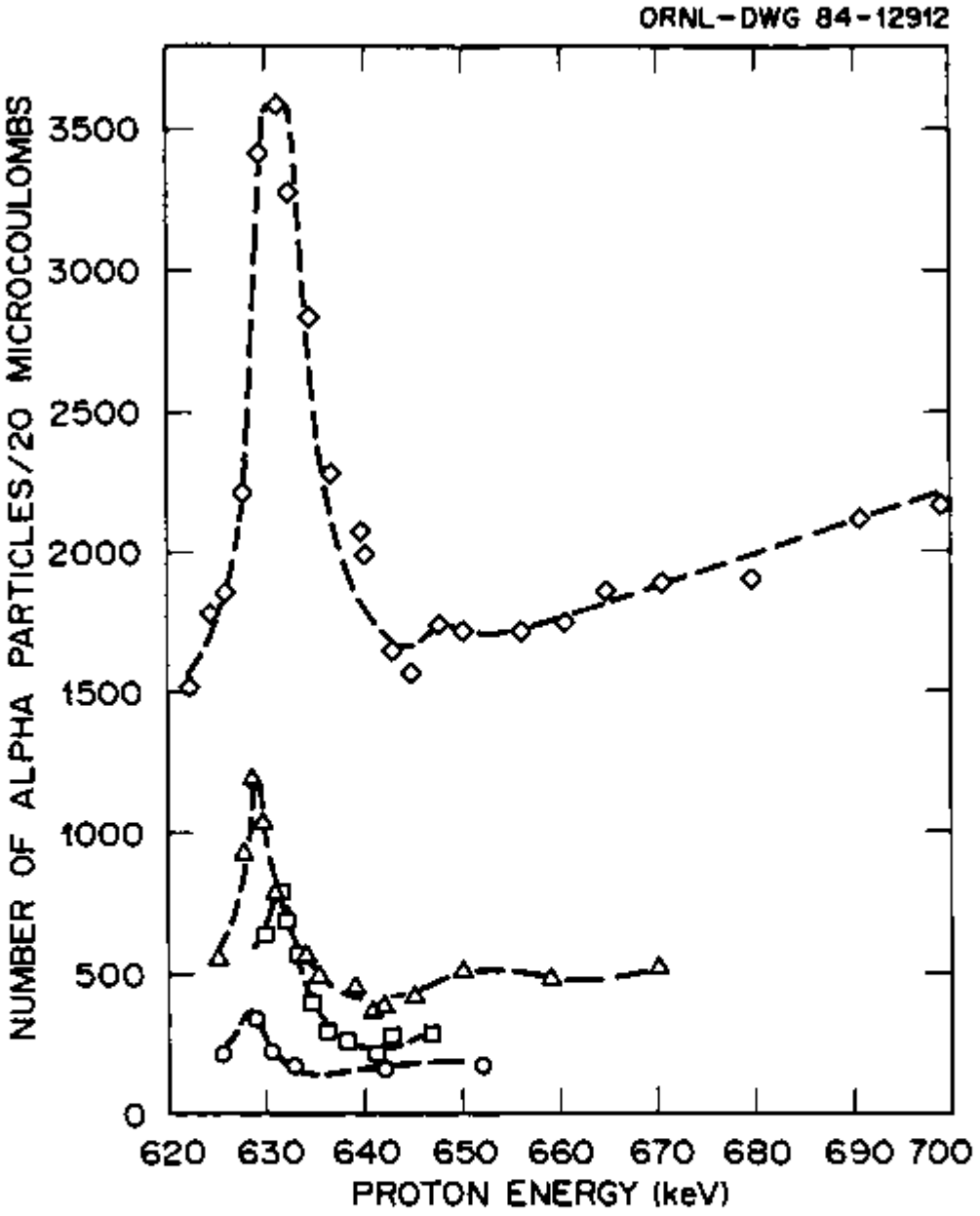

Fig. 16. Excitation curves from the anode side of MgO single crystals subjected to an electric field strength of 90 V cm^{-1}, and ^{18}O gas/solid isotopic exchange at: (◇) 973°C/48h, (△) 936°C/48h, (○) 894°C/48h, and (□) 845°C/139.1h. Dashed lines are drawn to help visualize the experimental data.

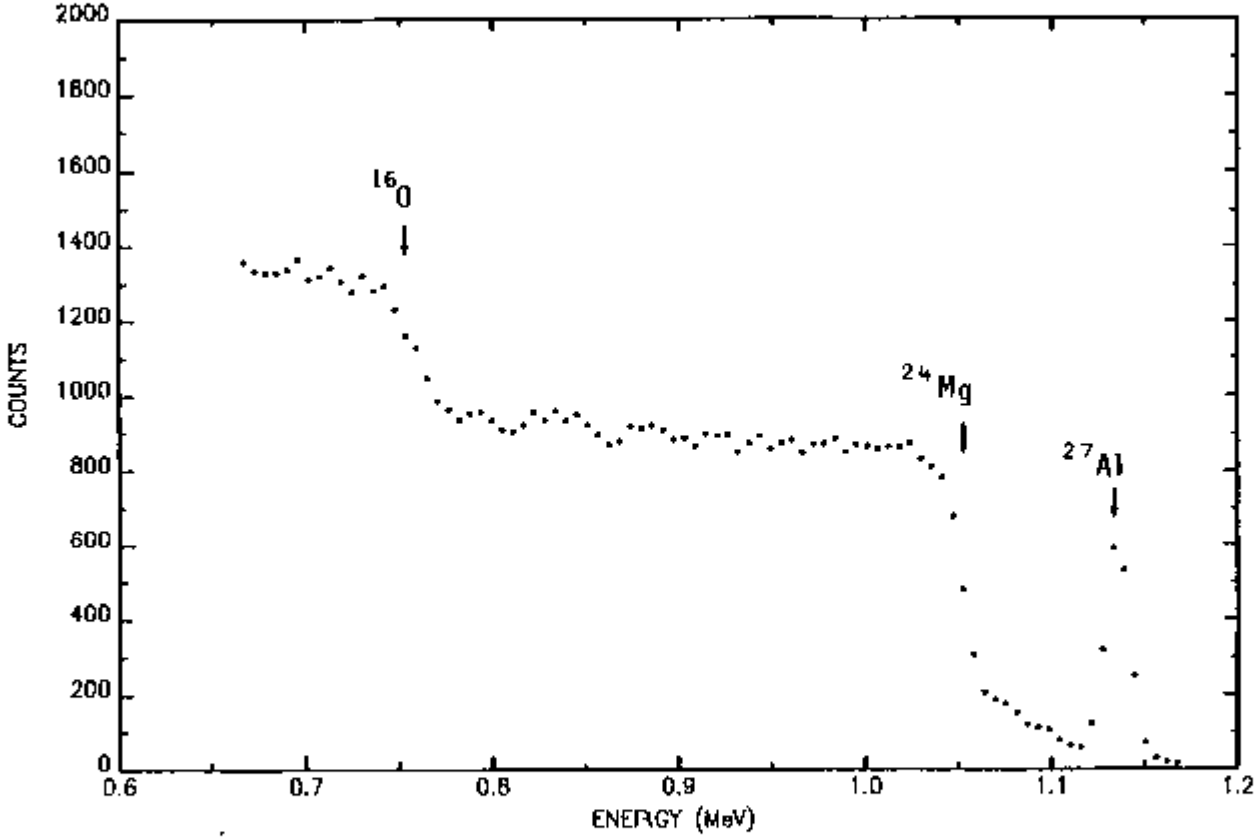

Fig. 17. RBS spectrum from a MgO single crystal isotopically exchanged with $^{18}O_2$ at 960°C during 89h.

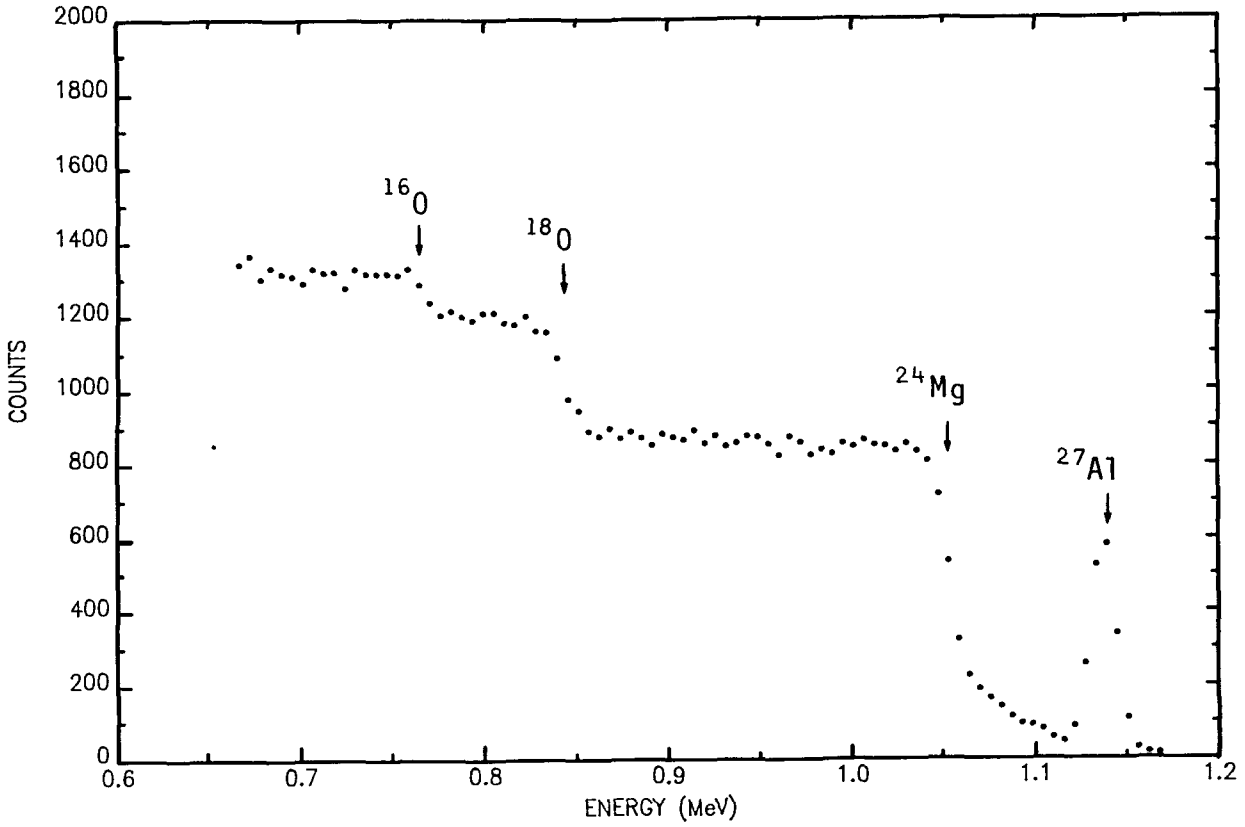

Fig. 18. RBS spectrum from the cathode side of a MgO single crystal subjected to 1010 V cm^{-1}, and isotopically exchanged with $^{18}O_2$ at 960°C during 89h.

7° off the [110] crystallographic direction, and constantly rotated in order to randomize the azimuthal angle.

Channeling was possible by orienting the crystals in such a way that the [110] direction coincided with the incident particle beam. Figures 19 and 20 show the RBS spectra in the channeling mode for the same crystals as used to obtain the random spectra (Figs. 19 and 20). Surface peaks for ^{27}Al, ^{24}Mg, ^{18}O, ^{16}O, and ^{12}C are observed in both spectra. These peaks are expected for ^{4}He scattering from atoms on the surface of the samples; no evidence of interstitial atoms or amorphous formation in the region near the surface was detected. The only observed difference between the data for the case without and with a field is a slight increase in the background when the field is present. Since they were taken from different samples, and the channeling optimization might vary due to misalignment, a small difference is expected.

SEM micrographs

Due to the different surface appearance of crystals subjected to electric fields, scanning electron micrographs were taken from crystal surfaces previously in contact with electrodes. Figures 21(a) and (b) show two of these micrographs at different magnifications. They were taken from the cathode face of a sample subjected to 1000 V/cm at 930°C during 24 h. The increased magnification used for Figure 21(b) provides a more detailed view of the surface modifications stimulated by the electric field. Figures 22(a) and (b) show SEM micrographs taken from the anode face of the same sample, using the same magnifications as Figures 21(a) and (b).

I. P. E. N.

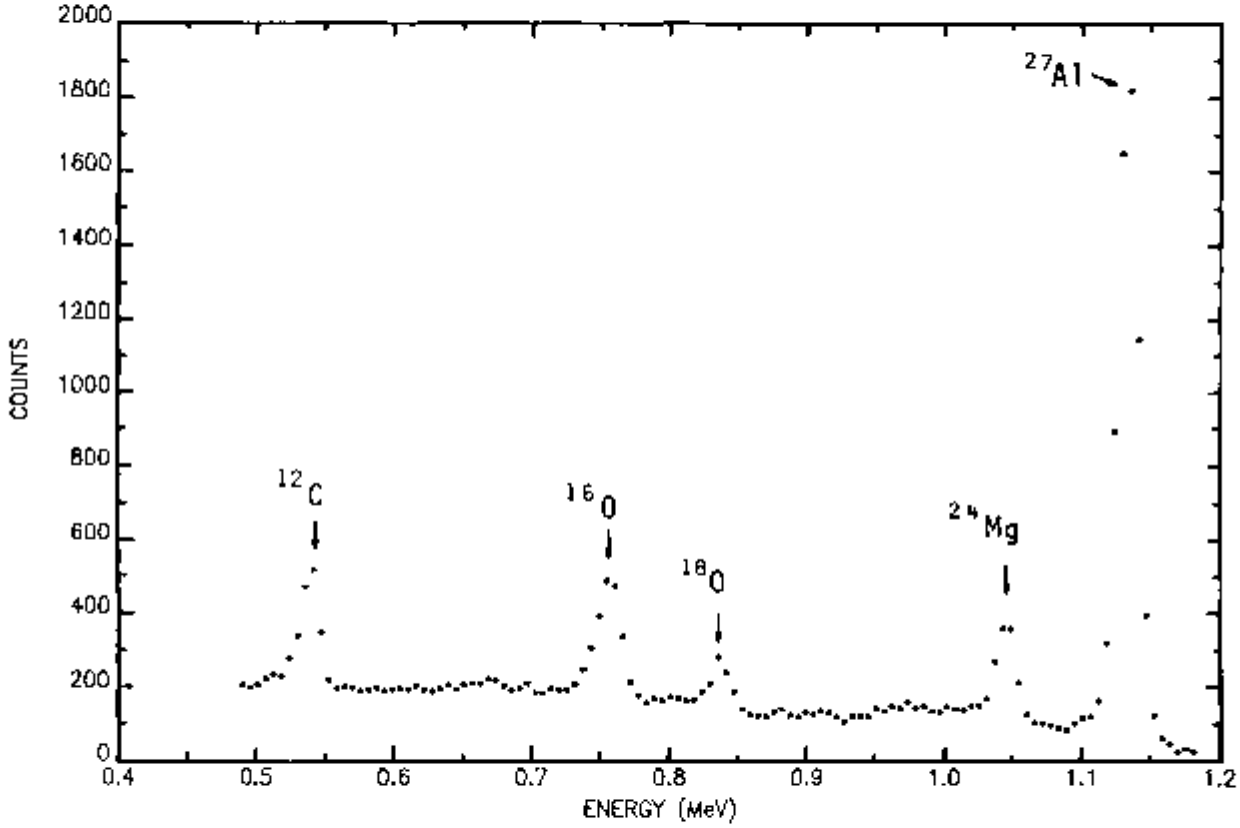

Fig. 19. RBS spectrum in the channeling mode from a MgO single crystal isotopically exchanged with $^{18}O_2$ at 960°C during 89h.

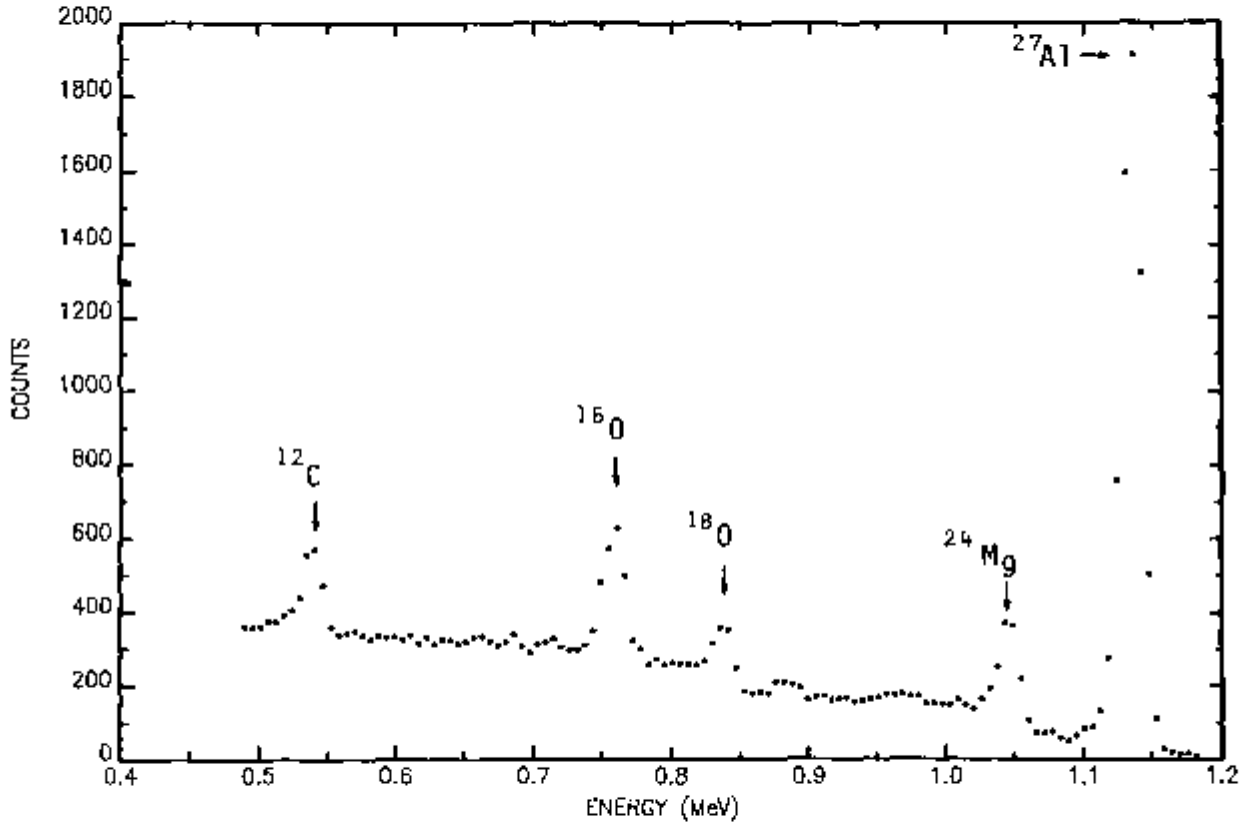

Fig. 20. RBS spectrum in the channeling mode from the cathode side of a MgO single crystal subjected to 1010 V cm^{-1} and isotopically exchanged with $^{18}O_2$ at 960°C during 89h.

a) 70X

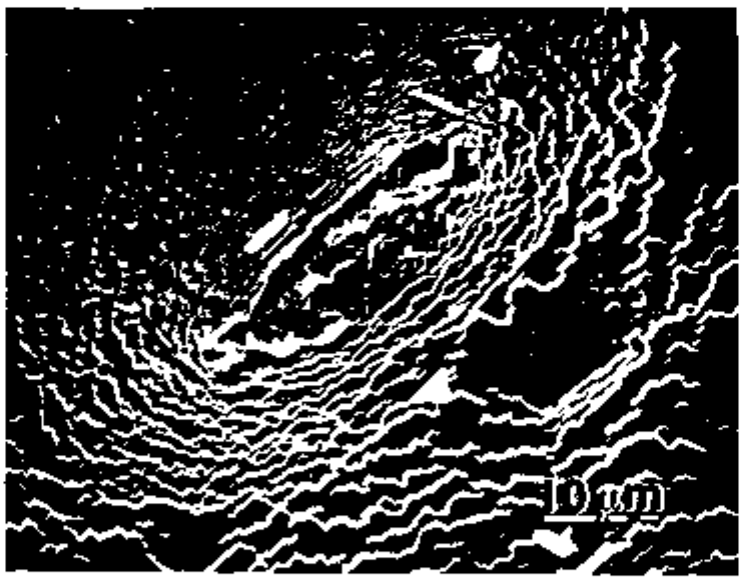

b) 700X

Fig. 21. SEM micrograph from negatively polarized surface.

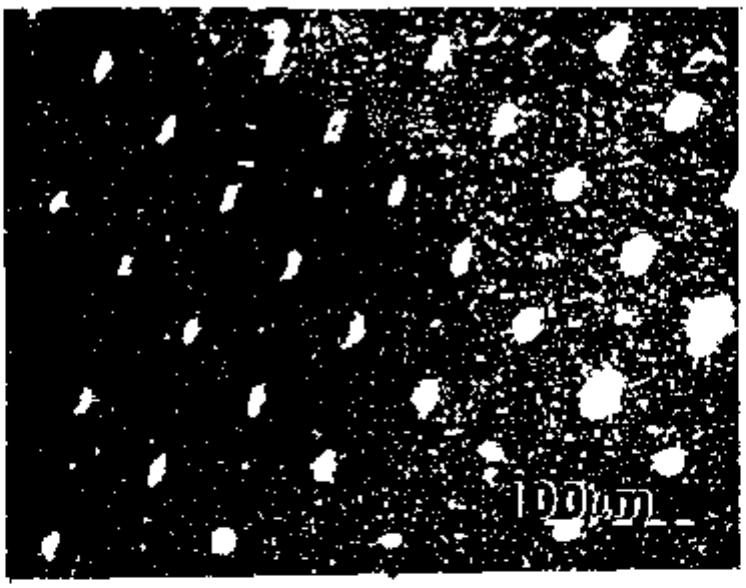

a) 70X

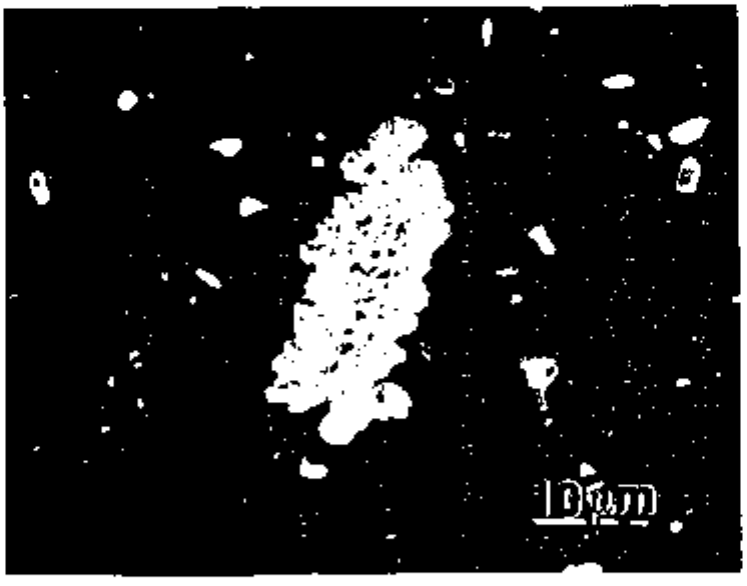

b) 700X

Fig. 22. SEM micrograph from positively polarized surface.

No alteration in the surface texture was observed from crystal surfaces exposed to field strengths < 300 V cm^{-1}. The dark area shown in Figure 22(a) is part of the region where the proton beam was incident. The micrographs taken at higher magnification (700X) show that the cathode and anode surfaces differ. Comparing micrographs shown in Figures 21(b) and 22(b), it is seen that the difference is not only on the contact points but also on the surrounding area. This area appears to be smoother on the anode surface than on the cathode surface. The roughness of the cathode surface might be an indication of the formation of a new oxide film, such as $Mg^{18}O$. However, stereomicrographs are needed in order to obtain the surface topological characteristics.

CHAPTER V

DISCUSSION

Development of a convolution program

A computational program has been developed in order to generate excitation curves from the convolution of an assumed concentration profile with the initial proton beam energy spread, particle energy straggling, and the finite width of the resonant cross section. A diagram of this program is given in Fig. 23.

For each incident proton energy E_p, the program convolutes the energy spreading with the differential cross-section values providing the probability of creating an α-particle at each depth. A matrix of such probability is calculated as a function of depth and then again convoluted with the assumed concentration profile in order to produce a calculated excitation curve. The parameters describing this concentration profile, e.g., diffusivity, surface exchange coefficient, and/or oxide layer thickness, are then adjusted by a subroutine, labeled DLMDF1,* in order to obtain the best fit. This subroutine minimizes the sum of squares of the difference between the calculated excitation curve and the observed one. The integrations necessary to convolute the concentration profile were done by using a subroutine, labeled SPLINT,** in

*B. S. Garbow, K. E. Hillstrom, and J. J. More, Minpack Documentation, Argonne National Laboratory, Argonne, IL, 1980.

**G. E. Forsythe, M. A. Malcolum, and C. B. Moler, Computer Methods for Mathematical Computations (Prentice Hall, 1977), pp. 89-90.

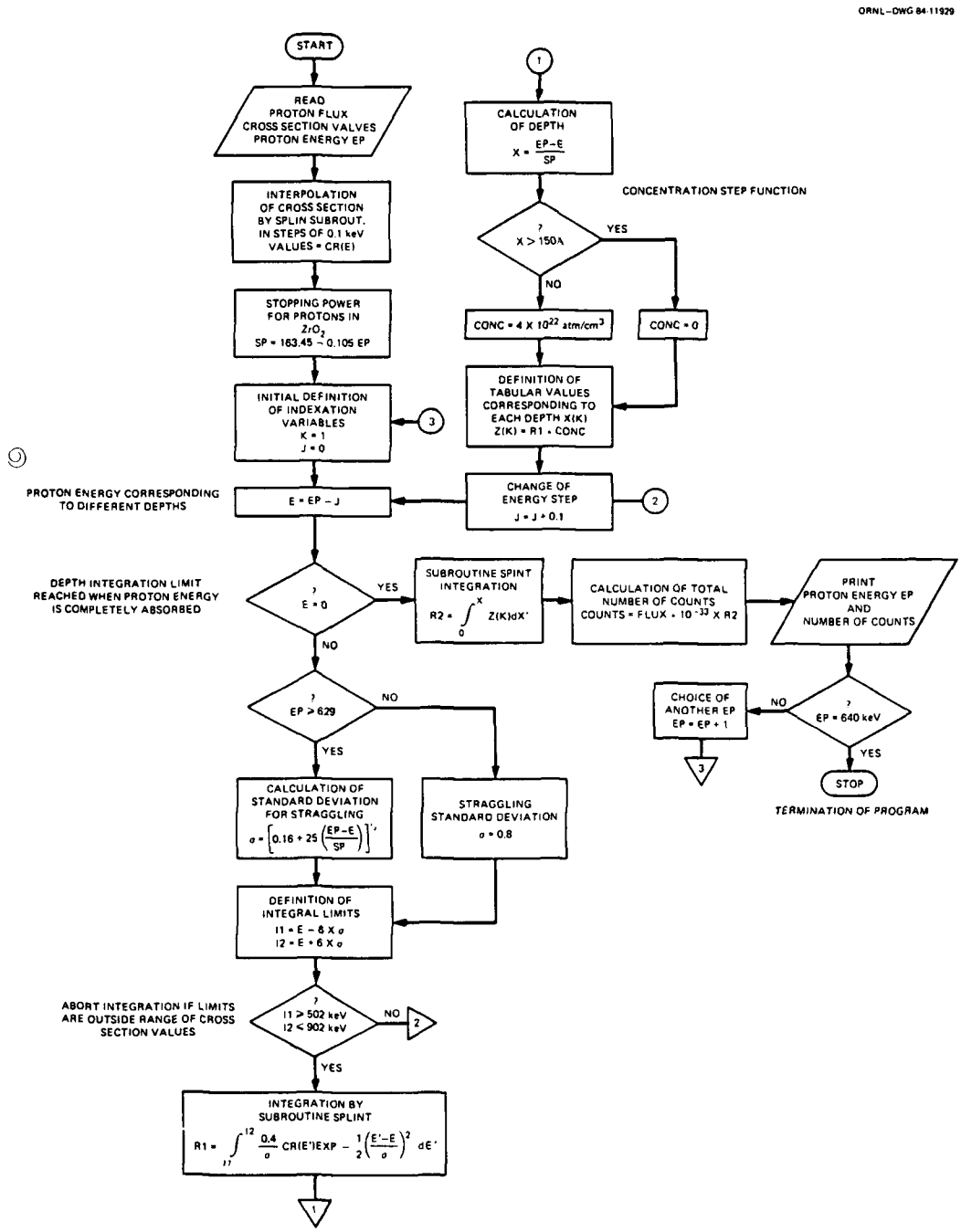

Fig. 23. BLOC diagram for computational program.

the library of the DEC-10 computer. Furthermore, the convolution program uses experimental cross-section values [51] interpolated in 0.1 KeV steps, instead of theoretical analytical expressions. The theoretical approach would introduce further assumptions.

To check this program, the experimental data obtained from the $Zr^{18}O_2$ standard sample was analyzed by using the following procedure: the concentration depth profile was assumed to be a step function with a constant ^{18}O concentration within the first 150 Å from the surface. This thickness has been previously estimated by the parameters of the anodization process. Beyond this depth the ^{18}O concentration was taken to be zero. Figure 24 shows both the experimental and calculated excitation curves. The points on this figure indicate the degree of agreement between the calculated curve and the experimental data to be expected in these experiments.

Implanted Samples

The results from implanted samples show a loss of ^{18}O after annealing at $T \geq 1200°C$, as indicated in Fig. 7. The reason for such loss is still not clear. It is possible that diffusion through the damaged area created by the implantation process is much faster than through the undamaged interior of the implanted sample. Intrinsic defects are created during implantation in MgO [53], both in the anionic sublattice (F, F^+, F_2-centers) and in the cationic sublattice (V^--centers). Excess defects would accelerate diffusion. A similar phenomenon has been clearly observed [54] for an Al_2O_3 single crystal implanted with Ti and Cr. RBS spectra obtained on this material in the

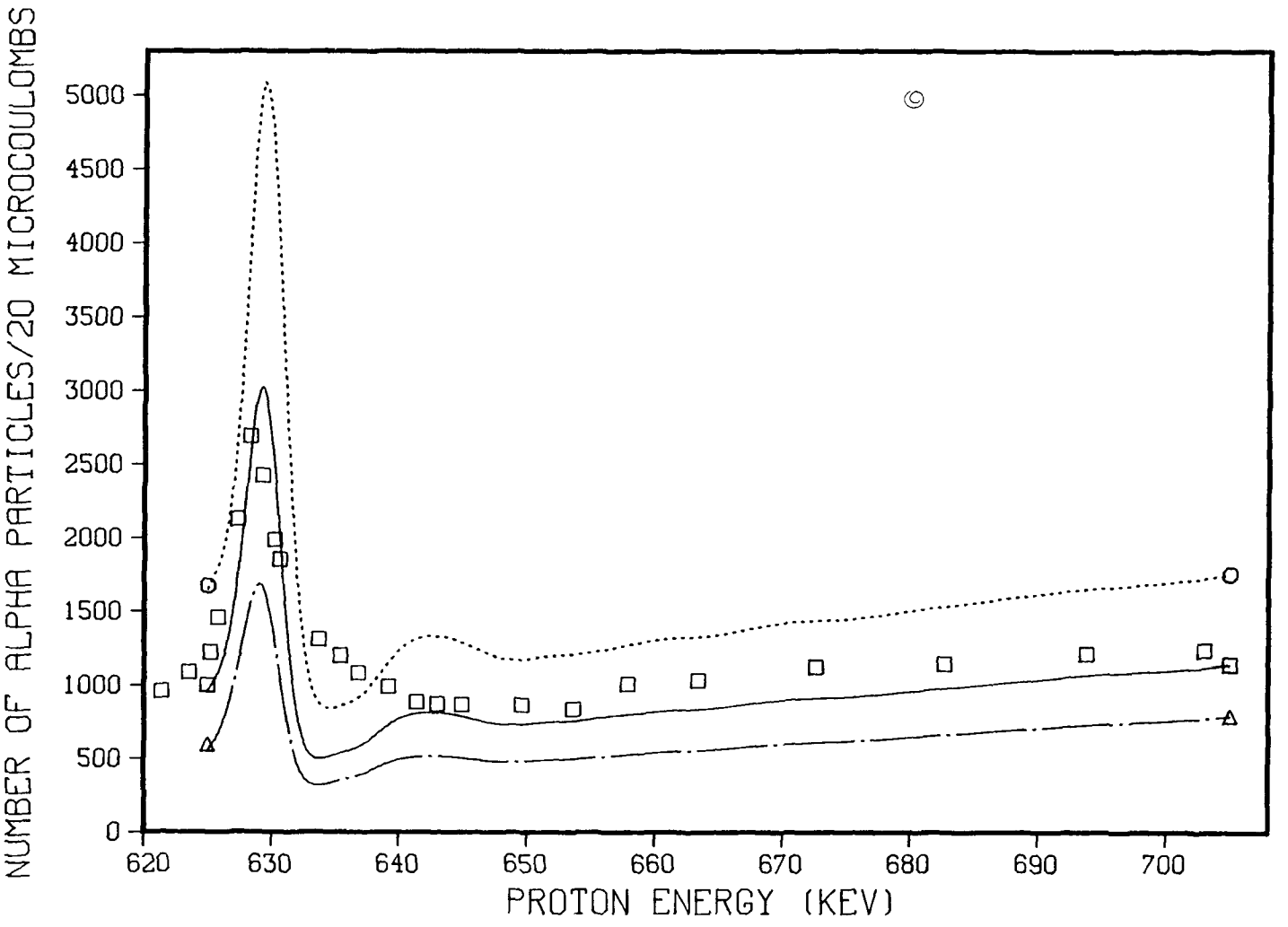

Fig. 25. Calculated excitation curves for proton bombardment on MgO single crystal subjected to $^{18}O_2$ gas/solid isotopic exchange at 975°C/311.4h. Solid line for $D = 2.4 \times 10^{-19}$ cm^2 s^{-1}; dotted line for $D = 7.4 \times 10^{-19}$ cm^2 s^{-1}; chain-dotted line for $D = 7.4 \times 10^{-20}$ cm^2 s^{-1}, (□) experimental points.

channeling mode show the creation of an amorphous layer due to the implantation process. They also show recrystallization due to annealing, and a loss of the initially implanted impurity.

Loss of implanted $^{18}O^{+}$ has also been observed in NiO single crystals [55]. For that material it is attributed to evaporation of NiO during diffusion annealing. By annealing two implanted NiO specimens simultaneously with the implanted surfaces in contact, the loss of ^{18}O was reduced. The same procedure was tried in the present work. Two MgO crystals implanted with 10^{17} ions cm^{-2} were annealed at 1200°C with the implanted faces in contact. The loss of ^{18}O was approximately the same as in the case of an uncovered face, i.e., none of the implanted ^{18}O was detected. Apparently two crystals in contact do not preclude the loss of implanted ^{18}O.

Figure 8 is interpreted by assuming that implanted ^{18}O ions occupy random positions in the crystal, i.e., both interstitial and lattice sites, precluding channeling of incident particles. However, after annealing at temperatures as low as 700°C, channeling is observed, indicating that implanted ^{18}O ions have left interstitial positions Therefore, channeling paths which were initially occupied are now empty.

To sum up, adopting this method of tracer introduction for self-diffusion studies requires full understanding of the behavior of the material during implantation as well as a systematic characterization of radiation damage and structure modification, and its consequence to the diffusion process.

I. P. E. N.

Analysis of Gas/Solid Isotopic Exchange Results

Oxygen self-diffusion coefficients in MgO were determined by using the computational program described previously to convolute equation 10 with the experimental factors. The parameters of equation 10, i.e., diffusivity and surface exchange coefficient were adjusted in order to calculate the excitation curves that best fit the observed ones. In Fig. 25 fits for different parameters are shown. The best fit, which is the least square calculated by the computer program, is shown by a solid line fitting the experimental data previously presented in Fig. 9. The calculated oxygen diffusivity for this particular temperature (975±6°C) was 2.4×10^{-19} cm^2/s, and the surface exchange coefficient was 5.45×10^{-10} cm/s. The same procedure was followed for samples subjected to different annealing time intervals and temperatures. Table 3 presents the diffusion coefficient values as a function of temperatures. These values are plotted in Fig. 26 in addition to values reported by other investigators.

TABLE 3

OXYGEN DIFFUSION COEFFICIENTS IN MgO

Temperature (°C)	time(s)	V(cm s^{-1})	D cm^2 s^{-1}
975±6	1,121,400	$(5.45\pm1.42)\times10^{-10}$	$(2.4\pm0.6)\times10^{-19}$
894±3	173,322	$(7.08\pm1.77)\times10^{-10}$	$(1.7\pm0.4)\times10^{-19}$
845±4	923,940	$(8.11\pm1.30)\times10^{-10}$	$(2.9\pm0.5)\times10^{-20}$

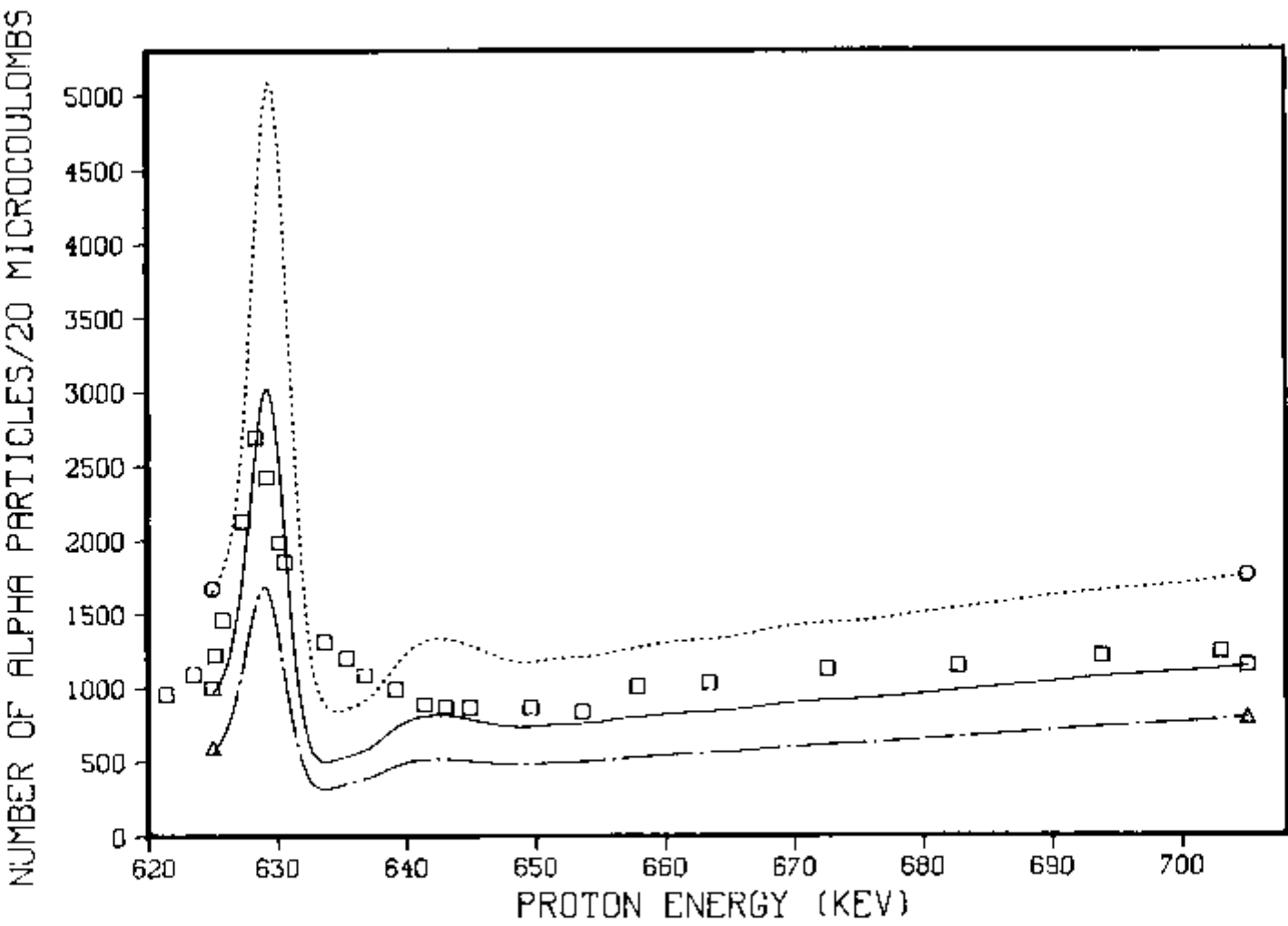

Fig. 25. Calculated excitation curves for proton bombardment on MgO single crystal subjected to $^{18}O_2$ gas/solid isotopic exchange at 975°C/311.4h. Solid line for $D = 2.4 \times 10^{-19}$ cm^2 s^{-1}; dotted line for $D = 7.4 \times 10^{-19}$ cm^2 s^{-1}; chain-dotted line for $D = 7.4 \times 10^{-20}$ cm^2 s^{-1}, (□) experimental points.

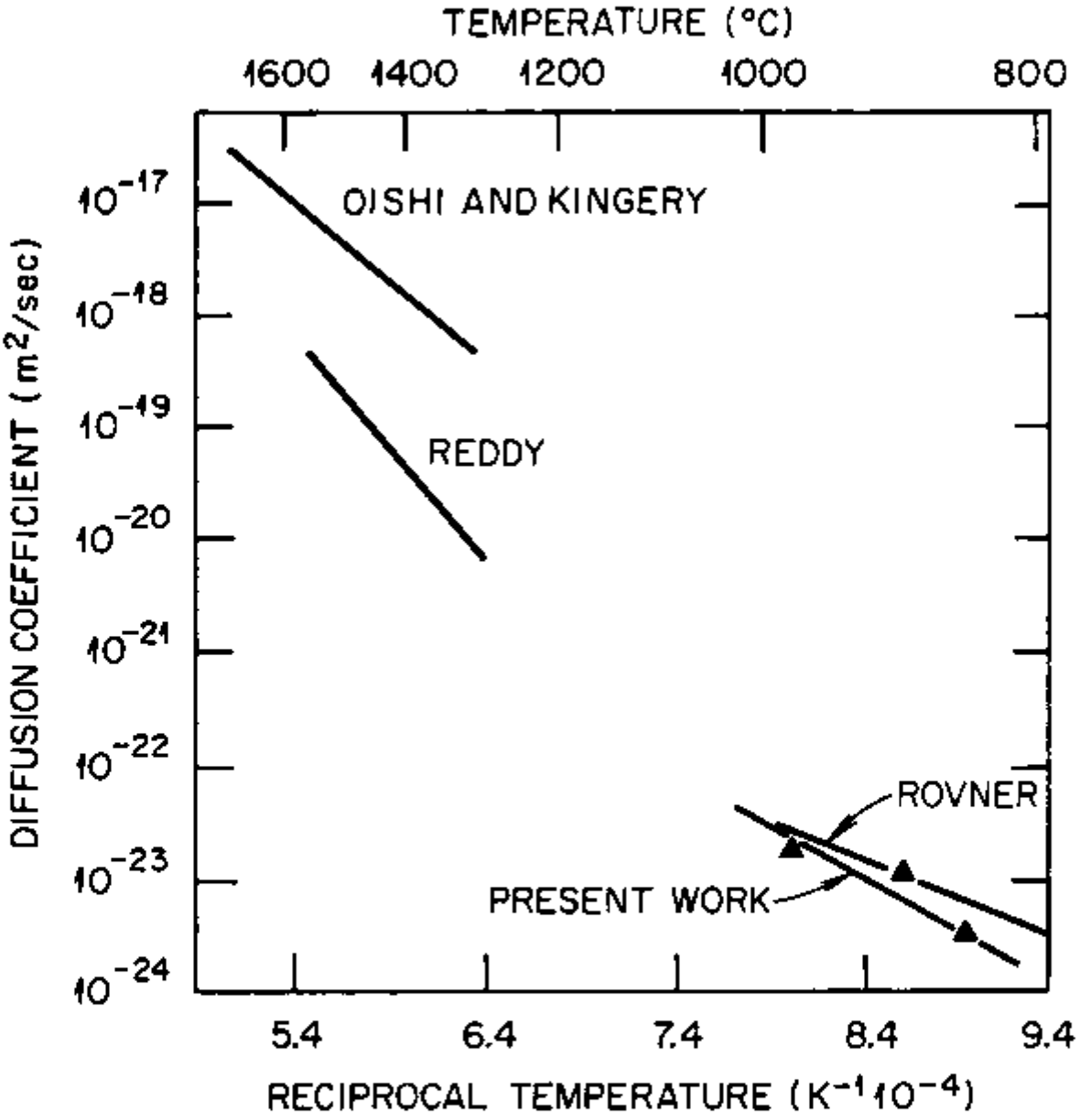

Fig. 26. Comparison of oxygen diffusion data in MgO single crystals. Oishi and Kingery, Ref. 31; Reddy, Ref. 29; and Rovner, Ref. 31.

The value 161±60 kJ/mole obtained by a least-square fit of the diffusivity versus the reciprocal of the absolute temperature (Fig. 26), is within the experimental error, in agreement with the one reported by Rovner [32], 125 kJ/mole in the so-called extrinsic region (750-975°C). The relatively large standard deviation for the activation energy value is caused by the experimental point taken at the shorter time interval (48h). At this time interval the concentration profile can be substantially affected by the surface exchange reaction. It has been demonstrated [30] that the effects of surface exchange reaction on concentration profiles will be greater in the initial stages of the exchange than in the final stages.

Analysis of Results from Gas/Solid Exchange with Electric Field Externally Applied

The same procedure described in the preceding section was initially attempted to determine the oxygen diffusion coefficient in the presence of electric fields; equation 15, instead of equation 10, was convoluted to calculate the excitation curve.

If the oxygen diffusivity values were assumed to be electric field independent and equal to that obtained in the absence of an electric field, the experimental excitation curves from the cathode faces could not be fitted. A diffusivity two orders of magnitude higher did provide a reasonable fit. But even then the field strength dependence depicted in Fig. 11 could not be fitted.

A simple calculation shows that the displacement of the concentration profile caused by the electric field, $\Delta x = \mu E \Delta t$, is of the same

order of magnitude as the depth penetration, $x_{\alpha}2\sqrt{D\Delta t}$ for the experimental conditions. The electric fields used in the present work were too small to produce a measurable difference between the concentration profiles in the absence of a field and that with a field. Therefore, excitation curves in these two cases should be similar for a set of parameters corresponding to a short diffusion run. Figure 27 shows the calculated excitation curves obtained for ^{18}O diffusion without field, and in the presence of 300 V/cm. Indeed, the difference between them is too small to be observed. However, Fig. 10 shows the observed excitation curves for a sample subjected to 90 V/cm. Even for this low field, a large difference is observed between the excitation curves for the cathode and for the anode faces. Therefore, the results are inconsistent with only an oxygen diffusion process.

Another mechanism of mass transport is proposed to explain these results: ionized magnesium vacancies V''_{Mg} drift to the anode causing a corresponding drift of magnesium ions to the cathode. At the cathode these Mg ions react with $^{18}O_2$ forming a Mg ^{18}O layer. Since magnesium diffusion is some orders of magnitude greater than oxygen diffusion in MgO, such a mechanism can produce the very large effects observed. The field strength and time dependence of the excitation curves are consistent with a mechanism of mass transport of magnesium induced by an electric field. If this process is assumed, then the thickness of the formed oxide film can be used to deduce the mobility of Mg ions, and the cationic transference number. From these, the Mg self-diffusion coefficient can be calculated.

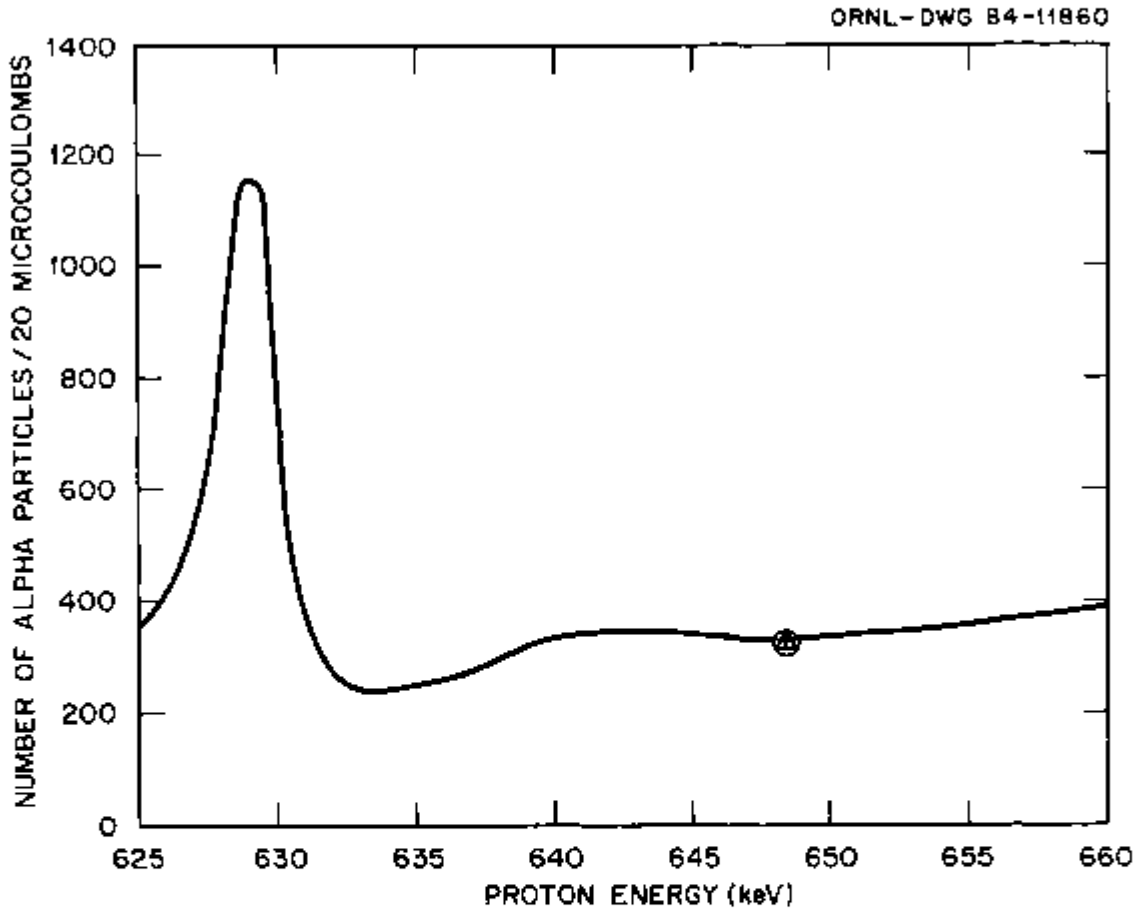

Fig. 27. Calculated excitation curves assuming oxygen diffusion in a MgO single crystal subjected to: (O) no field, (+) +300 V cm^{-1}, and (Δ) -300 V cm^{-1}. The differences in the curves are too small to be shown on this figure.

For the convolution calculation, the ^{18}O concentration profile of the $Mg^{18}O$ film is approximated by a step function with a nonzero constant value from the surface of the material to some depth. Beyond this depth, it is assumed that the concentration profile is controlled by ^{18}O thermal diffusion with an applied electric field. For the sake of completeness, equation 15 is used, although as discussed above the electric field has no measured effect on the ^{18}O diffusivity. The $Mg^{18}O$ film thickness, Δx, is adjusted in order to obtain a best fit between the calculated excitation curves and the observed ones.

As discussed early in this chapter, the convolution process produces "theoretical" excitation curves from given concentration profiles. Such curves are compared with the experimental data and adjusted to fit it. However, there is a finite number of experimental points taken at energy values that differ by 1 KeV, which correspond to approximately 100 Å in a depth scale. Therefore, it is estimated that, due to the limit imposed by the experimental resolution, a detailed shape curve cannot be resolved for depths smaller than 200 Å. The determination of the total amount of ^{18}O provide a quantitative analysis in these regions. For high penetration depths, the experimental resolution is sufficient to provide a shape resolution for the excitation curves. For these cases the experimental data cannot be fitted with any reasonable diffusion profile caused by oxygen diffusion. Profiles having a step function shape give reasonable fits. For simplicity, a step function was used in each case since it is consistent with the physical nature of a growing oxide film. It should be noted, however, that better fits

were obtained if an ensemble of step functions were used. It may be that such an ensemble represents irregularities of the actual surface.

The mobility and diffusivity of V''_{Mg} are calculated from equations 28 and 29, respectively. The vacancies are present as charge compensation due to the presence of Fe^{3+}, Al^{3+}, and Cr^{3+} impurities. The vacancy concentration is estimated from equation 4 by using the detected impurity concentration (see p. 29). Any error in this estimation affects only the absolute value of the diffusion coefficient, but not the activation energy for migration. The V''_{Mg} concentration will be affected by impurity precipitation which happens over a range of temperatures. Processes such as precipitation of impurities and dissolution of precipitates might be indicated by a sharp change in the activation energy observed over a range of temperatures.

The experimental excitation curves shown in Fig. 15 are now replotted in Figs. 28, 29, 30, and 31 along with the calculated excitation curves. These curves show a secondary peak between 645 and 650 KeV caused by the increase of cross section values and decrease of ^{18}O concentration. Experimentally this peak has not been resolved. The oxide film thickness corresponding to the oxidation of Mg ions drifted to the cathode is then determined from these fits as a function of temperature. The calculated mobility and diffusivity are given in Table 4 and are plotted in Figs. 32 and 33, respectively, as a function of reciprocal temperature. The activation energy is calculated by the least-squares fit of the three points at $T \geq 1168$ K to equation 11. The solid lines in those figures show the best fit of equation 11.

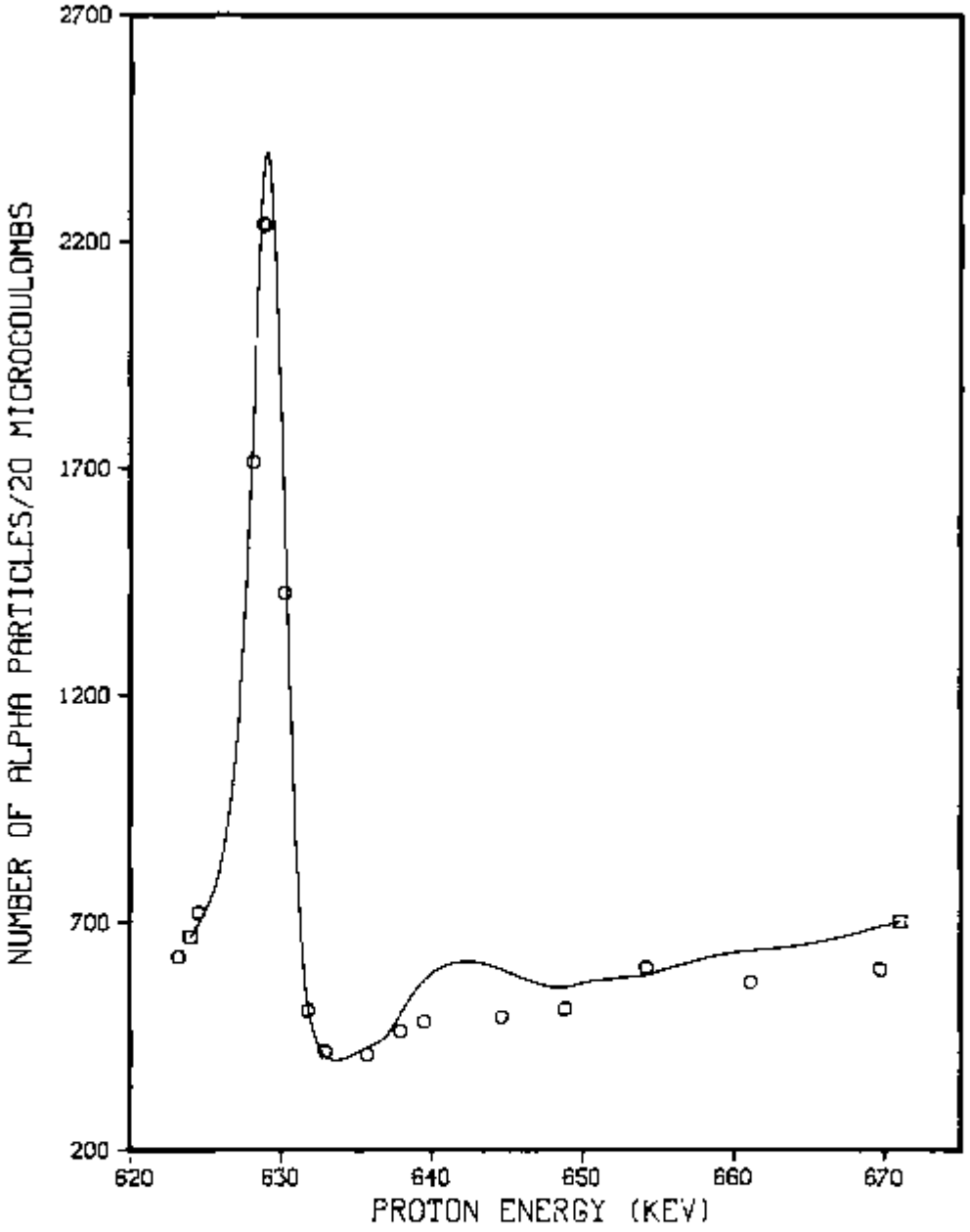

Fig. 28. Calculated excitation curve for the cathode side of a MgO single crystal isotopically exchanged with $^{18}O_2$ at 845°C/139.1h in the presence of an electric field of 90 V cm^{-1}. Experimental points are included for comparison.

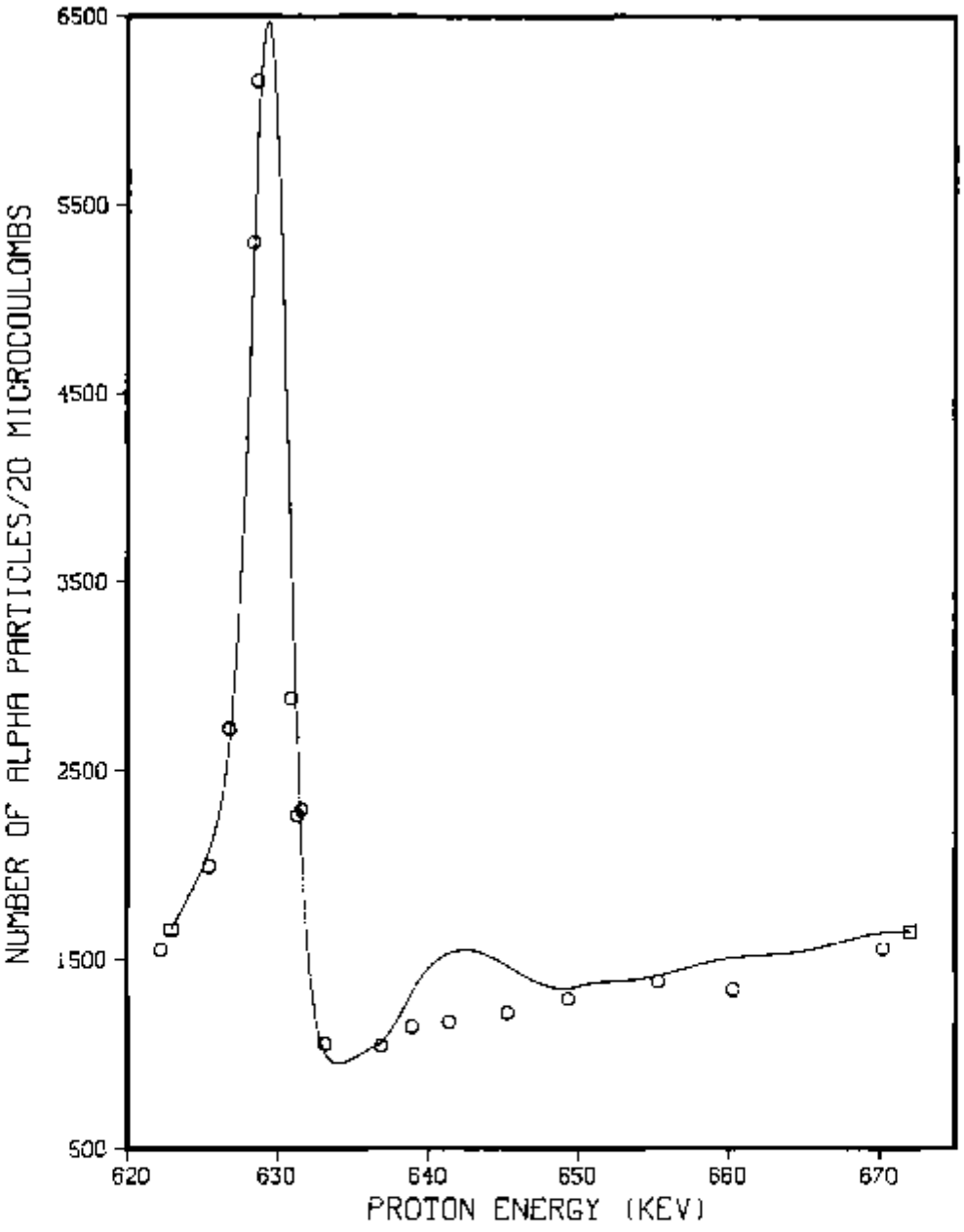

Fig. 29. Calculated excitation curve for the cathode side of a MgO single crystal isotopically exchanged with $^{18}O_2$ at 894°C/48h in the presence of an electric field of 90 V cm^{-1}. Experimental points are included for comparison.

I. P. E. N.

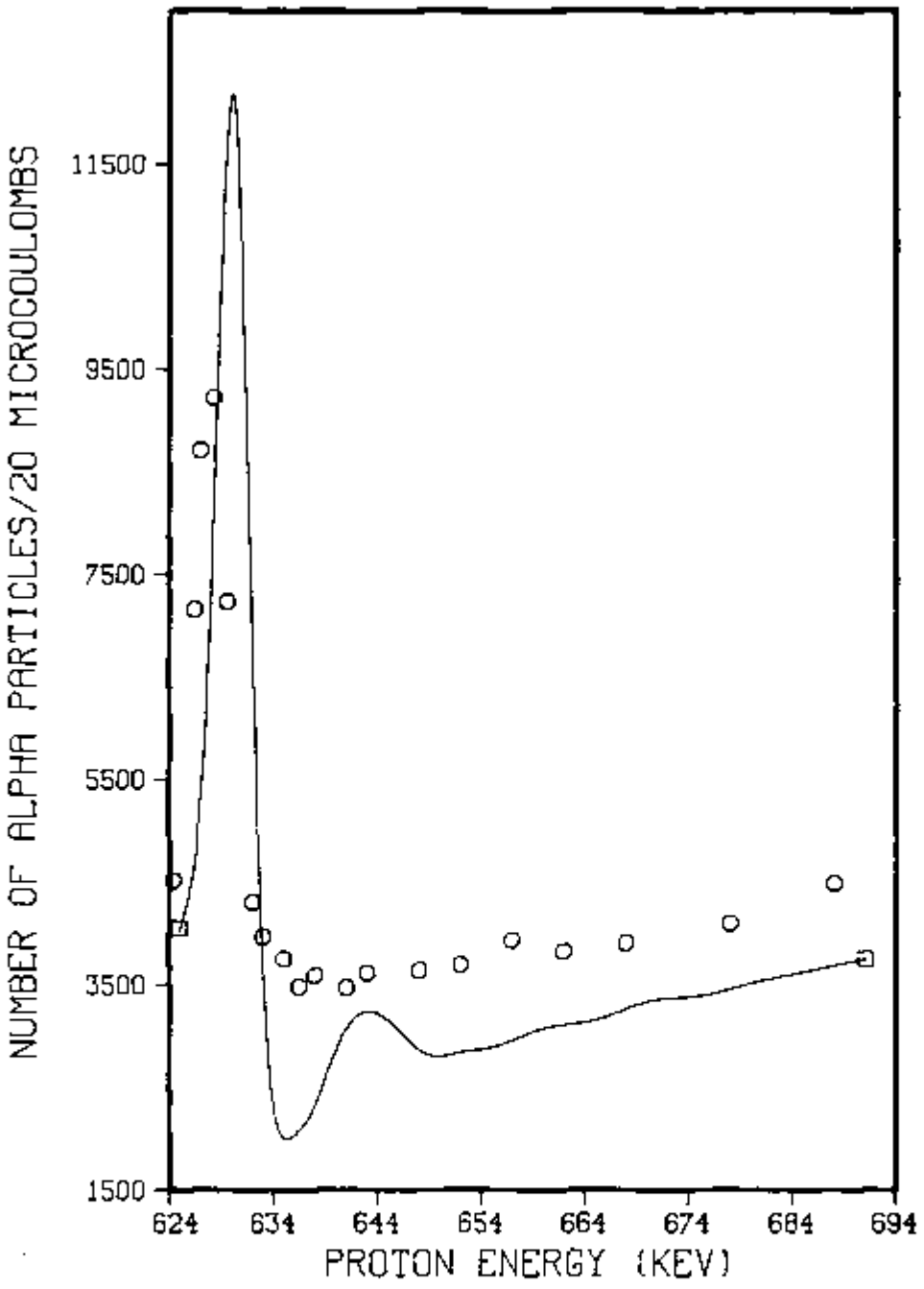

Fig. 30. Calculated excitation curve for the cathode side of a MgO single crystal isotopically exchanged with $^{18}O_2$ at 936°C/48h in the presence of an electric field of 90 V cm^{-1}. Experimental points are included for comparison.

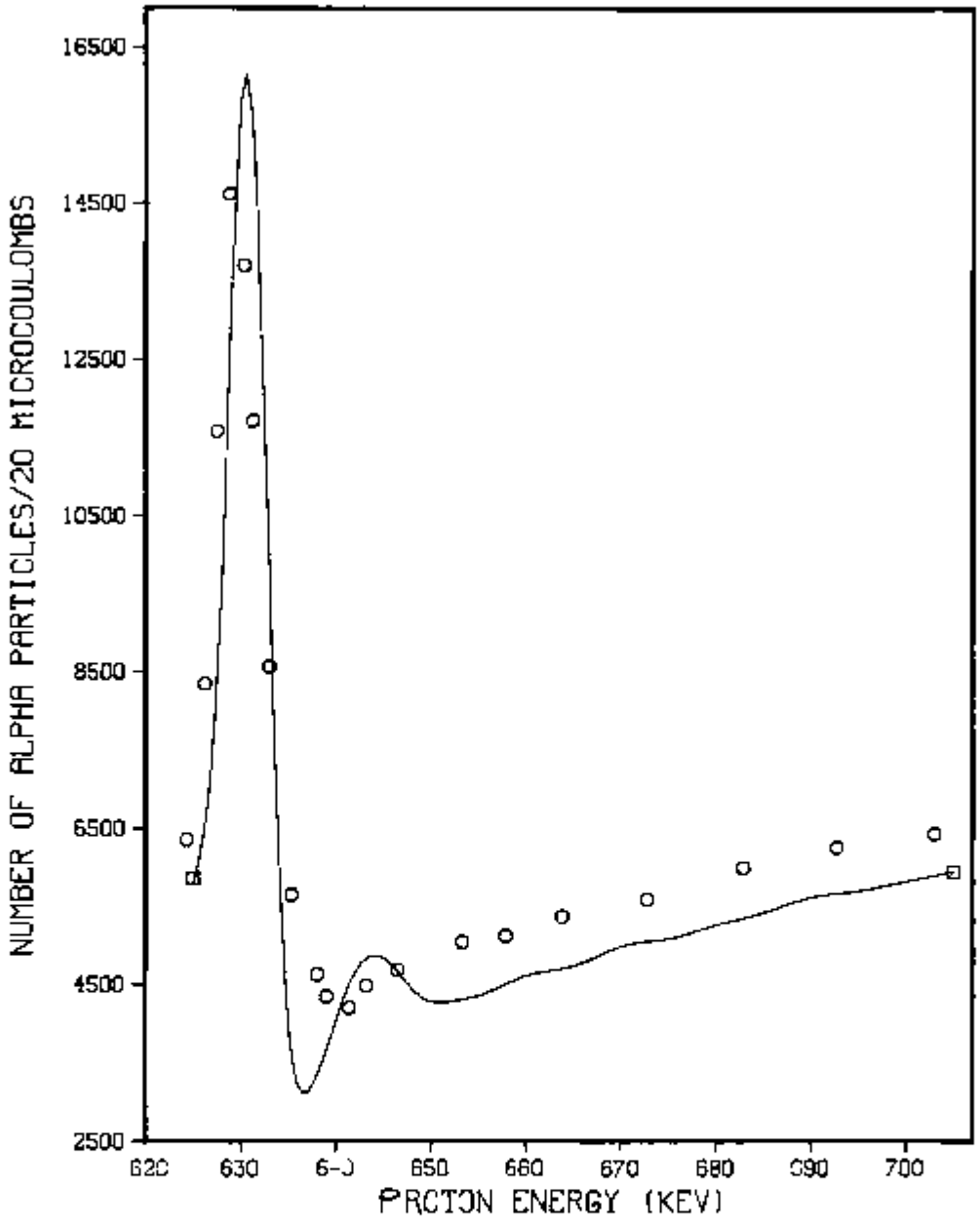

Fig. 31. Calculated excitation curve for the cathode side of a MgO single crystal isotopically exchanged with $^{18}O_2$ at 973°C/48h in the presence of an electric field of 90 V cm^{-1}. Experimental points are included for comparison.

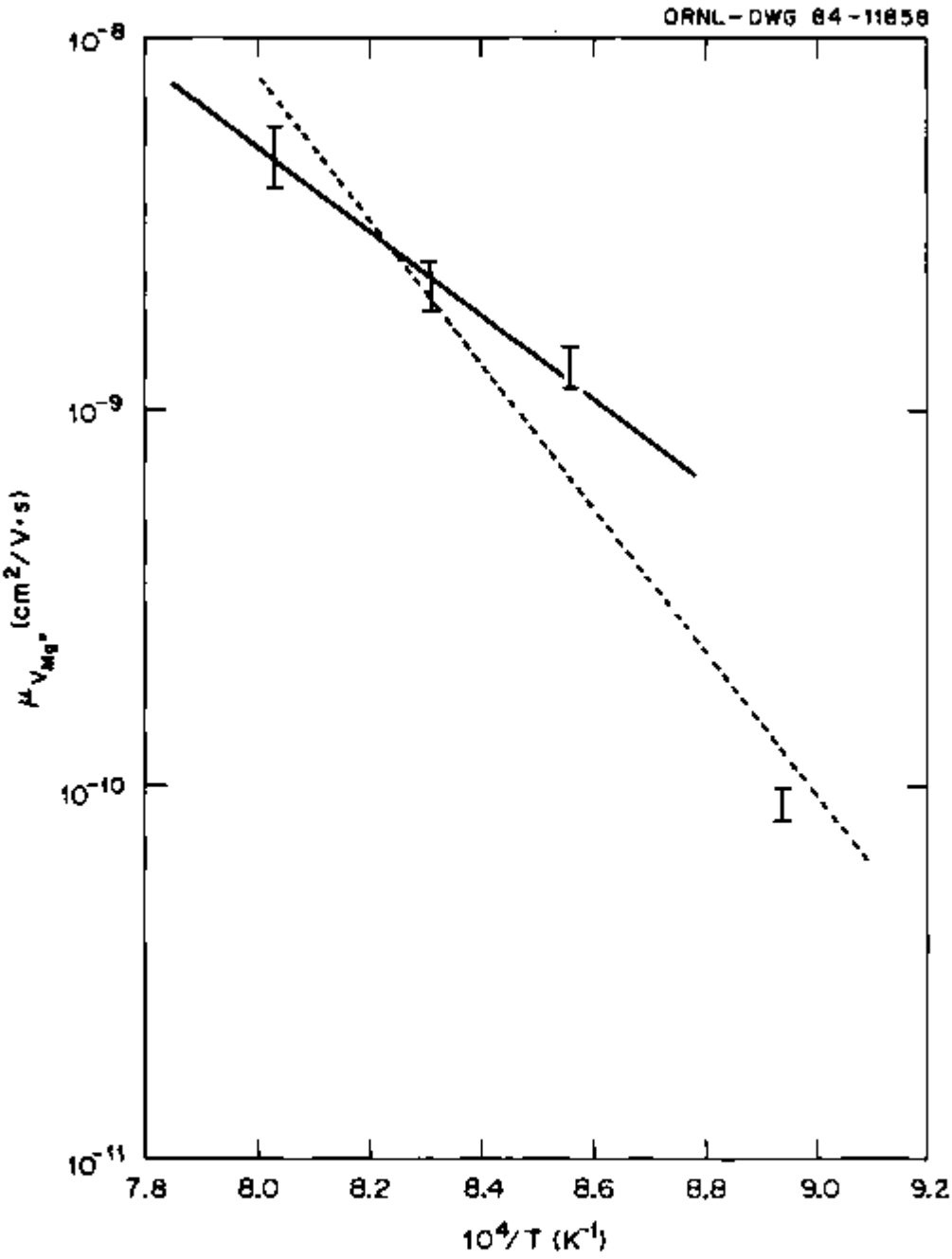

Fig. 32. V_{Mg}'' mobility vs reciprocal temperature. Solid line is the least square fit of the three points at higher temperatures, and dashed line is the least square fit of all points.

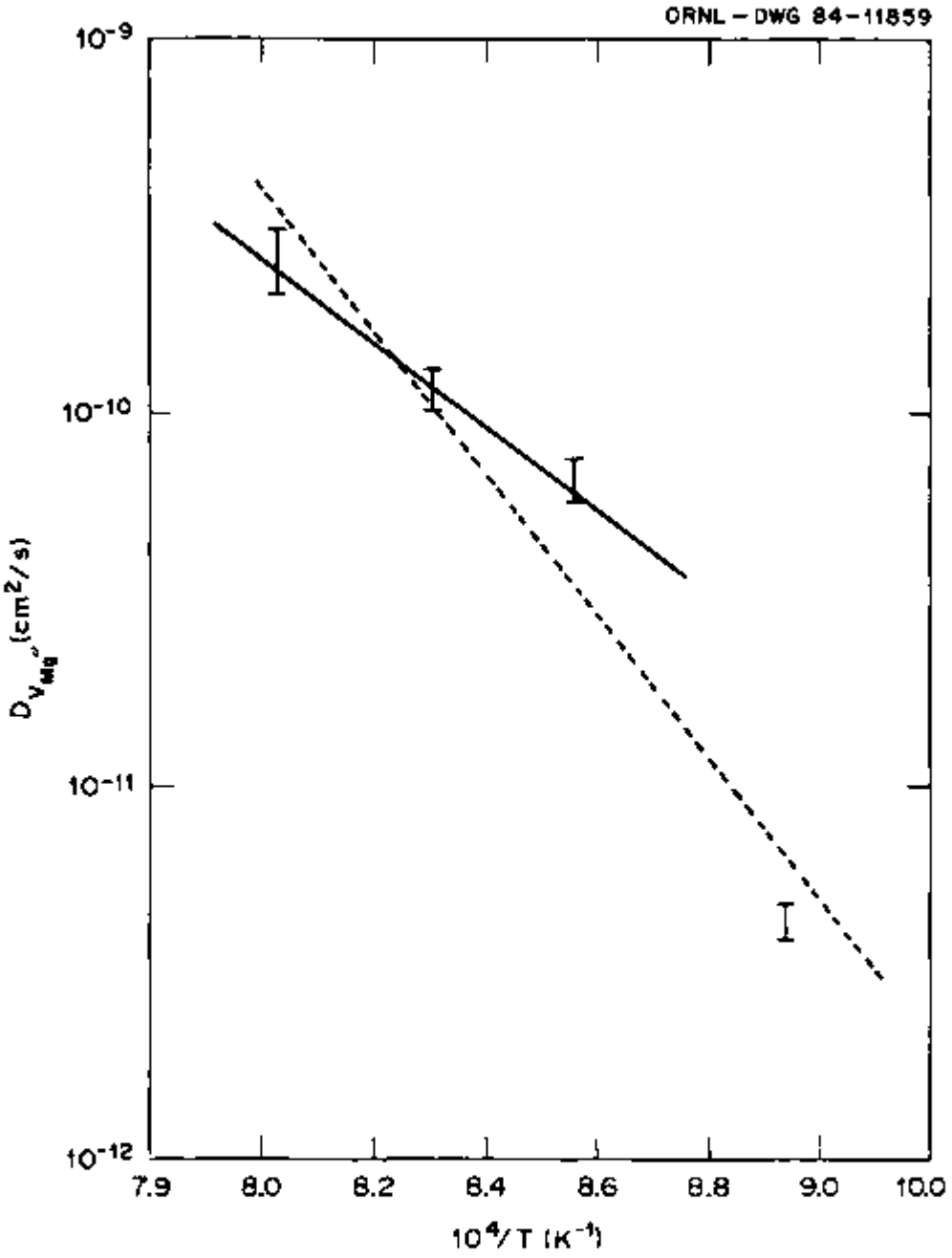

Fig. 33. V_{Mg}'' diffusion coefficient vs reciprocal temperature. Solid line is the least square fit of the three points at higher temperatures and dashed line is the least square fit of all points.

The diffusion coefficient is given by

$$D_{V''_{Mg}}\left(\frac{cm^2}{sec}\right) = (0.3\pm0.3)\exp\left[-\left(\frac{215\pm18}{RT}\right)\ kJ/mole\right] . \qquad (30)$$

If the least-square fit of all points in Figures 32 and 33 to equation 11 is taken (indicated by dashed lines), the activation energy will be higher as given by the following equation:

$$D_{V''_{Mg}}(cm^2/sec) = (9.8\pm5.0)\times10^5\exp\left[-\frac{368\pm69}{RT}\ kJ/mole\right] . \qquad (31)$$

TABLE 4

MAGNESIUM VACANCY MOBILITY AND DIFFUSIVITY IN MgO

Temperature (K)	Time (sec)	ΔX(Å)	μ $cm^2/v.s$	D cm^2/s
1118±3	501480	22±2	$(8.83\pm0.90)\times10^{-11}$	$(4.25\pm0.43)\times10^{-12}$
1168±3	173322	111±14	$(1.31\pm0.17)\times10^{-9}$	$(6.29\pm0.86)\times10^{-11}$
1204±1	86936	92±12	$(2.16\pm0.28)\times10^{-9}$	$(1.12\pm0.15)\times10^{-10}$*
1246±1	173334	409±74	$(4.81\pm0.87)\times10^{-9}$	$(2.58\pm0.47)\times10^{-10}$

*Data from Fig. 35.

The data at T ≥ 1168 are better fitted by equation 30. Both activation energy and pre-exponential values given by this equation are in better agreement with the results reported for Mg diffusion in MgO (see Table 2). The proposed model of Mg ion drift to the cathode by vacancy

mechanism is then confirmed by these results. Furthermore, the activation energy value obtained in this work indicates that the defects are extrinsic as a consequence of the presence of aliovalent impurities.

Equation 31 shows higher activation energy when the lower temperature data is included. This value of mobility at the lowest temperature may be an indication of impurity cluster formation. Further experiments are needed to determine if precipitation of aliovalent ions is the relevant factor. The precipitation process has been observed at 800°C [56] with iron implanted in MgO, forming oxide precipitates and spinel ferrite. It is also known that the solubility of Si in MgO is very low at T< 1200°C [38]. Cr^{3+} has been observed to be reduced by electric fields of 1000 V/cm at 1100°C in MgO [57]. Surface segregation of aluminum by spinel precipitation has been observed in MgO [58,59]. The growth of the spinel precipitates at the surface is observed for T > 800°C but not for lower temperatures, even over a period of several hours.

The vacancy mechanism for atomic diffusion requires a nearest neighbor vacancy. Hence, the jump rate of an ion is proportional to the vacancy concentration. However, the vacancy itself can jump to any of the occupied nearest neighbor positions and therefore their jump rate is independent of the concentration. Thus, the diffusion coefficient for vacancies does not depend on the vacancy concentration for small defect concentrations [46].

The vacancy diffusion coefficient, D_V, is related to the random diffusion coefficient, D_r, by

$$D_r = c\, D_V \quad , \tag{32}$$

where c is the vacancy concentration. Equation (32) is only valid when the diffusion is completely random and the successive jumps are independent, i.e., uncorrelated. In the measurement of the diffusion of tracers, this assumption is not fulfilled since each jump depends on the preceding one. Therefore, the diffusion of the tracer atom is no longer uncorrelated. However, the vacancy can jump to any one of its nearest neighbors, while the tracer atom can only jump to the vacancy site.

The diffusion coefficient for correlated diffusion of a tracer atom in a cubic crystal is given by

$$D^{T}_{Mg} = N_V \, f \, D^{''}_{V_{Mg}} \quad , \tag{33}$$

where f is the correlation factor and N_V the fraction of vacant Mg sites. For vacancy self-diffusion in face-centered cubic crystal, f = 0.78 [46]. N_V is estimated to be 5.45×10^{-5} from the vacancy concentration value calculated by equation 4.

In order to compare the magnesium self-diffusion coefficient obtained in the present work with results previously reported, D_{Mg} is calculated from equation 33. Table 5 shows D_{Mg} as a function of temperature.

Figure 34 shows the magnesium self-diffusion coefficient values obtained in this work as a function of reciprocal of the temperature. Values previously reported are also plotted for comparison. Indeed, the values in the present work are in good agreement with the ones expected by extrapolating the higher temperature values.

In order to substantiate the validity of the model proposed for mass transport under influence of electric field, the time, and field

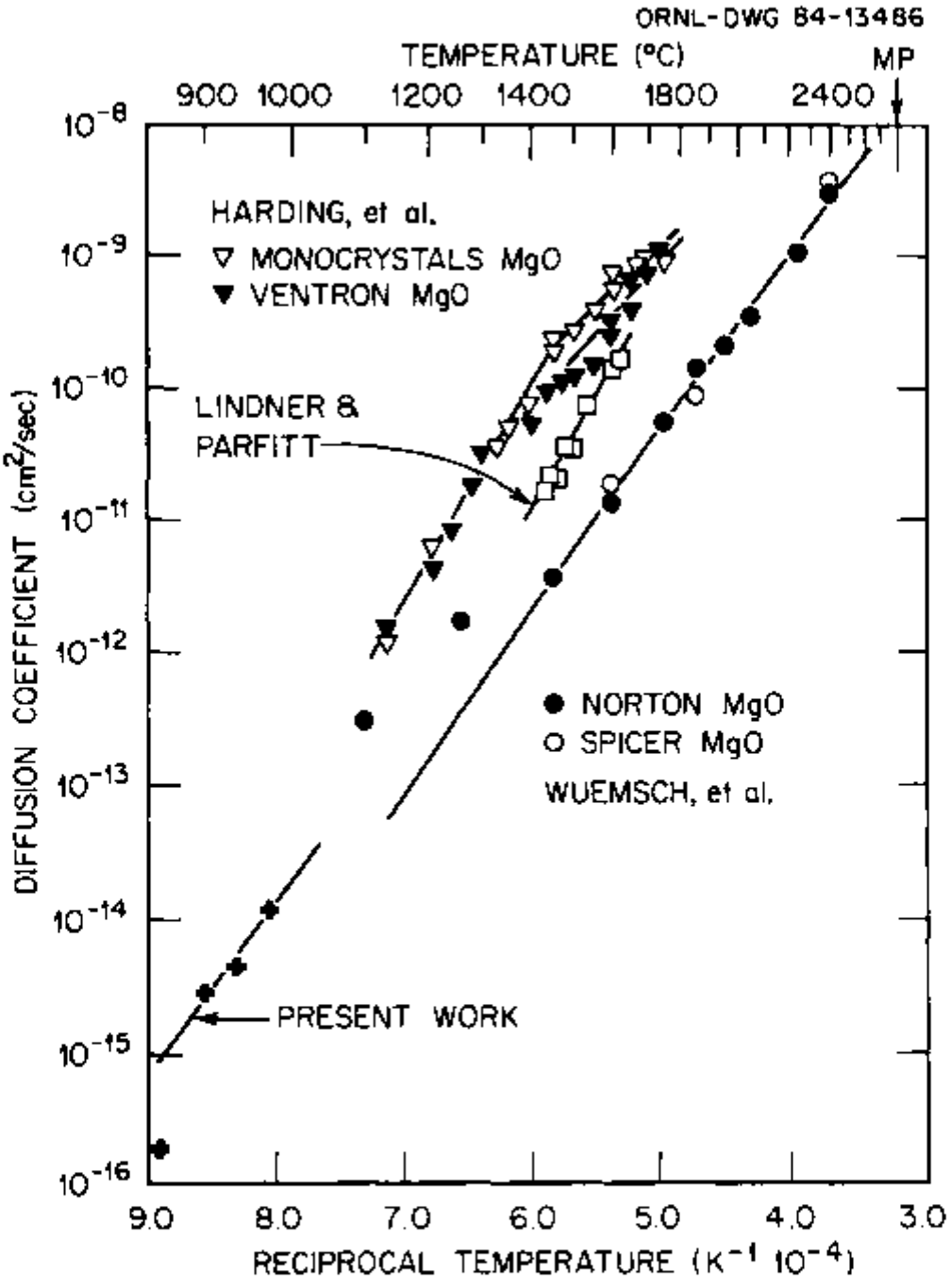

Fig. 34. Comparison of My diffusion data in MgO. Harding et al., Ref. 41; Lindner and Parfitt, Ref. 37; Wuemsch et al., Ref. 39.

TABLE 5

MAGNESIUM SELF-DIFFUSION COEFFICIENT IN MgO

Temperature (K)	D_{Mg} (cm^2/s)
1118±3	$(1.81\pm0.18)\times10^{-16}$
1168±3	$(2.80\pm0.37)\times10^{-15}$
1204±1	$(4.75\pm0.64)\times10^{-15}$
1246±12	$(1.10\pm0.20)\times10^{-14}$

strength dependence were analyzed. By rearranging equation (27)

$$\Delta x = \frac{M \cdot J \cdot \Delta t}{aZF} \quad . \tag{34}$$

Hence, a linear dependence between Δx, the $Mg^{18}O$ film thickness, and Δt, the time interval, is expected. The experimental excitation curves shown in Fig. 13 for the near cathode region are plotted in Figs. 35, 36, and 37 with the curves obtained from the convolution program. Time intervals varied from 24 h to 96 h, while temperature and field strength were kept constant. Figure 38 shows Δx calculated from the curves as a function of time interval Δt and $\sqrt{\Delta t}$. A linear dependence between Δx and Δt is observed, as expected for drift mobility.

Following the same procedure, the dependence between Δx and E, the field strength, was analyzed. By rearranging equation (27) and replacing the current density by equation (17)

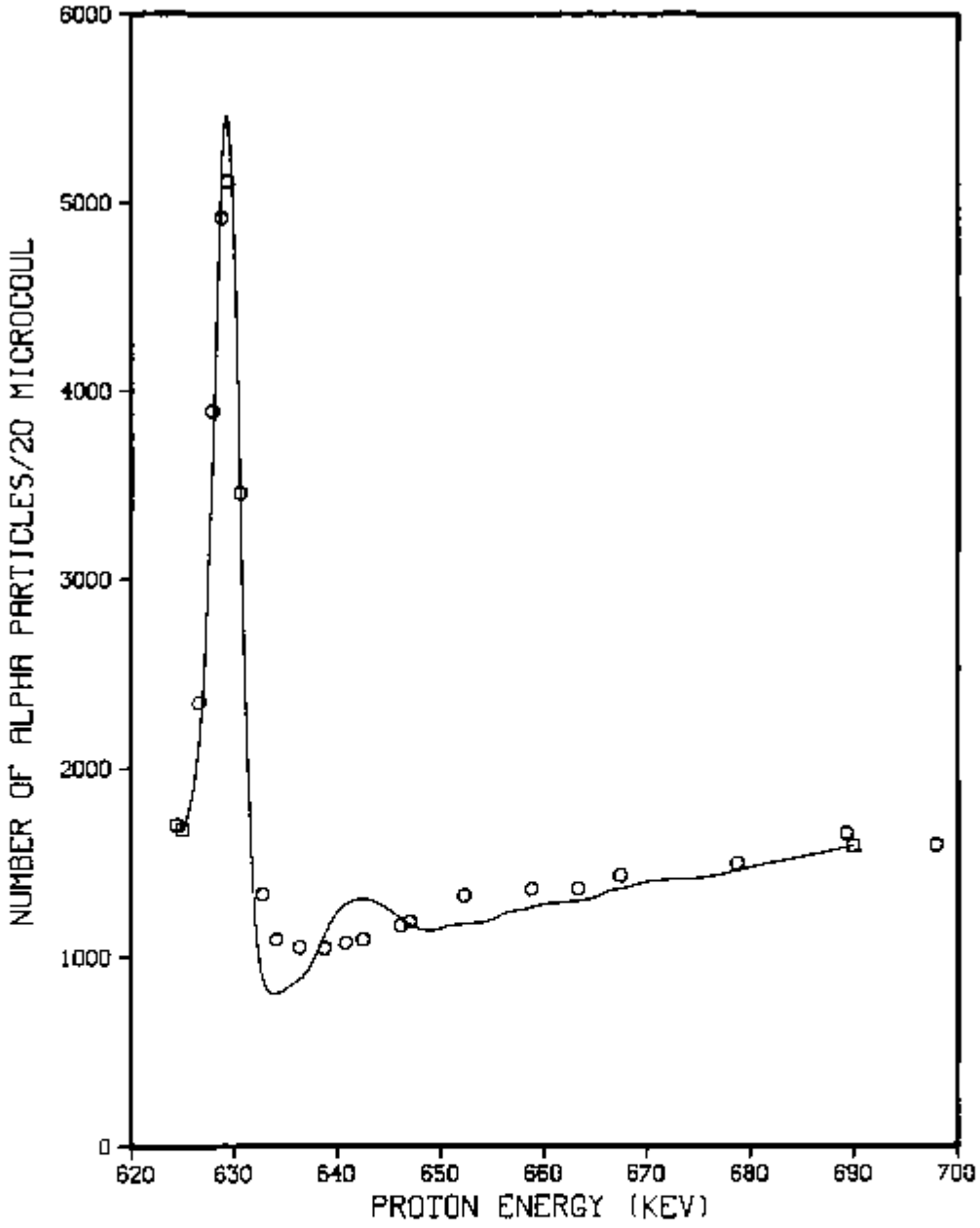

Fig. 35. Calculated excitation curve for the cathode side of a MgO single crystal isotopically exchanged with $^{18}O_2$ at 930°C/24h in the presence of an electric field 90 V cm^{-1}. Experimental points are included for comparison.

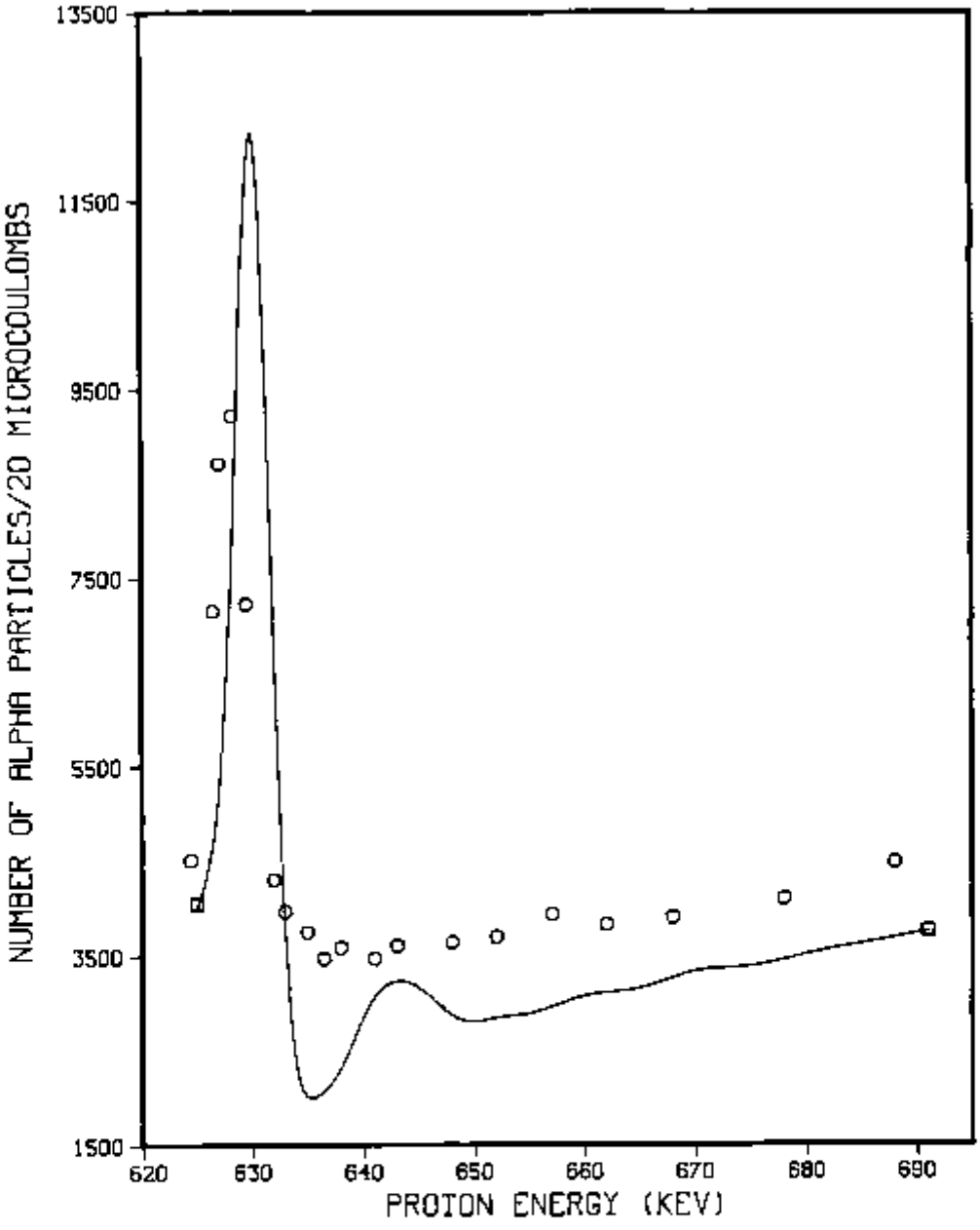

Fig. 36. Calculated excitation curve for the cathode side of a MgO single crystal isotopically exchanged with $^{18}O_2$ at 930°C/48h in the presence of an electric field 90 V cm^{-1}. Experimental points are included for comparison.

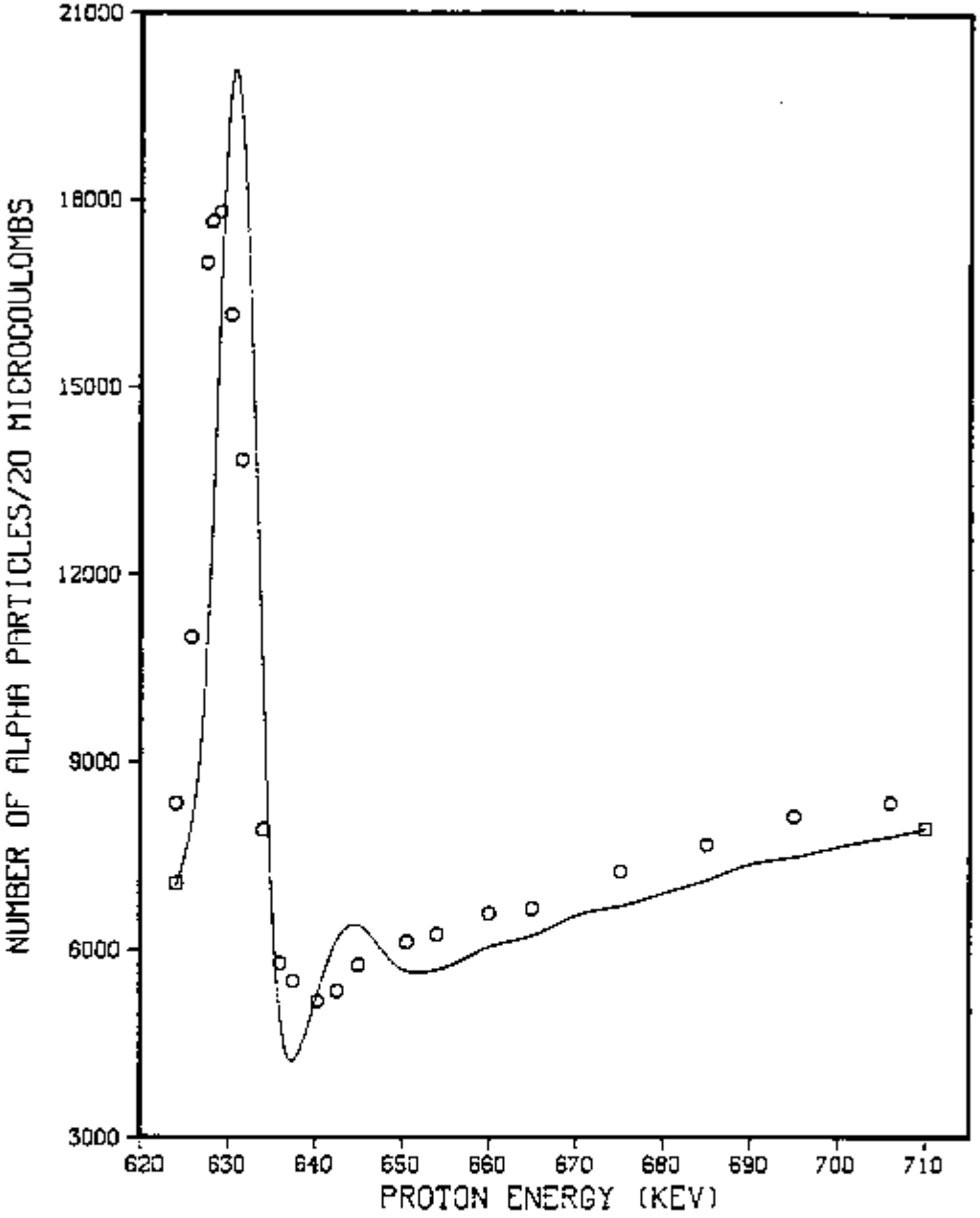

Fig. 37. Calculated excitation curve for the cathode side of a MgO single crystal isotopically exchanged with $^{18}O_2$ at 930°C/96h in the presence of an electric field 90 V cm^{-1}. Experimental points are included for comparison.

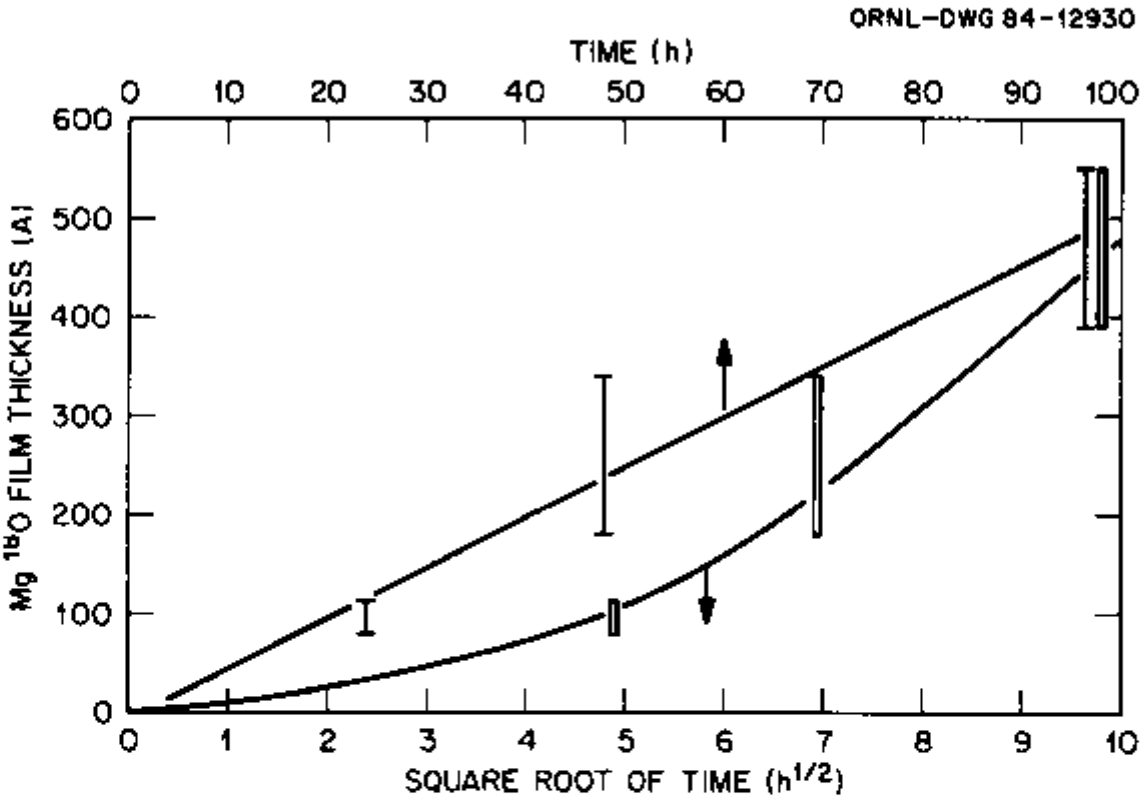

Fig. 38. Growth of $Mg^{18}O$ layer on surface of crystal vs time interval, square root of time interval.

$$\Delta x = \frac{M\sigma\Delta t}{aZF} E \quad . \tag{35}$$

Again a linear relation between Δx, the $Mg^{18}O$ film thickness, and E, the electric field strength is expected, as a characteristic of drift mobility.

From the calculated excitation curves plotted in Figs. 39 through 43, Δx was calculated for field strengths of 10, 90, 300, 1000, and 3000 V/cm, respectively. Figure 44 shows the linear relation between Δx and E.

Hence, the observed variation of the excitation curves with time, temperature, and field strength are consistent with the model proposed for mass transport by magnesium vacancies.

An estimate of the average transference number for any run can be made using equation 25. The results, obtained from the experimental value of the film thickness Δx and current I, during the run, are given in Table 6.

TABLE 6

CATIONIC TRANSFERENCE NUMBER IN MgO

T (K)	$t_{cationic}$
1243±4	0.37±0.12
1206±3	0.48±0.11
1168±3	0.45±0.11

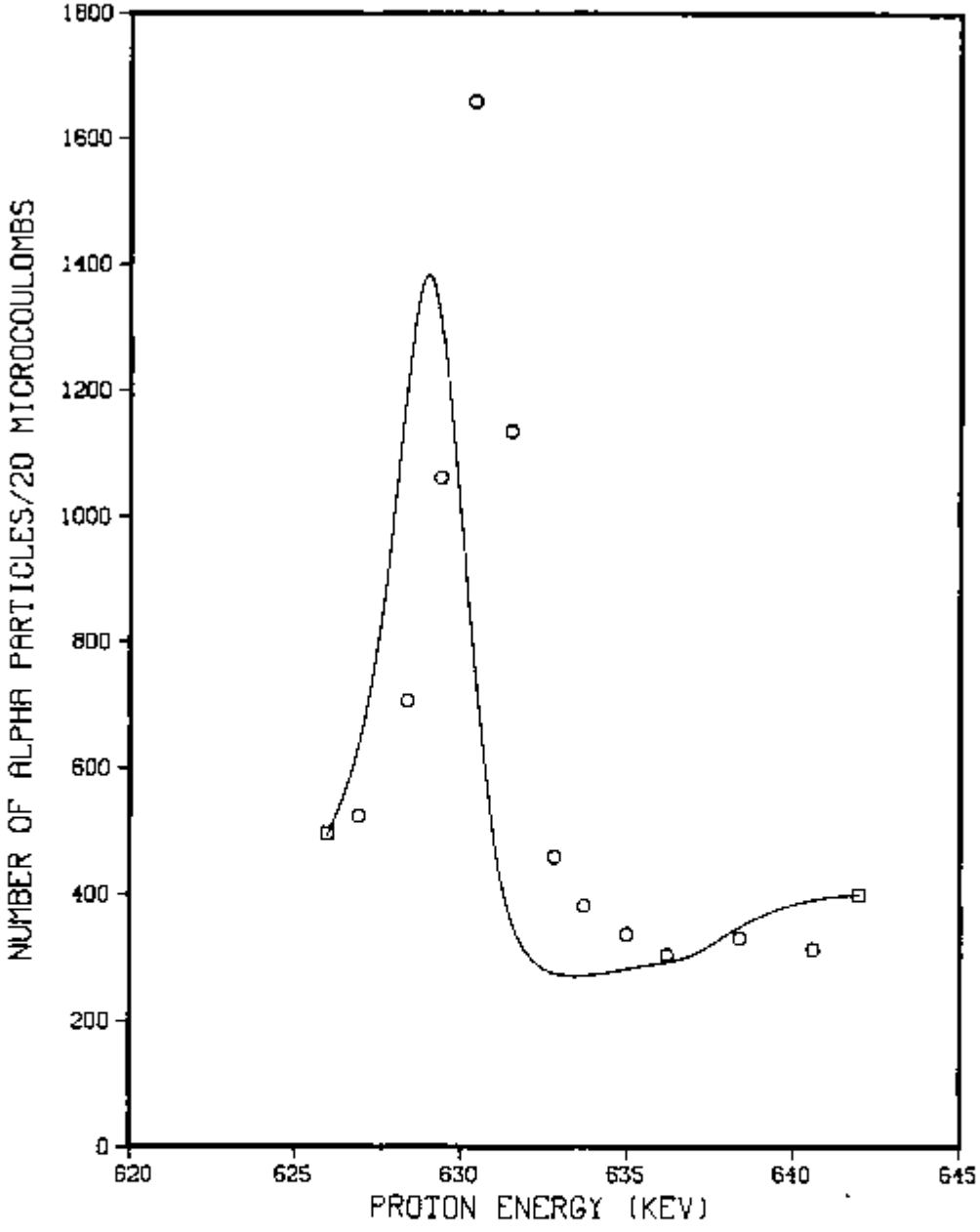

Fig. 39. Calculated excitation curve for the cathode side of a MgO single crystal isotopically exchanged with $^{18}O_2$ at 930°C/24h in the presence of an electric field 10 V cm^{-1}. Experimental points are included for comparison.

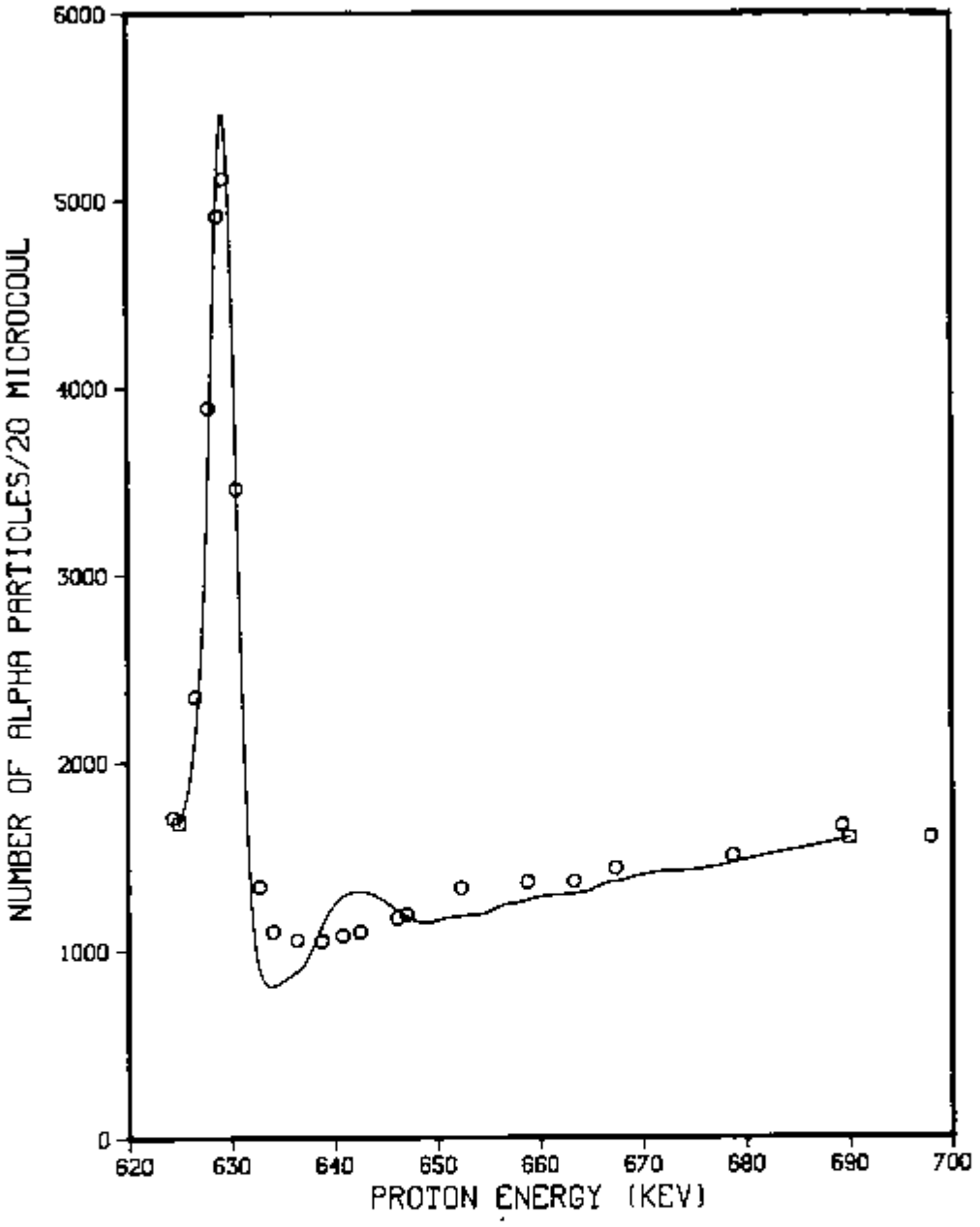

Fig. 40. Calculated excitation curve for the cathode side of a MgO single crystal isotopically exchanged with $^{18}O_2$ at 930°C/24h in the presence of an electric field 90 V cm^{-1}. Experimental points are included for comparison.

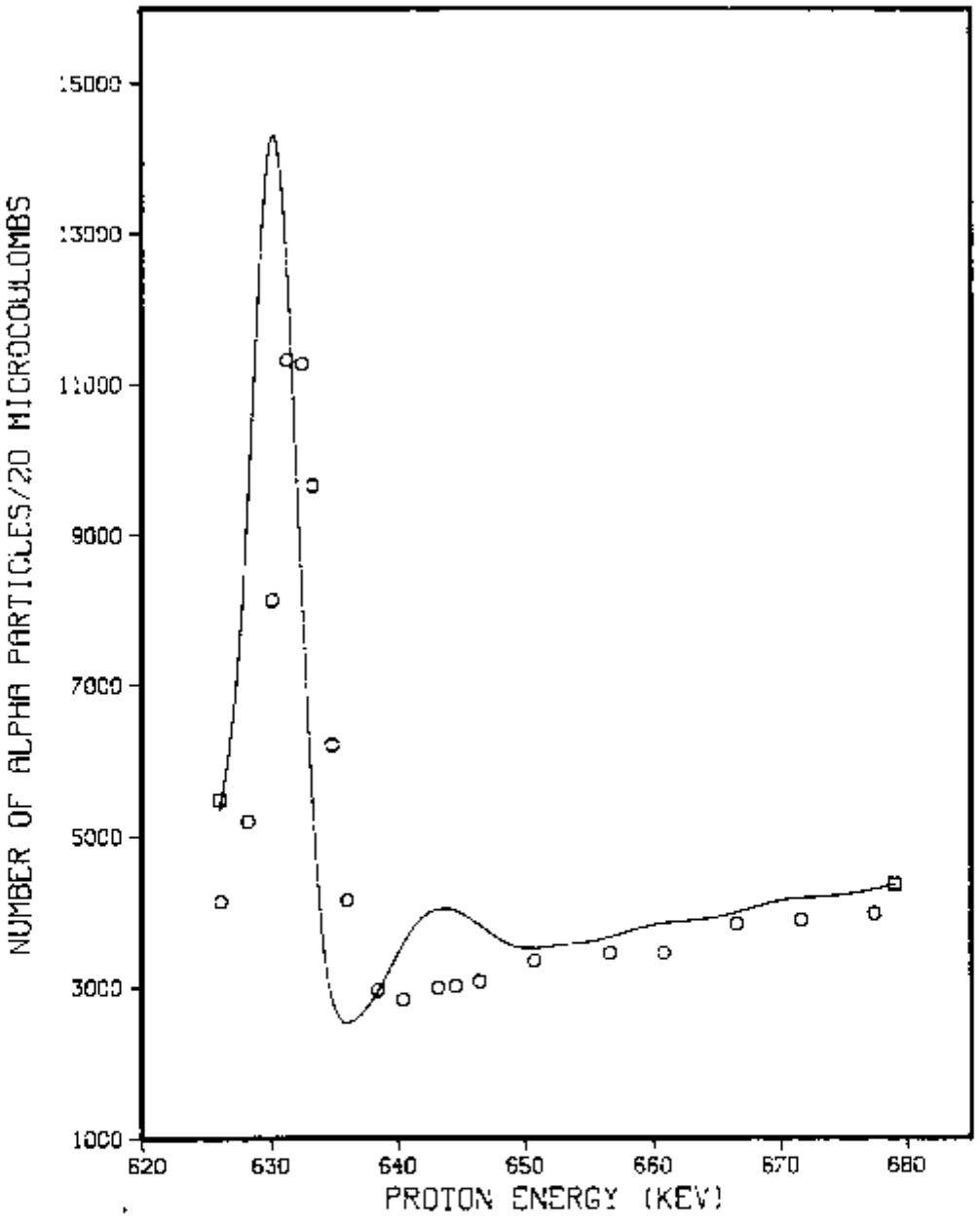

Fig. 41. Calculated excitation curve for the cathode side of a MgO single crystal isotopically exchanged with $^{18}O_2$ at 930°C/24h in the presence of an electric field 300 V cm^{-1}. Experimental points are included for comparison.

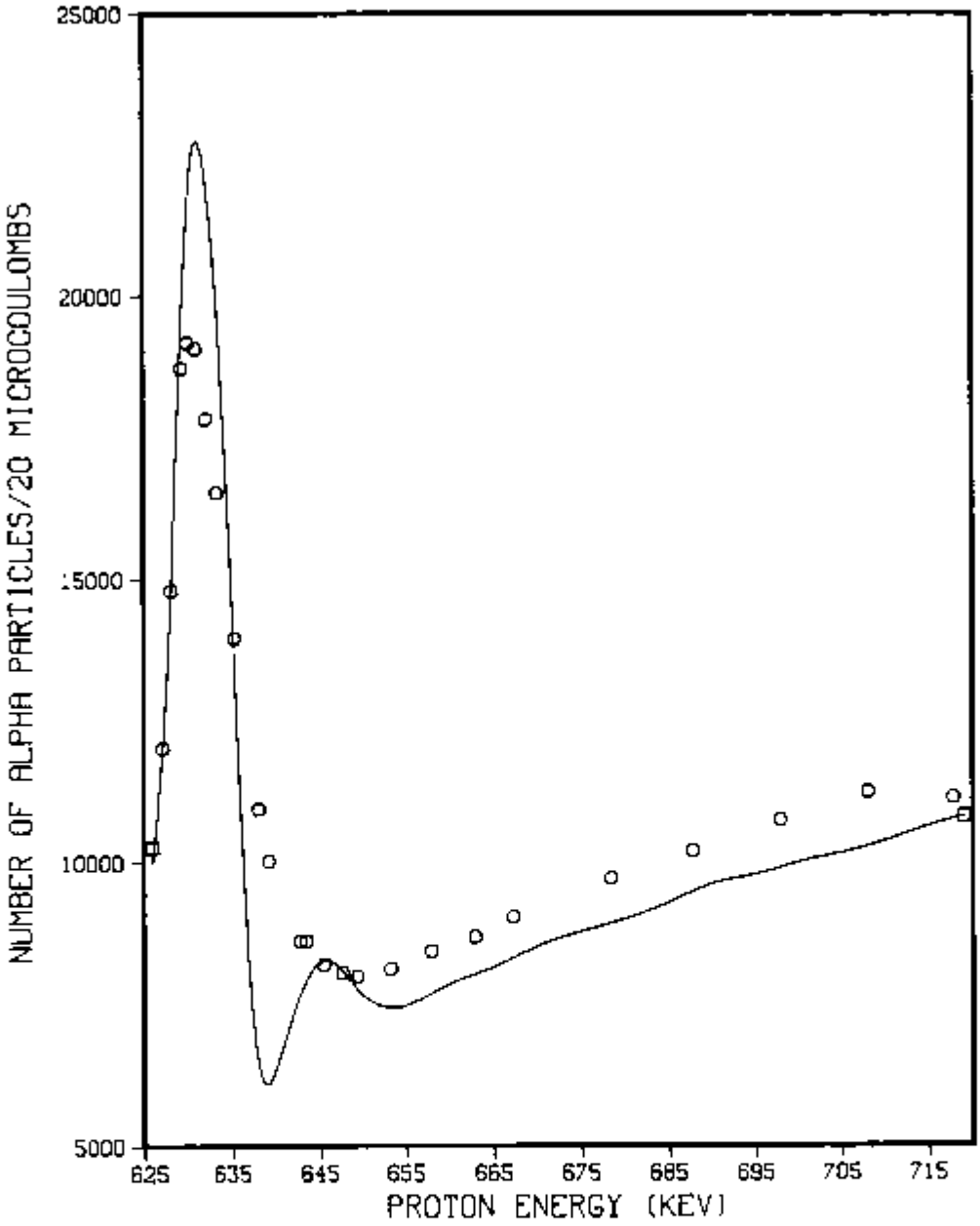

Fig. 42. Calculated excitation curve for the cathode side of a MgO single crystal isotopically exchanged with $^{18}O_2$ at 930°C/24h in the presence of an electric field 1000 V cm^{-1}. Experimental points are included for comparison.

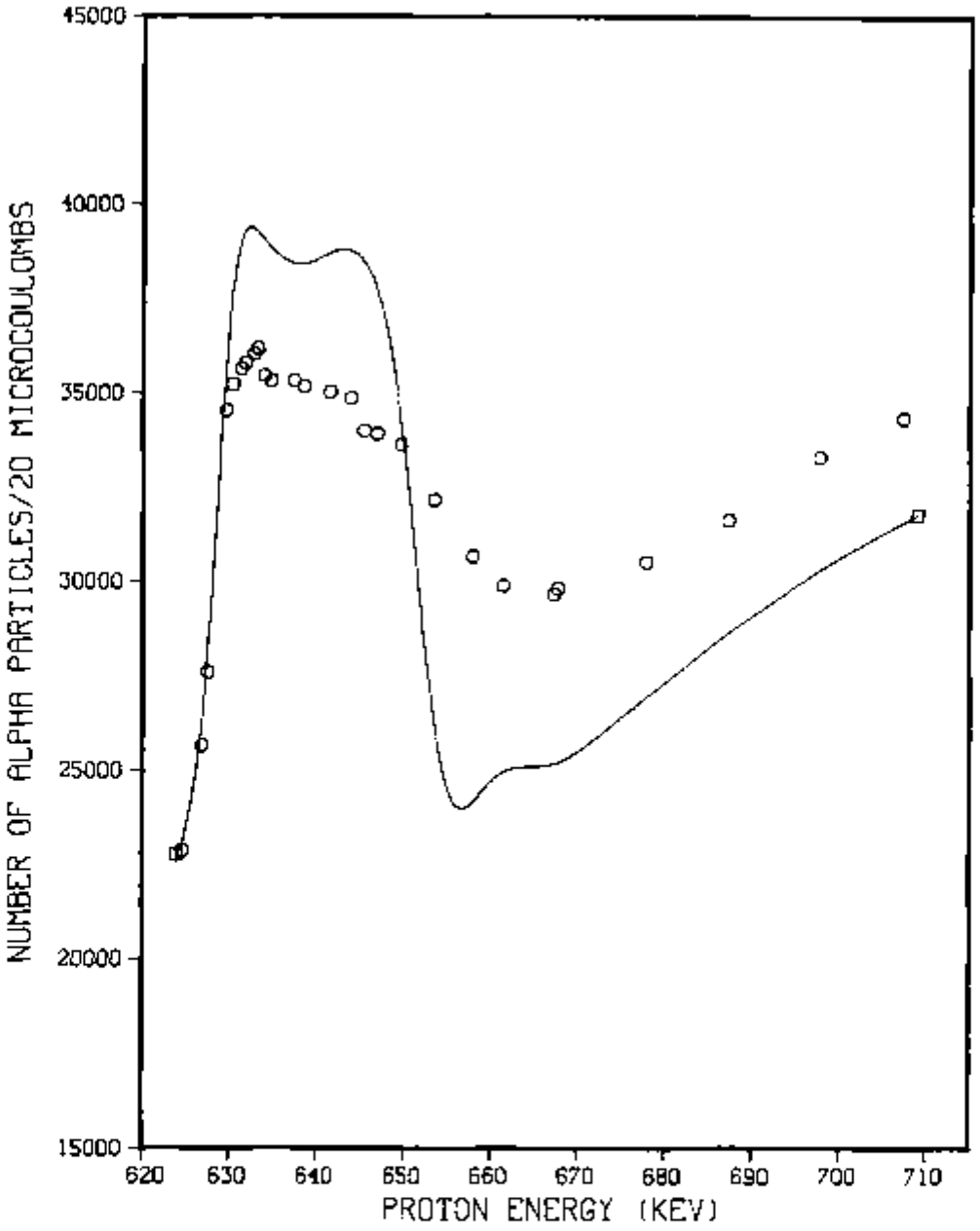

Fig. 43. Calculated excitation curve for the cathode side of a MgO single crystal isotopically exchanged with $^{18}O_2$ at 930°C/24h in the presence of an electric field 3000 V cm^{-1}. Experimental points are included for comparison.

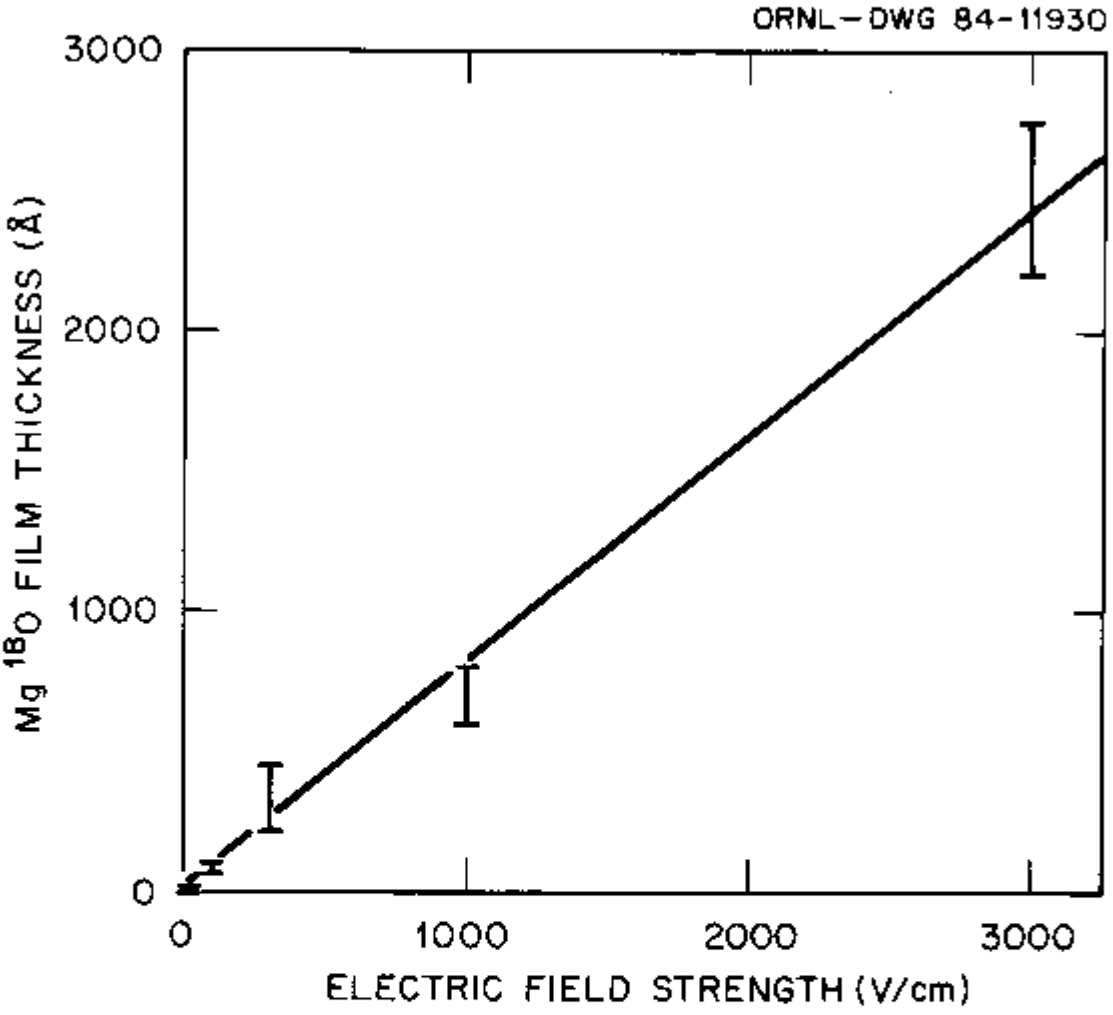

Fig. 44. $Mg^{18}O$ layer growth vs electric field strength.

INSTITUTO DE ENERGÉTICA E NUCLEARES
I. P. E. N.

These numbers are in agreement with the ones reported at 1428 K and 1507 K for MgO equilibrated in 1 atm of oxygen [43]. A relatively large fraction of ionic motion is still observed at 1168 K indicating that ionic transport is correlated to extrinsic defects independent of the temperature.

Results for Cr-Doped MgO

In the preceding section, evidence for magnesium ion drift by a vacancy mechanism was presented. Extrinsic vacancies were assumed to be due to the presence of aliovalent impurities. In this section, an additional experiment is presented to substantiate that assumption.

A MgO sample containing 1500 μg/g chromium was subjected to an electric field of 1000 V/cm during 24 h at 930°C. A sandwich was made of a nominally pure MgO sample and a Cr doped sample in which the anode was placed between the two samples. The cathode of each sample was brought out of the furnace separately. Thus, both samples experienced identical electric field and ^{18}O atmosphere. The observed excitation curves obtained from both the cathode and anode faces of each crystal are shown in Fig. 45.

It is obvious from these data that the concentration of ^{18}O, as well as the depth of the oxide layer, are higher near the cathode region of the Cr-doped MgO than the cathode region of the nominally pure MgO. The anode regions for both samples show lower ^{18}O concentration in agreement with previous results.

The solid lines in Fig. 45 are the calculated excitation curves, following the procedure described in the preceding section. From these

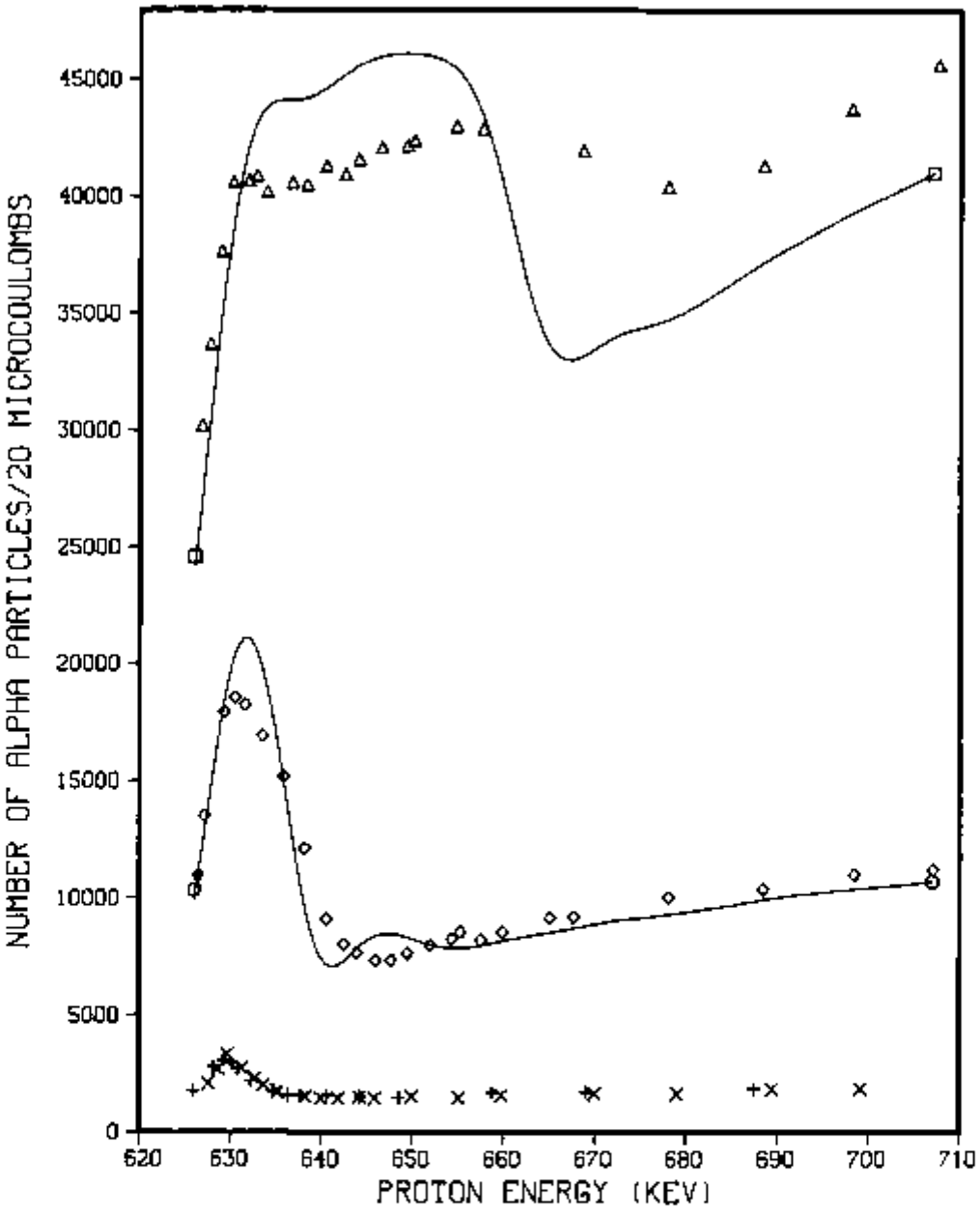

Fig. 45. Calculated excitation curves for the cathode sides of a Cr-doped MgO and a nominally pure MgO single crystal subjected to 1000 V cm^{-1} in an atmosphere of $^{18}O_2$ at 930°C during 24h. Experimental data are included for: (△) cathode side of Cr-doped MgO, (◇) cathode side of nominally pure MgO, (x) anode side of Cr-doped MgO, and (+) anode side of nominally pure MgO.

curves the $Mg^{18}O$ film thickness is determined to be 3540±350 Å for the cathode of Cr-doped MgO, and 851±102 Å for the cathode of nominally pure MgO.

Chromium shows some influence on the electrical conductivity of MgO [60]. EPR measurements show that chromium normally is in the 3+ valence state in untreated MgO, and reduction or oxidation has no major influence on the Cr^{3+} concentration [60]. Therefore, the concentration of V''_{Mg} is calculated from equation 4, knowing the concentration of Cr^{3+}. However from the calculated excitation curve, it is estimated that only 30% of this concentration is taking part in the transport process. This result is in agreement with the decrease of Cr^{3+} concentration detected by EPR measurement of MgO samples subjected to 1000 V/cm at 1100°C [57]. The disappearance or large decrease of absorption lines due to Cr^{3+} indicates that Cr^{3+} is changing its charge state, probably to Cr^{2+}. Moreover, Cr might be present as pairs and triplets which will influence their participation in the ionic transport process.

The cationic transference number was calculated from equation (25). For Cr-doped MgO t_{cat} = 0.80±0.15, which is higher than the one calculated for the nominally pure MgO (t_{cat}=0.54±0.10). This indicates that the additional chromium is increasing the ionic transport by increasing the extrinsic vacancy concentration.

Finally, a simple calculation of evaporation rate [61] shows that the fraction of material lost by free evaporation at 930°C during the time intervals of the present work is negligible and should not influence the results. For instance, at 930°C the loss of material in vacuo would be 1.60×10^{-12} g/cm^2 s. For a period of 24 h, material to

a depth up to 4 A is lost. This depth is far less than either oxygen diffusion penetration or buildup of $Mg^{18}O$ layers on the surface, e.g., for an electric field of 1000 V/cm a film thickness of 700 A, which is at least two orders of magnitude higher, has been determined for the same period of time.

RBS Analysis

The RBS spectra depicted on Figs. 17 and 18 show that for samples annealed in an electric field $^{18}O_2$ can be detected. Moreover, a depth penetration on the order of 1000 A and a ^{18}O isotope concentration of $5x10^{16}$ cm^{-2} are estimated. These numbers are in good agreement with the ones obtained by the convolution program applied to the excitation curves of the $^{18}O(p,\alpha)^{15}N$ nuclear reaction. In fact, the RBS spectrum depicted in Fig. 18 is very impressive since ^{18}O can be resolved from ^{16}O. According to L'Hoir et al. [52], the ^{18}O concentration profile on oxides or silicates "has no effect" on RBS spectra near random positions. Our results show that in the particular case of a sample subjected to an electric field, the ^{18}O peak is observed in RBS spectra. Hence, these results confirm that $Mg^{18}O$ film is present on the surface of the cathode. From the RBS spectra in the channeling mode (Fig. 19 and 20), surface peaks for ^{16}O and ^{18}O are observed for both crystals (without, and with field). This result is expected since a fraction of ^{16}O of the crystal surface is exchanged with ^{18}O in the gas phase in both crystals. However, there is no indication whatsoever of ^{18}O in interstitial positions or distortion of the crystalline structure in MgO subjected to electric field. The α-particles are very well channeled

and the scattering surface peaks are well resoluted in the RBS spectra in the channeling mode.

SEM Analysis

A significant alteration of the surfaces in contact with the electrodes is detected when fields > 1000 V/cm are applied. Figures 21 and 22 show SEM micrographs taken from the surfaces kept in contact with the cathode and the anode during the diffusion annealing with an applied field of 1010 V/cm. The micrographs were taken by tilting the surface 45° from the normal with respect to the electron beam. At lower magnification (70X) spots created by the contact between the crystal surface and the platinum gauze are observed. The same type of distribution is observed on both surfaces (cathode surface, Fig. 21(b); anode surface, Fig. 22(b). For fields of 300 V/cm, none of these alterations are observed with SEM, however, visual observation of the surface with optical microscope shows that alteration of color and reflectivity has occurred at points of contact. As the field strength is lowered, it is more difficult to observe these effects.

Through the present work a position and time independent electric field was assumed. It should be pointed out that this assumption is only an approximation to the actual experimental condition. Potential profiles along the thickness of MgO crystals have been measured [62] during the application of an electric field (strength of 1000 V/cm at 1473 K). Several profiles have been reported, depending on the level of dc current that crosses the sample. The potential is nonlinear and asymmetric with respect to the center of the sample immediately after

the voltage application. However, the potential varies with time, and eventually a linear dependence on distance is reached. The electric field strength, which initially was much higher in the region near the electrodes, becomes constant.

The platinum gauze used as electrodes will cause a surface field distribution with relatively higher strength in the contact region. It is this higher field strength which causes the contact point configuration observed in the SEM micrographs. In the case of lower field strengths, these higher field spots were not sufficient to produce any detectable alteration on the surface. However, the excitation curves from the nuclear reaction should not be affected because the analysis is averaged amongst the contact points and the surrounding area. The proton beam used for the nuclear reaction has a diameter of 2 mm normal to the beam direction. Therefore, the area covered by the beam encompasses several points of contact between the sample and the platinum gauze. The α-particle count is an average of two regions: the contact points and the surrounding area on the surface. But it has been estimated by the SEM micrographs that the contact points are approximately 5% of the total area encompassed by the proton beam. Therefore, the effects of the spot areas on the measurement is small. Indeed, different surface regions were analyzed by displacing the proton beam on the surface of samples, without showing any substantial difference among the excitation curves. No difference was observed, even when platinum gauzes of different mesh size (45 and 100 mesh) were used.

The experimental excitation curves obtained from the anode surfaces (Fig. 12) of samples subjected to electric field and simultaneously to

$^{18}O_2$ gas/solid isotope exchange, fall into the range expected for oxygen diffusion in MgO but they exhibit some differences among themselves. The reason for these differences are not yet understood. Similar discrepancies have been observed by Gauthier et al. [43] in dilacoulometry experiments.

CHAPTER VI

CONCLUSIONS

i) The use of implantation methods for introducing tracers in diffusion studies is not feasible for ^{18}O in MgO; a systematic study of the effect of implantation damage on the diffusion processes is first necessary. The loss of the implanted ^{18}O during the diffusion anneal indicates a much higher diffusivity toward the surface than that expected for bulk oxygen diffusion.

ii) Gas/solid isotopic exchange has been used to introduce the tracer ^{18}O in MgO. The oxygen self-diffusion coefficients obtained from these analysis are in good agreement with data reported by using $^{18}O_2$ gas/solid isotopic exchange and mass spectrometer analysis.

iii) The oxygen stable isotope can also be used in determining the cationic diffusion coefficient if an external electric field is applied simultaneously to the gas/solid isotopic exchange. The magnesium self-diffusion coefficient was determined by this technique in the range of temperatures 800-1000°C. These results are in good agreement with the extrapolated higher temperature data. The activation energy and the pre-exponential values inferred from these data indicate that diffusion is by a vacancy mechanism.

iv) Cationic transference numbers were determined by measuring the integrated current that flowed through the samples during the anneals.

v) The measured ^{18}O concentration in the cathode region is always higher than in the anode region. The higher ^{18}O concentration is attributed to the oxidation of Mg ions at the cathode. Mg ions are drifted toward the cathode as a consequence of V''_{Mg} drift toward the anode due to the electric field. Extrinsic V''_{Mg} are due to aliovalent impurities replacing Mg ions in the crystal lattice.

vi) MgO containing 1500 μg/g chromium shows higher ^{18}O concentration in the cathode surface than nominally pure MgO. This result supports the assumption that V''_{Mg} are present due to trivalent impurities. However, the vacancy concentration involved in the transport process calculated from the thickness of the $Mg^{18}O$ layer is about 30% of the value expected from the chromium concentration. This result is expected if a transition $Cr^{3+} \rightarrow Cr^{2+}$ occurs due to the electric field or if some of the Cr precipitates.

vii) The present results confirm the migration of negatively charged ionic species (V''_{Mg}) toward the anode electrode as assumed in discussions of electric degradation of MgO.

CHAPTER VII

SUGGESTIONS FOR FUTURE WORK

Weeks et al. [20] showed that electric current flowing through MgO samples due to electric fields in the order of 1000 V/cm increases with time, leading to dielectric breakdown after 100 h at 1200°C. Since there is a controversy concerning the relative importance of electronic and ionic conduction in the degradation mechanism, the present technique could be applied to determine the cation transference number as degradation progresses. The sample would initially be equilibrated in $^{16}O_2$ atmosphere, and after reaching a selected current level, $^{16}O_2$ would be replaced by $^{18}O_2$. The nuclear reaction technique could be used to analyze the ^{18}O concentration on the cathode region. By knowing the current value, the cationic transference number can be determined. Since it has been reported [62] that the addition of impurities such as Cr, V, Fe, and Ni accelerates the degradation, a comparative study of the transference number on MgO doped with those impurities could be done by using the present technique. In fact, data for Cr-doped MgO show an increase in the cationic transference number compared with nominally pure MgO. Ni-doped MgO might be a particularly interesting system, since Ni is the only specie among impurities observed to speed up the degradation that cannot be found in the trivalent state.

The technique developed for MgO and described in this work yields a large amount of transport information. It would be useful to determine

cationic transference number and to identify the contribution of different vacancy types in the transport processes for other insulating oxides such as $MgAl_2O_4$ spinel, YAG, and Al_2O_3.

The loss of implanted ^{18}O after annealing is not yet understood. RBS in both random and channeling modes can provide a surface characterization of MgO implanted with ^{18}O and lead to better interpretation of this effect. Possible amorphization of the implanted region and recrystallization after annealing can be detected by this technique, since channeling is very pronounced in undamaged MgO crystals.

LIST OF REFERENCES

1. Freer, R. "Self-diffusion and impurity diffusion in oxides." J. Mat. Sci. 15(4) 803-24 (1980).

2. Wöhlbier, F. H., ed. Diffusion and Defect Data, Vol. 20 (1979)

3. Oishi, Y., Ando, K., Suya, N., and Kingery, W. D. "Effect of surface condition on oxygen self-diffusion coefficients for single crystal Al_2O_3." J. Am. Ceram. Soc. 66(8), C-130 (1983).

4. Cox, B., and Pemsler, J. P., "Diffusion of oxygen in growing zirconia films." J. Nucl. Mater. 28, 73-8 (1968).

5. Henriksen, A. F., Chiang, Y., and Kingery, W. D. "Enhanced oxygen diffusion at 1400°C in deformed single-crystal magnesium oxide." J. Am. Ceram. Soc. 66(8), C144-6 (1983).

6. Condit, R.H., and Holt, J. B., "A technique for studying oxygen diffusion and locating oxide inclusions in metal by using the proton radioactivation of oxygen-18." J. Electrochem. Soc. 111(10), 1192-4 (1964).

7. McKenzie, D. R., Searcy, A. W., Holt, J. B., and Condit, R. H. "Oxygen grain-boundary diffusion in MgO." J. Am. Ceram. Soc. 54, 188 (1971).

8. Calvert, J. M., Lees, D. G., Derry, D. J., and Barnes, D. "Analysis by charged particle nuclear reaction. The use of charged particle bombardment for studying oxygen self-diffusion in oxides." J. Radioanal. Chem. 12, 271-5 (1972).

9. Robin, R., Cooper, A. R., and Heur, A. H. "Application of a non-destructive single-spectrum proton activation technique to study oxygen diffusion in zinc oxide." J. Appl. Phys. 44(8), 3770 (1973).

10. Amsel, G., Nadai, J. P., D'Artemare, E., David, D., Girard, E., and Moulin, J. "Microanalysis by the direct observation of nuclear reactions using a 2 MeV Van der Graaff." Nucl. Instrum. Meth. 92, 481-93 (1971).

11. Gass, J. E., Müller, H. H., Schmied, H., Jörissen, L., and Ziffermayer, G. "Measurement of oxygen-diffusion-profiles in silicon-single-crystals by means of the nuclear reaction $^{18}O(p,\alpha)^{15}N$." Nucl. Instrum. Meth. 106, 109-13 (1973).

12. Lindstron, W. W. and Heuer, A. N. "A magnetic spectrometer for nuclear microanalysis of concentration distributions." Nucl. Instrum. Meth. 116, 145-55 (1974).

13. Nelson, V. C., and Friauf, R. J. "Diffusion of vacancies and vacancy pairs in NaCl." J. Phys. Chem. Solids 31(4), 825-43 (1970).

14. Geguzin, Ya. E., Solunskii, V. I., and Boiko, Yu. I. "Interdiffusion in KCl-KBr single crystals in an external dc electric field." Sov. Phys.-Solid State 8(4), 1046-7 (1966).

15. MacKenzie, K. J. D., Banerjee, R. K., Kasaai, M. R. "Effect of electric fields on solid-state reactions between oxides. I. Reaction between calcium and aluminum oxides." J. Mater. Sci. 14(2), 333-8 (1979).

16. MacKenzie, K. J. D., and Banerjee, R. K. "Effect of electric fields on solid-state reactions between oxides. Part 2. Interdiffusion studies in polycrystalline calcium and aluminum oxide pellets." ibid. pp. 339-44.

17. MacKenzie, K. J. D., and Ryan, M. J. "Effect of electric fields on solid-state reactions between oxides. Part 3. Interdiffusion in polycrystalline magnesium and aluminum oxide pellets." J. Mater. Sci. 16, 579-88 (1981).

18. Dornelas, W., and Lacombe, P. "Diffusion sous champ électrique de l'oxygéne aux températures de 900° á 1000°C dans l'oxyde d'uranium UO_2." J. Nucl. Mater. 21, 100-4 (1967).

19. Gonzalez, R., Chen, Y., and Tsang, K. L. "Diffusion of deuterium and hydrogen in doped and undoped MgO crystals." Phys. Rev. B 26 (8), 4637-45 (1982).

20. Weeks, R. A., Narayan, J., and Sonder, E. "Electric breakdown in MgO crystals at elevated temperature." Phys. Stat. Sol. (a) 70, 639-9 (1981).

21. Sonder, E., Kelton, K. F., Pigg, J. C., and Weeks, R. A. "The effect of electric current on the conductivity of MgO single crystals at temperatures above 1300 K." J. Appl. Phys. 49, 5971 (1978).

22. Sonder, E., and Weeks, R. A. "Behavior of electric conduction of spinel and other insulating oxides in moderate electric fields at high temperature." To be published in the Journal of Applied Physics.

23. Tsang, K. L., Chen, Y., and O'Dwyer, J. J. "High field conduction and dielectric breakdown in nominally pure and nickel-doped MgO crystals at high temperatures." Phys. Rev. B 26 (12), 6909-17 (1982).

24. Derry, D. J., Lees, D. G., and Calvert, J. M. "A study of oxygen self-diffusion in the c-direction of rutile using a nuclear technique." J. Phys. Chem. Solids 42 (1), 57-64 (1980).

25. Ziegler, J. F. ed. Handbook of Stopping Cross Sections for Energetic Ions in All Elements, Vol. 5 of the Stopping Ranges of Ions in Matter, New York: Pergamon Press, 1980.

26. Williamson, C. F., Boujot, J. P., and Picard, J. "Tables of range and stopping power of chemical elements for charged particles of energy 0.5 to 500 MeV." Rept. CEA-R-3042, Commissariat a l'Energy Atomique, Saclay (France), 1966.

27. Rawal, B. S., and Cooper, A. R. "Oxygen self-diffusion in a potassium strontium silicate glass using proton activation analysis." J. Mat. Sci. 14, 1425-32 (1979).

28. Neild, D. J., Wise, P. J., and Barnes, D. G. "Measurement of ^{18}O concentration profiles using resonant nuclear reactions." J. Phys. D: Appl. Phys. 5, 2292 (1972).

29. Oishi, Y., and Kingery, W. D. "Oxygen diffusion in Periclase crystals." J. Chem. Phys. 33 (3), 905 (1960).

30. Reddy, K. P. R. "Oxygen diffusion in close packed oxides." Ph.D. Dissertation, Case Western Reserve University, 1979.

31. Rovner, L. H. "Diffusion of oxygen in magnesium oxide." Ph.D. Thesis, Cornell University, 1966.

32. Hashimoto, H., and Hama, M. "Preferential diffusion of oxygen along grain boundaries in polycrystalline MgO." J. Appl. Phys. 43 (11), 4828 (1972).

33. Shirasaki, S., and Hama, M. "Oxygen diffusion characteristics of loosely sintered polycrystalline MgO." Chem. Phys. Letters 20, 361 (1973).

34. Shirasaki, S., Yamamura, H., Hama, M., and Hashimoto, H. "Oxygen diffusion in Li-doped polycrystalline MgO." Jap. J. Appl. Phys. 12, 1654-5 (1973).

35. Narayan, J., and Washburn, J. "Self-diffusion in Magnesium Oxide." Acta Met. 21, 533 (1973).

36. Oishi, Y., Ando, K., Kurokawa, H., and Hiro, Y. "Oxygen self-diffusion in MgO single crystals." J. Am. Ceram. Soc. 66 (4), C60-2 (1983).

37. Linder, R., and Parfitt, G. D. "Diffusion of radioactive magnesium in magnesium oxide crystals." J. Chem. Phys. 26 (1), 182-5 (1957).

38. Sempolinski, D. R., and Kingery, W. D. "Ionic conductivity and Mg vacancy mobility in MgO." J. Am. Ceram. Soc. 63 (11-12), 664-9 (1980).

39. Wuensch, B. J., Steele, W. C., and Vasilos, T. "Cation self-diffusion in single-crystal MgO." J. Chem. Phys. 58 (12), 5258-66 (1973).

40. Harding, B. C., and Price, D. M. "Cation self-diffusion in MgO up to 2350°C." Phil. Mag. 26 (1), 253-60 (1972).

41. Harding, B. C., Price, D. M., and Mortlock, A. J. "Cation self-diffusion in single crystal MgO." Phil. Mag. 23, (182), 399-408 (1971).

42. Wuensch, B. J. "On the interpretation of lattice diffusion in magnesium oxide." Mater. Sci. Res. 9, 211-31 (1975).

43. Gauthier, M., Fabry, P., and Deportes, C. "Transport cationique dans l'oxyde de magnesium monocristallin." Electrochem. Acta 19, 103-9 (1974).

44. Kittel, C. Introduction to Solid State Physics. 4th ed. New York: John Wiley & Sons, 1971.

45. Crank, J. The Mathematics of Diffusion. 2nd ed. Oxford: Oxford University Press, 1975; Clarendon Press, 1979.

46. Kofstad, P. Nonstoichiometry, Diffusion, and Electrical Conductivity of Binary Metal Oxides. New York: Wiley-Interscience, 1972.

47. Boltaks, B. I. Diffusion in Semiconductors. New York: Academic Press, 1963.

48. Krefft, G. B. "Radiation annealing studies in ion bonbarded MgO." Rad. Eff. 49, 127-32 (1980).

49. Amsel, G., Béranger, G., De Gélas, B., and Lacombe, P. "Use of nuclear reaction $^{16}O(d,p)^{17}O$ to study oxygen diffusion in solids and its application to zirconium." J. Appl. Phys. 39 (5), 2246 (1968).

50. Spadaro, J. V. "Penetration depth of dislocations formed during cold-work on the (100) surface of nominally pure MgO single crystals." Oak Ridge: ORNL, unpublished (1980).

51. Mayer, J. W., and Rimini, E. eds. Ion Beam Handbook for Materials Analysis. New York: Academic Press, 1977.

52. L'Hoir, A., Schmaus, D., Cawley, J., and Jaoul, O. "Depth profiling light nuclei in single crystals: a combined nuclear reaction and RBS technique to minimize unwanted channeling effects." Nucl. Instrum. Meth. 191, 357-66 (1981).

53. Fritsch, L., Marest, G., and Perez, A. "Defects created by indium implantation in magnesium oxyde crystals." In Nuclear Physics Methods in Materials Research - Proceedings of the 7th Divisional Conference, Darmstadt, September 23-26, 1980, pp. 411-414, ed. by. K. Bethge, H. Baumann, H. Jex, and F. Rauch.

54. Farlow, G. C., White, C. W., Appleton, B. R., Angelini, M. P., and McHargue, C. J. "Temperature effects on ion-induced damage in Al_2O_3." Paper presented at the 86th Annual Meeting of the American Ceramic Society, Pittsburgh, PA, 30 April 1984.

55. Meyer, M., Barbezat, S., Houch, C. E., and Talon, R. "Diffusion study of oxygen implanted in nickel oxide." J. Phys. Colloq. C6, 327-30 (1980).

56. Perez, A., Treilleux, M., Thevenard, P., Abouchacra, G., Marest, G., Fritsch, L., and Seruguetti, J. "Precipitation phenomena in implanted ionic oxide MgO." In Metastable Materials Formation by Ion Implantation, pp. 159-166. Ed. by S. T. Picraux, and W. J. Choyke. New York: Elsevier Science, 1982.

57. Weeks, R. A., Sonder, E., Pigy, J. C., and Kelton, K. F. "Reduction of impurity ions in MgO by current flow at high temperature." J. Phys. Suppl. 37, 411-14 (1976).

58. Berthelet, C., Kingery, W. D., and Vandersande, J. B. "Magnesium aluminate spinel precipitation in MgO." Ceramurgia International 2 (2), 62-6 (1976).

59. Kingery, W. D., Robbins, W. L., Henriksen, A. F., and Johnson, C. E. "Surface segregation of aluminum (spinel precipitation) in MgO crystals." J. Am. Ceram. Soc. 58 (5-6), 239-41 (1976).

60. Weeks, R. A., and Sonder, E. "Electrical conductivities at elevated temperatures of MgO single crystals doped with Fe, Cr, Ni, and Li." Rev. Int. Hautes Tempér. Réfract. 17, 154-64 (1980).

61. Kubaschewski, O., and Alcock, C. B. Metallurgical Thermochemistry, 5th ed. New York: Pergamon Press, 1979.

62. Tsang, K. L. "A new model for the dielectric breakdown of MgO crystals at high temperatures." Ph.D dissertation, University of Alabama, 1983.